CHALMERS
UNIVERSITY OF TECHNOLOGY

Thermal modeling and drivetrain-loss study for thermal management of electric machines

Utilizing powertrain heat for better performance in cold conditions

Master's thesis in Mobility Engineering

Filip Rosén
Maja Tyrbo

DEPARTMENT OF MECHANICS AND MARITIME SCIENCES
CHALMERS UNIVERSITY OF TECHNOLOGY
Gothenburg, Sweden 2023
www.chalmers.se

Master's thesis 2023

Thermal modeling and drivetrain-loss study for thermal management of electric machines

Utilizing powertrain heat for better performance in cold conditions

Filip Rosén
Maja Tyrbo

CHALMERS
UNIVERSITY OF TECHNOLOGY

Department of Mechanics and Maritime Sciences
Division of Energy Conversion and Propulsion Systems
Chalmers University of Technology
Gothenburg, Sweden 2023

Thermal modeling and drivetrain-loss study for thermal management of electric machines
Utilizing powertrain heat for better performance in cold conditions
Filip Rosén
Maja Tyrbo

Supervisors: Johan Larsson, Manjunath Nagappa, Polestar
Examiner: Dr. David Sedarsky, Division of Energy Conversion and Propulsion Systems

Master's Thesis 2023
Department of Mechanics and Maritime Sciences
Division of Energy Conversion and Propulsion Systems
Chalmers University of Technology
SE-412 96 Gothenburg
Telephone +46 31 772 1000

Cover: Collage with three parts. The Polestar Precept concept to the left, from [1]. Bottom right shows the developed electric motor thermal model in Simulink. The figures in the top right corner shows the operating points and electric motor losses during the SC03 cycle.

Typeset in LaTeX
Printed by Chalmers Reproservice
Gothenburg, Sweden 2023

Thermal modeling and drivetrain-loss study for thermal management of electric machines
Utilizing powertrain heat for better performance in cold conditions
Filip Rosén
Maja Tyrbo
Department of Mechanics and Maritime Sciences
Chalmers University of Technology

Abstract

The number of battery electric vehicles, BEVs, are increasing as the transportation sector is moving towards a more sustainable future with zero emissions. An issue with BEVs compared to conventional vehicles is their shorter range. To achieve higher efficiency and thereby longer range, every system on the vehicle must be optimised. This thesis has considered the thermal management system, cabin heating in cold conditions, and the utilization of heat losses from the electric drive unit, EDU.

To understand the benefit of an EDU loss-mode, i.e. operating with higher losses than nominal to create more heat, a thermal model of the electric machine was built. The thermal model is a lumped-parameter model capable of predicting the temperature of critical components, which enables over-loading analysis to ensure that the thermal capability of the machine is not exceeded. The model is parameterized only by dimensions and material data, and can be easily customized to new motor types. Verification with steady-state and WLTC test data showed good trend correlation and within the expected accuracy of 30%.

A vehicle-level thermal management model was built to implement and utilize heat losses from the electric drive unit. Simulations with an ambient temperature of -10°C and heating the cabin to 20°C were performed with EDU heat losses. Simulations with motor preheating was also performed.

Reduction of energy consumption for cabin heating was found to be approximately 7% when utilizing drive unit heat losses. Motor preheating reduced cabin heating consumption further, but used more energy over-all and was not found efficient.

Keywords: thermal management, battery electric vehicle, lumped parameter thermal network, heat loss utilization, thermal simulation electric machines, electric machine thermal modeling.

Acknowledgements

We would like to express our gratitude to our supervisors at Polestar Johan Larsson and Manjunath Nagappa, who have supported us during the whole thesis. Through their feedback in all aspects of modeling, correlation and overall project direction, we have learnt a lot both academically and professionally. We would also like to thank the rest of the R&D propulsion department, that have supported us with information, encouragement and an inviting workplace. Finally we would like to thank associate professor David Sedarsky for examining the thesis.

Filip Rosén and Maja Tyrbo, Gothenburg, June 2023

List of Acronyms

AC	Alternating Current
BEV	Battery Electric Vehicle
CFD	Computational Fluid Dynamics
DC	Direct Current
DE	Drive-End
dq0	Direct-Quadrature-Zero
EDU	Electric Drive Unit
EESM	Electrically Excited Synchronous Machine
EM	Electric Motor
EPS	Electric Propulsion System
ERAD/EFAD	Electric Rear/Front Axle Drive
FEA	Finite Element Analysis
GHG	Green House Gas
HTC	Heat Transfer Coefficient
HVCH	High Voltage Coolant Heater
HVAC	Heating, Ventilation and Air Conditioning
HVAH	High-Voltage Air Heater
LCA	Life-Cycle Analysis
LP	Lumped Parameter
LPTN	Lumped Parameter Thermal Network
MTPA	Maximum Torque Per Ampere
MTPL	Maximum Torque Per Loss
NDE	Non Drive-End
NEDC	New European Driving Cycle
NVH	Noise, Vibration and Harshness
PM	Permanent Magnet

PMSM	Permanent Magnet Synchronous Machine
PTC	Positive Temperature Coefficient
REE	Rare Earth Element
WLTC	Worldwide harmonized Light-duty Test Cycle

List of Parameters

α	Temperature coefficient $[W/m^2K]$
δ	Air gap length $[m]$
λ	Thermal conductivity $[W/mK]$
A	Surface area $[m^2]$
D_h	Hydraulic diameter $[m]$
F_g	Factor for modifying Taylor number [-]
h	Heat transfer coefficient $[W/m^2K]$
L	Length $[m]$
R	Thermal resistance $[K/W]$
r	Radius $[m]$
Nu	Nusselt number [-]
Pr	Prandtl number [-]
Re	Reynold's number [-]
Ta	Taylor number [-]
Ta_m	Modified Taylor number [-]
u_r	Peripheral rotor speed $[m/s]$

Contents

List of Figures

List of Tables

1
Introduction

This chapter introduces the thesis work, consisting of a background to the topic, the aim of the work and its limitations. Lastly, societal, ethical and ecological aspects as discussed.

1.1 Background

With a big environmental focus for the transport and automotive sector, reducing green house emissions, such as CO_2, has become an important matter. Therefore, more and more conventional vehicles with internal combustion engines are replaced by battery electric vehicles, BEVs, due to the absence of tailpipe emissions [5].

By replacing internal combustion engine vehicles with BEVs, the driving range of the vehicle becomes a problem. Charging a BEV takes time, and drivers must plan their driving. All customers might not be willing to adapt, which gives BEVs a drawback compared to conventional combustion engine vehicles [6].

The driving range of a BEV is also greatly reduced in cold ambient conditions [7]. The reason for this is twofold; for one, recuperated energy from regenerative braking is limited in order to protect the battery cells from premature aging [8]. This is commonly countered by heating with resistive heaters (e.g. Positive Temperature Coefficient, PTC, heaters), which although efficient present yet another auxiliary power consumer. Secondly, energy to heat the cabin is supplied by the vehicle's traction battery rather than relying on waste heat from combustion like a conventional vehicle [9]. A common solution to heat the cabin is to employ PTC heaters, which consume significant power and thereby leaves less energy for traction. Several sources report range losses of up to 50% [10] [11]. Another solution, presented in [12], is to use a heat pump which can utilize ambient heat, and thereby reduce the required energy with up to two thirds compared to PTC heaters [8]. Unfortunately, heat pumps are less efficient with lower ambient temperature, and are also at risk of freezing - therefore PTC heaters are commonly included anyway, to support in cold conditions.

Counteracting these attributes is currently a popular research topic, and many interesting architectures have been presented. Some examples are battery thermal management systems, BTMS, integrated with coolant loops [13], refrigerant cycles [11] and integration with Heat, Ventilation and Air Conditioning, HVAC [9].

Other are systems diverting recuperated energy for heating when charging is limited [8], holistic energy management optimization [14] and thermal storage using heat from powertrain components [10].

Recent investigations suggest that heat losses from the powertrain can assist heat pumps instead of PTC heaters [15]. A further step to this approach is to intentionally generate additional losses in the powertrain components to produce more heat than they would under normal operation, and in that way support the heat pump. This could be an interesting possibility in certain scenarios, and will henceforth be referred to as a "loss mode".

This thesis was carried out with the "System Design" team at Polestar, utilizing and building upon a simulation tool based on Matlab, Simulink & Simscape. The simulation environment is used for efficiency and performance investigation for the complete vehicle.

1.2 Aim

This thesis aims to expand the capabilities of an in-house developed simulation tool to enable simulation and analysis of heat generation in the electric drive unit, EDU. This includes, but is not limited to, the principle of an EDU "loss-mode".

Loss-mode refers to operation with losses higher than required, in order to utilize existing EDU components for heat generation. To enable the simulation of this, a thermal model of the electric machine is built. The thermal model can evaluate the heat generated in the individual parts as well as heat carried by the coolant. This makes it possible to evaluate both how much heat can be extracted utilizing a loss-mode, as well as monitoring that the electric machine does not overheat.

A further aim of the thesis is to evaluate if powertrain losses can be utilized to reduce energy consumption from cabin heating in cold climate, as has been discussed in section 1.1 above. This particular application was chosen among other possible aspects where an EDU loss-mode can be of interest.

1.3 Limitations

The vehicle model is intended to be lightweight and be able to run simulations fast with sufficient accuracy for vehicle-level simulations. Therefore all developed models must adhere to this concept, which means numerical analysis such as finite element, FE, and computational fluid dynamics, CFD, cannot be used.

1.4 Societal, ethical and ecological aspects

In commitment to reduce greenhouse gases, GHG, from the transportation sector, car manufacturers such as Polestar [16] are building electric cars for sustainable mobility. While electric vehicles emit more in the production phase, life-cycle analysis, LCA, show that the utilization phase is the dominant factor for vehicles and since EVs have zero tailpipe emissions, they emit significantly less over their complete life-cycle [17]. Still, LCA results varies locally depending on the primary energy sources used to produce the electricity. It is therefore important for EVs to be as energy efficient as possible. Since the thesis aimed to investigate further reduction in energy consumption, the thesis is considered to be favourable to society and ethical. These aspects were therefore not taken into further consideration.

Ecological aspects was taken into account during the thesis. For example, reflecting on the aspects of added components and materials in the proposed concepts. A complete LCA analysis was however beyond the scope of the thesis and was not performed.

2
Theory

This chapter describes the theoretical background of electric machines and thermal management of electrical vehicles that is used throughout the thesis. First of, section 2.1 presents common electric machine topologies and sustainability considerations. The different internal losses are described, along with a discussion on how a loss-mode strategy can be implemented and some potential issues. Finally, methods for thermal analysis of electric machines is reviewed. In section 2.2, the methodology of modeling the electric machine as a lumped-parameter thermal network, LPTN, is described. Furthermore, the heat transfer paths through the electric machine is discussed along with a review of the different heat transfer modes of conduction, convection and radiation. Section 2.3 describes how the thermal management works in a BEV, including the refrigeration cycle and what a PTC heater is. Section 2.4 describes why driving cycles are used and the ones that have been used in this thesis work.

2.1 Electric machines

With the increasing use of electric machines for traction in vehicles, comes a demand for machines with higher power density and efficiency as well as reduced in size and weight. A good thermal design is crucial to ensure that the desired performance and reliability is achieved. In particular, some components where hot-spots typically develop are critical to keep within safe limits, namely the windings and the permanent magnets. The lifetime is approximately reduced by half for every 10°C increase above the thermal class of the winding insulation, and the permanent magnets are at risk of demagnetization and even developing cracks [18].

A review of the motor topologies considered in the thesis is described in section 2.1.1, followed by a discussion on electric machine losses in section 2.1.2. Loss-mode strategy as a component of thermal management is covered in in section 2.1.3, and lastly some common methods for thermal analysis is reviewed in section 2.1.4.

2.1.1 Topologies

While there are numerous different types of electric motors, they share similar components. However, this study considered two topologies in particular during development, the permanent magnet synchronous machine, PMSM, and the electrically

excited synchronous machine, EESM. Synchronous motors are common in electric vehicles due to some notable features like high efficiency, high power density and high speed capabilities [19] [20].

The two considered topologies feature similar stator assemblies, consisting of a wound stator core that is energized by alternating current, AC. The core, made from laminated steel sheets, facilitate conduction of the magnetic flux when energized. The windings are copper conductors wound together and insulated by a coat of impregnation varnish. The coated winding is also insulated from contact with the stator core using a thin composite material known as slot liner. Figure 2.1 below shows a generic example stator, with the laminated core, insulated copper conductors wound around the stator teeth and with slot liner in between.

Figure 2.1: Example of a stator assembly showing the laminated core, windings and insulation. From [2].

The main difference between the two topologies is the rotor assembly. By definition, a synchronous machine rotates with the same speed as the magnetic field produced by the stator excitation. As opposed to an induction machine, where the rotor is excited by induction, the synchronous machine's rotor produces a magnetic field that synchronizes with the magnetic field from the stator. In a PMSM, permanent magnets are attached to the rotor, while the EESM has a wound rotor similar to the stator assembly. The wound rotor must therefore be supplied with a separate excitation current, which increases complexity but also allows for continuous power factor control and increased efficiency [20]. Figure 2.2 below illustrates the difference between the rotors in a PMSM and an EESM.

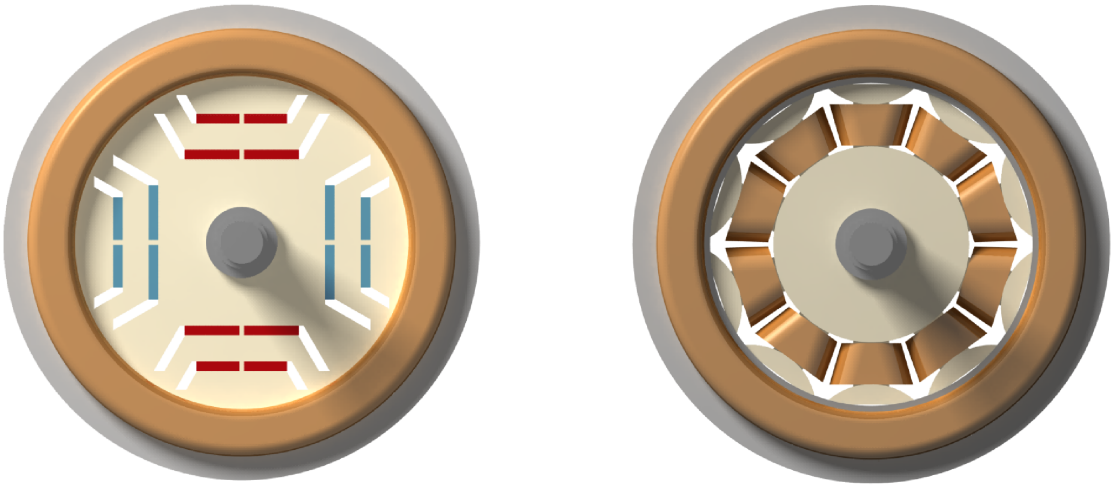

(a) PMSM. **(b)** EESM.

Figure 2.2: Illustration of PMSM and EESM rotors.

Figure 2.2a shows a PMSM, where the outer grey part is the stator. Moving radially into the middle of the motor, are the stator windings in reddish brown followed by the core of the rotor in beige. The magnets are red and blue and in the middle of the motor is the shaft in grey.

An EESM is shown in figure 2.2b, where the stator is the same as for the PMSM. Inside the stator windings are the rotor shoes in beige that the rotor windings in reddish brown are wound around. After is the rotor core in beige and finally the shaft in grey, in the middle.

2.1.1.1 Sustainability

While the total life-cycle emissions of battery electric vehicles are generally lower than for vehicles with combustion engines, the production phase typically emits more green house gas, GHG, emissions [17]. This is usually attributed to the battery production, but never the less, solutions to lower the environmental load posed by the electric machine is a popular research topic. One aspect is the use of rare earth element, REE, magnets, such as the commonly used neodymium-iron-boron, NdFeB, in PM machines. A review of machine topologies with reduced amounts or no magnets at all, that can produce similar characteristics as a PM machine, is presented in [21]. A design study of a machine with reduced magnet content together with a discussion on the environmental load of common EM materials is found in [22]. Furthermore, the environmental load of aluminium is a lot lower than copper, and it has been shown that an aluminium hairpin design can be considered an alternative to the common copper hairpin or copper-strand windings [23] [24]. Hairpin windings, as opposed to conventional wound strands, are solid bars bent in a shape similar to that of a hairpin.

2.1.2 Losses

Power losses in the electric machine occur due to irreversible energy conversion processes in the materials, and ultimately turns into heat. These processes are typically categorized as copper losses, iron losses and mechanical losses. Additionally, there are losses from the magnets in the case of a permanent magnet assisted topology [18] [25].

2.1.2.1 Copper losses

Losses in the copper windings can be divided into two components, namely direct current, DC, and alternating current, AC, losses. The DC losses are proportional to the winding resistivity and to the square of the current, as shown by equation (2.1). The resistivity, and therefore also the copper losses, are temperature dependent, which is typically accounted for by calculating the conductor resistivity using the temperature coefficient α of the material, as per equation (2.2) [26]. Here, T_{ref} and R_{ref} is the temperature and resistance at some known temperature.

$$P_{Cu} = R \times I^2 \tag{2.1}$$

$$R = R_{ref}\Big(1 + \alpha(T - T_{ref})\Big) \tag{2.2}$$

The AC loss component comes from the redistribution of current density in the conductor due to the induced magnetic field, and is further divided into the skin effect and the proximity effect. These effects are rather small in comparison to the DC component [27]. From the proportionality to resistivity and current, copper losses can be summarized as dependent on temperature and motor torque, which typically requires higher current.

2.1.2.2 Iron losses

Iron losses refer to the losses in both stator and rotor core, which are made from a laminated steel material. These are divided into hysteresis and eddy current loss. Magnetic hysteresis can be compared to friction when the magnetic flux density lags the change in magnetic field. Eddy currents are induced in the material due to changes in the magnetic field. These components are both frequency dependent, and therefore iron losses typically increase with motor speed [25].

2.1.2.3 Mechanical losses

Losses occurring due to the mechanical rotation of the rotor can be divided into friction losses and windage losses. Friction loss is associated with the shaft bearings and windage is due to the drag caused by air friction. These are both mainly dependent on the motor speed.

2.1.2.4 Magnet losses

In permanent magnet assisted machines, magnet losses occur from similar mechanisms as iron losses. Even though magnet losses are one of the smaller losses, they

are important to consider. This is because the magnet material has comparatively low thermal conductivity, and hence cools down slowly.

2.1.3 Loss-mode strategy

Electric machine analysis is commonly simplified by transforming the three-phase reference frame into the direct-quadrature-zero, *dq0*, reference frame. By studying the torque equation of an electric machine in the *dq0* reference frame, eq. (2.3) [27], it is evident that different values of direct and quadrature current (i_d & i_q) can create the same torque. Different combinations will however create different amounts of losses, and normally a strategy such as MTPA, maximum-torque-per-ampere, would be employed to minimize losses. MTPL, maximum-torque-per-loss, is another common loss minimization strategy.

$$T_e = \frac{3}{2} n_p \Big(\Psi_m i_q + (L_d - L_q) i_d i_q \Big) \tag{2.3}$$

A loss-mode feature attempts to do the opposite, operating the motor at a "worse-than-optimal" operating point and hence create more heat.

2.1.3.1 Potential use cases

This added heat can potentially be of benefit to other parts of the vehicle. One such case could be to heat up the cabin or the battery by heat pump operation. Another potentially interesting case is to heat up the transmission to lower its losses.

Maximum heat generation for an EDU in the Volkswagen ID.3 has been quantified in [15], considering a loss-mode in the electric machine and inverter. Combined losses ranging between 5.8 to 7.9 kW at low speed operation and between 4.5 to 5.4 kW at standstill is reported. Further, heat generation up to 6.5 kW is found possible at standstill if a disconnect/clutch is utilized.

2.1.3.2 Potential issues

Some potential issues can be identified with this strategy. First and foremost, the available operating region is limited by the thermal capacity of the EDU components and must be carefully monitored. As previously discussed, excessive temperatures can have serious implications on both lifetime and performance, and so it is imperative that hot spots within the motor is kept within safe limits.

An increase in torque ripple is observed in [15] when deviating from the common MTPA strategy. This has a negative effect on the passenger comfort in terms of noise-vibration-harshness, NVH, and would have to be further studied before implementation.

2.1.4 Thermal analysis

Predicting the thermal behavior of an electric machine is of great interest to ensure the performance and lifetime meet expectations, but has traditionally been of sec-

ond interest. When used as a traction motor for electric vehicles however, thermal analysis is necessary to verify performance during the highly varying load that is typical of an automotive application.

Thermal analysis can be performed using analytical or numerical methods. Analytical methods typically compute very fast, but requires some effort and experience to construct a network of reasonable accuracy. A common analytical technique is the lumped-parameter thermal network, LPTN, which will be described further in section 2.2 below. Numerical methods can be divided in two types, finite-element analysis, FEA, and computational fluid dynamics, CFD. These are very useful due to their high accuracy and diverse range of application, being able to model any geometry. They are however very time demanding both in setup and computational time [28].

In FE analysis, the components are divided into a coherent mesh of very small nodes, and the analysis takes place with respect to the change over these small volumes. Because of this computer-aided meshing, FEA can better analyze complex geometries that are difficult to capture with lumped-parameter models, and its accuracy is directly influenced by the level of detail in the mesh. CFD analysis is commonly used to simulate performance with respect to cooling and fluid flows, such as velocity, heat transfer coefficients and pressure. Typically CFD analysis only solves fluid characteristics, but can be extended to cover the solid domain using the conjugate heat transfer method [18] [29].

The presented methods of thermal analysis can favourably be used in conjunction. For a motor with an intricate cooling system, the accurate but time consuming CFD analysis can provide heat transfer boundary conditions as input to the lumped-parameter model. Furthermore, finite-element analysis can be used to find an accurate thermal resistance for parts of complex geometry. The analytical model can then used to study thermal behaviour in different load conditions. Such a methodology is presented in [30] and [31].

2.2 Lumped-parameter thermal network

An electric machine is a complex system with a number of different components, some of which with rather complicated geometries. A lumped-parameter, LP, model simplifies the machine to a number of nodes, by representing the components as a lumped mass with equal or similar thermal behaviour. The nodes contain a thermal mass representative of the component, and heat transfer between nodes are represented by thermal resistances connecting each component. There are many ways of constructing a LP model, such as choosing spatial heat transfer domain (2D/3D) and the level of discretization, and it is up to the designer of the system to chose according to the requirements of the system in question [32].

A lumped-parameter thermal network is analogous to an electrical circuit network, where voltage corresponds to temperature, current to power, and electrical resistance to thermal resistance. The thermal resistances can be calculated from component geometry and material properties, and empirical formulas for heat transfer coefficients in the case of convection [28]. This calculation is accounted for in section 3.2.

The lumped-parameter methodology has been subject to many publications for different machine sizes and topologies, reporting temperature predictions with an accuracy of ± 5-20%, which is what can be expected [30]. Figure 2.3 illustrates the individual components that are considered a specific node. The view is symmetric around the shaft, and the subscripts "DE" and "NDE" represent the motor drive-end and non drive-end respectively. This naming convention will be used throughout the thesis.

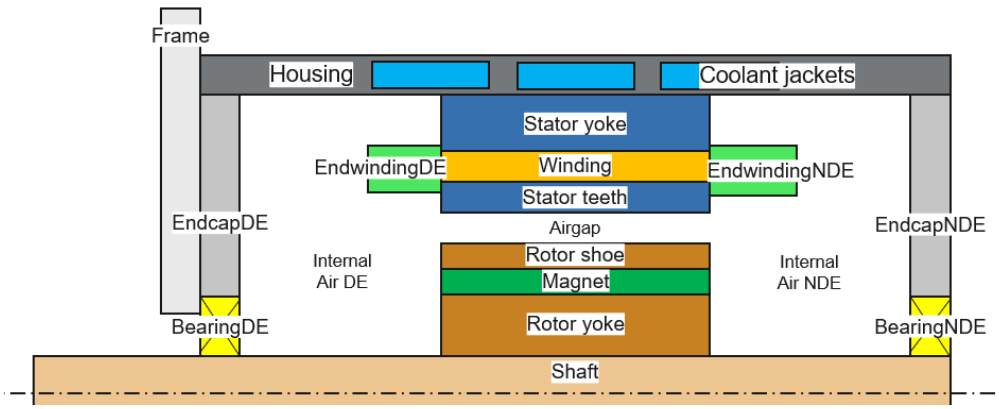

Figure 2.3: Simplified illustration of an electric motor in axial cross-section, with the component naming convention used throughout the thesis. The view is symmetric around the shaft.

2.2.1 Heat transfer

The temperature gradients in an electric motor arise from the internal losses described in section 2.1.2. These gradients in turn lead to heat transfer between components, in the natural attempt to reach a thermal equilibrium. Heat transfer

takes place through three modes; conduction, convection and radiation. The heat paths in an electric motor is illustrated in figure 2.4 below, for conductive and convective heat transfer. Note that the direction of heat transfer as indicated by figure 2.4 is not always true, it is instead decided at any given moment by the temperature gradient between the parts. The figure should instead be treated as a reference as to what modes of heat transfer is considered in the different components.

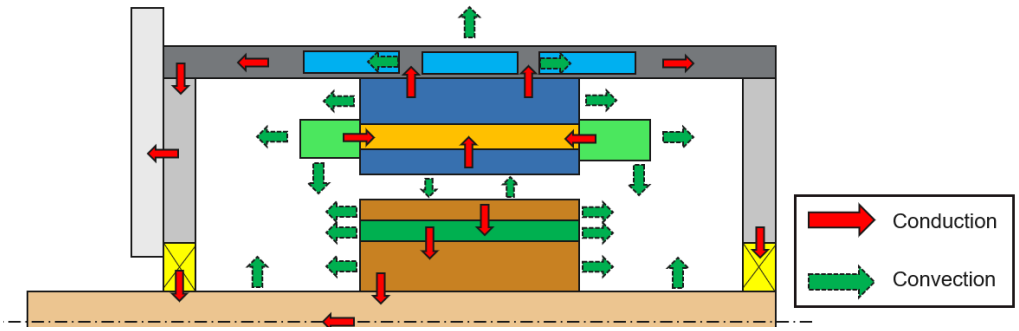

Figure 2.4: Illustration of heat paths in an electric motor, by conduction and convection. See figure 2.3 for component reference.

2.2.1.1 Conduction

Heat transfer by conduction occurs due to thermal diffusion and molecular interaction, and applies to solids and stationary fluids and gases. In an electric machine, conduction is thus considered between all solids. The rate of heat conduction through the material is a function of component area, length, thermal conductivity and temperature difference between the two components in contact [33] [27]. This relationship is stated in eq. (2.4) below. The thermal conductivity of a material is a measure of its ability to conduct heat, which in some cases differ depending on direction. This is called thermal anisotropy, and commonly applies to components that have been laminated or cold-pressed, such as the stator iron and copper windings respectively [34].

$$\dot{Q}_{\text{cond}} = -\lambda A \frac{\Delta T}{L} = f\Big(\text{geometry}, \Delta T, \lambda\Big) \tag{2.4}$$

Where $\dot{Q}_{\text{cond}}$ is the heat transfer rate $[W]$, λ is the thermal conductivity of the material $[W/mK]$, A is the contact area $[m^2]$, L is the contact length $[m]$ and ΔT is the temperature gradient between the components $[K]$.

2.2.1.2 Convection

Heat transfer by convection occurs between a solid and a contiguous fluid or gas in motion, and is a combined effect of conduction and the fluid motion. Heat is transferred by conduction to the adjacent layer of liquid, where the velocity approaches standstill. This liquid is then transferred away by the fluid motion and replaced by colder liquid. In the case of no fluid motion the heat transfer is purely by conduction, a relationship which the dimensionless "Nusselt number" describes (eq. (2.6) below). Convection can be described as *forced* if the fluid motion is forced

by any external means, like a fan or pump. On the contrary, if no such forced flow is exerted, the convection is described as *natural* [33] [35]. The rate of heat transfer by convection is described by the expression in eq. (2.5) below.

$$\dot{Q}_{conv} = h_C A(T_{\text{surf}} - T_{\text{liquid}}) = f\Big(\text{geometry}, h_C, \Delta T, \Big) \tag{2.5}$$

Where $\dot{Q}_{conv}$ is the heat transfer rate $[W]$, h_C is the heat transfer coefficient $[W/m^2K]$, A is the surface area $[m^2]$, T_{surf} is the surface temperature $[K]$, and T_{liquid} is the liquid temperature $[K]$.

2.2.1.2.1 Nusselt number For calculations of heat transfers that are a combination of conductive and convective, the Nusselt number can be used. It represents the ratio between these two heat transfers at the fluid's boundary. In general, the higher the Nusselt number is, the more turbulent the flow is and if the Nusselt number is equal to 0, the heat transfer is purely conductive [36].

There are a few different ways to model heat transfer with the Nusselt number, one of them is the Gnielinski correlation. It is a simplification of heat transfer through the walls of tubes, using just the hydraulic diameter and friction factor [37]. The hydraulic diameter is defined as the ratio between the wetted area and the wetted perimeter of the body. When the flow is laminar, the Nusselt number is important for determining this heat transfer, but for turbulent flows, the hydraulic diameter and friction factor are enough.

$$\text{Nu} = \frac{Q_{\text{conv}}}{Q_{\text{cond}}} = \frac{hL}{\lambda} = f\Big(\text{geometry}, \text{Re}, \text{Pr}\Big) \tag{2.6}$$

Where h is the heat transfer coefficient $[W/m^2K]$, L the contact length $[m]$, and λ the thermal conductivity of the material $[W/mK]$ [27].

2.2.1.3 Radiation

Heat transfer by radiation occurs due to photon emittance from a surface to other surfaces or the surroundings. A *black body* has an emissivity (ε) of 1, and other surfaces relates to this as a value ranging between 0-1. The rate of heat transfer by radiation is described be eq. (2.7) below.

$$\dot{Q}_{rad} = \varepsilon\sigma A(T_{\text{surf}}^4 - T_{\text{amb}}^4) = f\Big(\text{geometry}, h_C, \Delta T, \Big) \tag{2.7}$$

Where $\dot{Q}_{rad}$ is the heat transfer rate $[W]$, ε is the surface emissivity $[-]$, σ is Stefan-Boltzmann's constant $[W/m^2K^4]$, A is the surface area $[m^2]$, T_{surf} is the surface temperature $[K]$, and T_{amb} is the surrounding temperature $[K]$.

2.3 Vehicle thermal management

The range of a BEV is the distance possible to travel without the need to recharge the battery. The range is dependent on multiple different parameters, one of the most significant is the Heat, Ventilation and Air Conditioning, HVAC, system as it can drastically decrease the range of the vehicle [38]. As electric motors generate much less heat losses than combustion engines, the vehicle thermal management in EVs cannot rely on conventional powertrain heat, especially during cold climate conditions. Heating up the cabin uses more energy as an external heater needs to be used when the heat losses in the motor are not enough. Another aspect is that the battery temperature must be kept within its specified operating range to work properly, which includes both heating and cooling [39].

2.3.1 Refrigeration cycle

Most vehicles today are equipped with an HVAC for the comfort of the passengers. For enabling provision of cold or warm air from the HVAC, a refrigeration system is used. A typical refrigeration system consists of a compressor, condenser, expansion valve and evaporator. In a BEV, when a battery has to be cooled in the same process, a chiller can also be included in the refrigerant cycle. Refrigerant is flowing through these components and its temperature changes in the cycle between them [40].

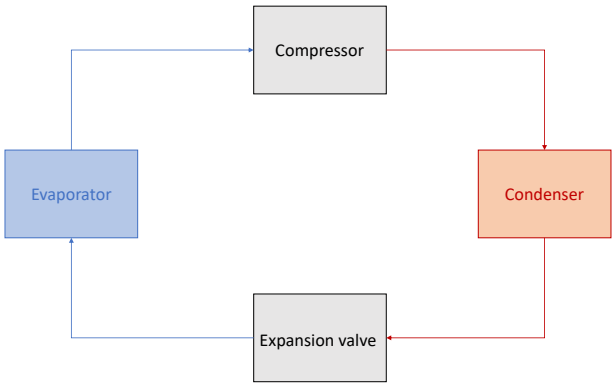

Figure 2.5: Schematic illustration of a conventional refrigeration cycle

2.3.1.1 Compressor

The compressor is used to compress the refrigerant to increase both its pressure and temperature. The warm and pressurized refrigerant then moves along to the condenser.

2.3.1.2 Condenser

A condenser is a heat exchanger between the refrigerant in the system and another fluid or air surrounding it. This means that warm refrigerant gets cooled down

by the condenser and the heat is transferred to the surrounding fluid or air. The temperature changes due to condensation of the warm refrigerant that enters the condenser in vapor state. The vapor is condensed and changes its phase to liquid, thus releasing heat and decreasing its temperature [41].

2.3.1.3 Evaporator

The evaporator is placed after the condenser, with an expansion valve in between that expands the refrigerant to create a pressure drop, causing some of it to boil. The low temperature refrigerant enters the evaporator that further cools it down by exchanging heat with fluid or air in its surrounding, like the condenser [40].

2.3.1.4 Chiller

A chiller is used for cooling systems like the battery or electric propulsion system, EPS. This is done by using the chiller as a heat exchanger between the refrigerant in the refrigeration circuit and the cooling fluid from the battery and/or EPS. The cold refrigerant comes out of the condenser and cools the warm coolant fluid when exchanging heat with it in the chiller. The cooling fluid, that is now cooled down, goes through the systems it is connected to and cools them down. In conventional refrigerant cycles, the chiller is placed in parallel with the evaporator [42].

2.3.2 PTC heater

A positive temperature coefficient heater, PTC heater, is a component that uses electrical resistance to heat up mediums and materials, like in the case of this thesis, air. It can also be called a high voltage coolant heater, HVCH when used for heating up coolant. These heaters have been used in the automotive industry for heating components in combustion engines for efficiency reasons, but are now the main component for heating in electrical vehicles [43]. The main property of a PTC heater that makes it a good choice for heating up a cabin is that it is self-regulating and able to reduce condensation on the vehicle's windows. Self-regulation means that regardless of the heat or voltage applied, it is able to keep a constant temperature by changing the resistance. This is thanks to the heater having a large positive resistance coefficient that increases with the temperature, which means that the temperature coefficient is above 0 [44].

2.3.3 Electric motor preheating

Preheating an electric motor before starting it is a method of optimizing the performance of it as well as decreasing its power consumption and wear. As different motor temperatures make the motor behave in different ways, the right temperature of the motor for a certain scenario could increase the performance [45]. In cold ambient temperatures, the motor will be cold during the start. This means that the materials in the motor components are cold and stiff, which increases the wear when the motor is started.

2.4 Driving cycles

A driving cycle is a cycle made for simulating different driving scenarios while testing vehicles. It consists of a sequence of data that represents the vehicle speed over time, which allows for consistent testing of vehicle performance such as energy consumption, or the propulsion system performance. To do so accurately, it is important to use real-world driving cycles that consider the vehicle performance properly [46].

2.4.1 NEDC

One widely used driving cycle is the New European Driving Cycle, NEDC. It includes four urban driving cycles and ends with an extra-urban driving cycle to capture different conditions in one cycle. The NEDC has high accelerations and decelerations and reaches a maximum speed of 120 km/h, while maintaining an average speed of 32 km/h [47]. The velocity curve can be seen in figure 2.6.

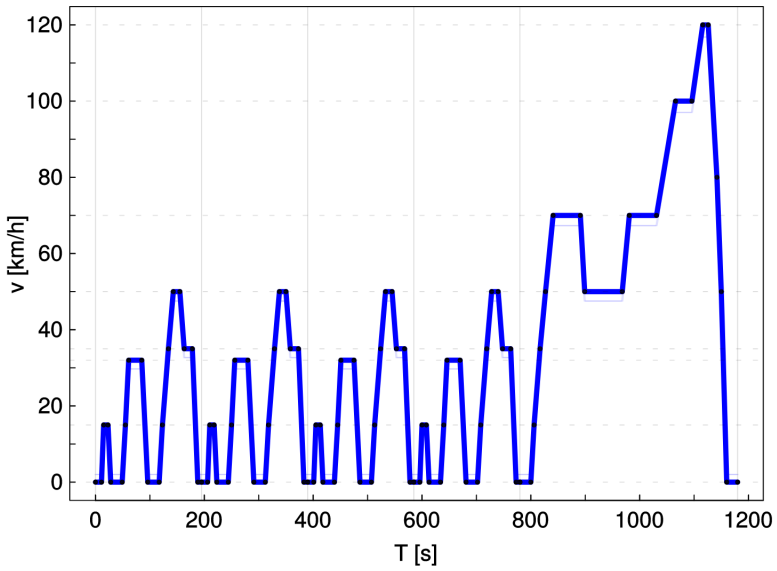

Figure 2.6: NEDC diagram [3].

2.4.2 WLTC

The successor to the NEDC is the slightly longer and more dynamic Worldwide harmonized Light-duty Test Cycle, WLTC. For this thesis, the WLTC class 3b was used. It starts with a low speed section up to 60 km/h, followed by a medium speed section where the maximum velocity almost reaches 80 km/h. After is a high-speed section and an extra high-speed section with maximum velocities of almost 100 km/h and 140 km/h respectively [48]. The velocity curve is shown in figure 2.7.

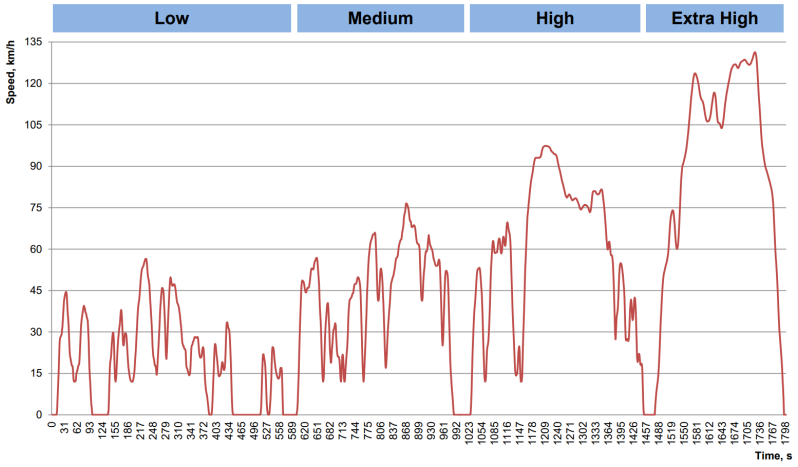

Figure 2.7: WLTC class 3b diagram [4].

3
Methods

This chapter describes the methodology used to build the lumped-parameter model of the electric machine, as well as the vehicle thermal management model. The overall methodology of this thesis was to first build a model of an electric machine and all its physical aspects, like heat transfer and heat losses. A verification was then done on the model by comparing simulation results to test data. When the model was verified, a thermal model on vehicle level was made where the losses from the EM model were implemented. With these models it was then investigated if the heat losses could aid the heating of the cabin and therefore reduce the power consumption of the PTC heater that is heating up the cabin. The focus in this thesis was therefore to utilize the losses for heating up the cabin, and not other aspects that have been mentioned. The work has been described in detail in the sections of this chapter where, first of, a review of the simulation tool is given in section 3.1. Then, details on building the lumped-parameter model is presented in section 3.2, including parameterization and a review of empirical equations to support the model. Further, the layout and parameters of the vehicle thermal management model is described in 3.3, and finally the implementation to study drivetrain loss utilization is discussed in section 3.4.

3.1 Tools and software

This thesis was performed using MATLAB, Simulink and Simscape. MATLAB is a computing platform suitable for building models, running simulations and subsequently analyzing the output data. Simulink adds capability to MATLAB in the form of a block diagram environment that enables model-based design and interfacing between different physical domains [49] [50].

3.1.1 Simscape modeling

Simscape enables quick modeling of physical systems through a library of fundamental components for different physical domains, e.g. electrical, fluids, thermal. The blocks are assembled through physical connections in a schematic format to represent the system of study, and Simscape formulates the implicit equations for the complete physical system. Parameters and boundary conditions are parameterized with MATLAB [51].

The domains that have been used in this thesis are the moist air domain, thermal

domain, thermal liquid domain, two-phase fluid domain and mechanical rotational domain. The domains represent physical attributes and enables modeling with high fidelity and accurate results. This is because quantities like mass flow, power and temperature are preserved and that losses and efficiency can be taken into consideration [52]. The colors of the domains used in this thesis are shown in figure 3.1.

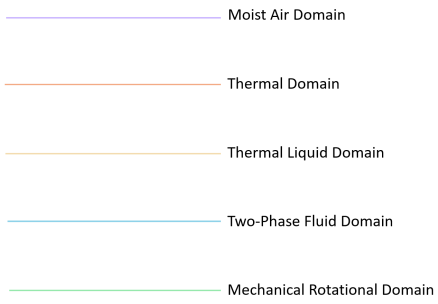

Figure 3.1: Color codes for the Simscape domains used in this thesis.

The moist air domain has a purple color of its connections and represents air in systems that can be dry, water vapor and also carbon dioxide. In this domain, the air can change its state when it is, for example, being heated up, so that a part of it is vapor, or cooled down, so that a part of it is water. The moist air has in this thesis mainly been used to represent the air inside of the cabin as well as the environmental air coming from the outside of the vehicle [53].

The most used Simscape domain in this thesis is the thermal domain, as it is more general than the other domains and defines quantities like thermal resistance, thermal mass, temperature and heat flow. It is therefore suitable for modeling a LPTN system, and it enables heat transfer to a liquid through the thermal liquid domain. The thermal domain has a red color [54].

The thermal liquid domain was used for modeling the coolant liquid that is cooling the motor. It has a yellow color and is easily integrated to transfer heat between other domains. The thermal liquid domain is suitable for modeling single-phase fluids which are expected to change significantly in temperature [55].

For representing refrigerant, the two-phase fluid domain is used. In the vehicle thermal management model, refrigerant is used in the HVAC system with heat exchanger interfaces to both the cabin and the battery coolant circuit. The two-phase fluid is considered part gas and part liquid, and changes its state depending on the temperature and pressure it is exposed to. The two-phase fluid has a blue color when modeled in Simscape [56].

The mechanical rotational domain has a green color in Simscape and has been used for modeling components like the compressor fan and motor pump. The domain uses quantities such as angular velocity and torque, and is used in cooperation with other domains [57].

3.2 EM thermal model

The EM thermal model aimed to predict the temperature in different components of the machine, with an approximate accuracy of 30%. This accuracy was specified based on what is commonly reported in literature for similar models. Further, the model was to be very general, easy to parameterize and computationally lightweight. As stated in section 2.1.1, electric machines of different topologies share a number of similar components. This is beneficial for the model developed in this thesis, since the model can cover a variety of different machines with minimal modification. Based on a literature review in thermal analysis of electric machines, the "T-equivalent" configuration was chosen, along with the simplification that all components were assumed cylindrical. Hence, the only parameters necessary are basic dimensions (length & diameter) and material data. A schematic of the T-equivalent circuit is shown in figure 3.2.

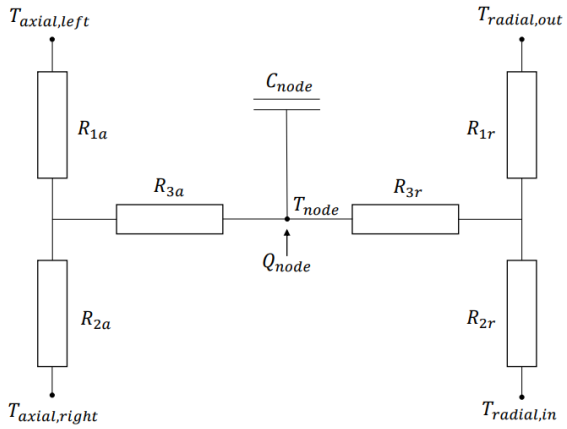

Figure 3.2: T-equivalent lumped-parameter model.

The T-equivalent circuit is used for each node in the network, where each node models a specific component of the machine. It includes heat transfer in axial and radial direction, and describes this by three resistances in an axial network (R_{1a},R_{2a},R_{3a}) and three resistances in a radial network (R_{1r},R_{2r},R_{3r}). The axial and radial networks are configured in a T, and their common connection point is considered the node. To this node, a thermal capacitance is connected to enable transient analysis, and the internal losses are applied. Determination of thermal resistance is described in section 3.2.1, thermal capacitance in section 3.2.2, and the applied losses in section 3.2.3.

3.2.1 Thermal resistance

When assuming a cylindrical geometry of the solid components, the conductive thermal resistances can be calculated as shown in table 3.1 [58]. The observant reader can notice that R_3 is negative. This is because R_1 and R_2 over predicts the node temperature, so R_3 compensates for this [59].

Table 3.1: Radial and axial resistances for conductive heat transfer

Resistance	Radial direction	Axial direction
R_1	$\frac{1}{4\pi\lambda L}\left(\frac{(1-2r_2^2 ln\left(\frac{r_1}{r_2}\right)}{r_1^2-r_2^2}\right)$	$\frac{L}{2\pi\lambda(r_1^2-r_2^2)}$
R_2	$\frac{1}{4\pi\lambda L}\left(\frac{(2r_1^2 ln\left(\frac{r_1}{r_2}\right)}{r_1^2-r_2^2}-1\right)$	$\frac{L}{2\pi\lambda(r_1^2-r_2^2)}$
R_3	$\frac{-r_1^2-r_2^2+\frac{4r_1^2r_2^2 ln\left(\frac{r_1}{r_2}\right)}{r_1^2-r_2^2}}{8\pi\lambda L(r_1^2-r_2^2}$	$\frac{-L}{6\pi\lambda(r_1^2-r_2^2)}$

Where λ is the thermal conductivity $[W/mK]$, L is the length of the component $[m]$, r_1 is the outer radius $[m]$ and r_2 is the inner radius $[m]$.

Conduction

Conductive heat transfer is considered in the interface between all solid parts of the machine, as previously shown in figure 2.4. This includes the housing, stator yoke, active winding, stator tooth, rotor shoe, rotor windings/permanent magnets, rotor yoke, shaft, bearings, and end caps. As the third resistance R_3 is negative, a custom-made Simscape block had to be created by modifying the original thermal resistance block. This is because Simscape by default does not accept a negative resistance. Figure 3.3 below shows a node implemented in the model.

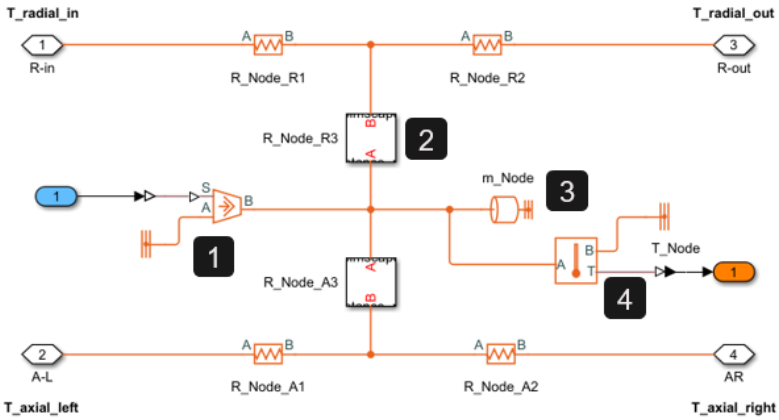

Figure 3.3: Example of a node in the model with an applied loss in (1). The custom thermal resistance block is indicated by (2), thermal capacitance in (3) and the temperature sensor in (4).

Laminated steel

Thermal conductivity of the lamination steel sheets may be given by the manufacturer, however this value is not accurate when considering the laminated product. The axial conductivity when the sheets are laminated depends on many factors such

as clamping pressure and insulation material between sheets [35] [60]. There is a gap in the literature on this topic, but there are known intervals of anisotropy ratios (radial-to-axial thermal conductivity). For this thesis, a ratio of (31/0.37) was used corresponding to values reported in [25]. This equates to 19.8 [W/mK] radially to 0.24 [W/mK] axially, as shown in table 3.4.

Windings

The copper windings constitute a major loss source, and in order to divert this heat from the machine to the coolant, it must typically pass through the stator core. However, it is not trivial to determine the thermal conductivity from the windings, since it is an assembly of many materials with largely varied physical properties. The part of the windings contained in the slots along the active length of the machine is considered one lumped node, and the end part of the windings on each side of the machine is considered one lumped node each. The active winding configuration assumed in this thesis consist of a number of copper conductors individually coated by an insulating varnish, jointly covered in an impregnation and with a thin slot liner at the boundary of the slot. This is illustrated in figure 3.4a below.

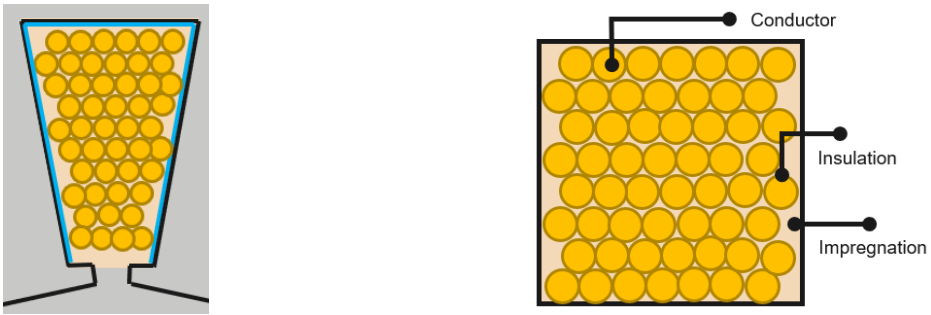

(a) Winding assembly in slot, liner shown in blue.

(b) Sample of winding assembly, with annotation.

Figure 3.4: Illustration of active windings with its composite parts.

To account for this composition of materials, an equivalent thermal conductivity is calculated to represent a fictive homogeneous material. A formulation for circular conductors derived in [61] is used. First, an equivalent thermal conductivity for the insulation and impregnation is calculated, followed by the equivalent thermal conductivity for the complete assembly. This is expressed in equations (3.1) to (3.2) below. Here, λ_{eqv} is the equivalent thermal conductivity for the complete assembly, and λ_i is the equivalent thermal conductivity for the insulation and impregnation. Further, λ_{imp} and λ_{ins} is the impregnation and insulation thermal conductivity, and λ_c is the conductor thermal conductivity. The volume factor v_c equals the slot fill factor, the areal ratio of conductors in the slot to the full slot area. Lastly, v_i and v_{ci} represent the impregnation and insulation areal ratio. End winding thermal conductivity is described by equation (3.3), where F_{ew} is the fill factor, λ_{ew}, λ_{Cu} and λ_{ins} is the equivalent, conductor and insulation thermal conductivity, respectively.

$$\lambda_{eqv} = \lambda_i \frac{(1+v_c)\lambda_c + (1-v_c)\lambda_i}{(1-v_c)\lambda_c + (1+v_c)\lambda_i} \tag{3.1}$$

$$\lambda_i = \lambda_{imp}\frac{v_i}{v_i+v_c} + \lambda_{ins}\frac{v_c}{v_i+v_c} \tag{3.2}$$

$$\lambda_{ew} = \lambda_{Cu}F_{ew} + \lambda_{ins}(1-F_{ew}) \tag{3.3}$$

Convection

Convective heat transfer is considered for all components connected to air. Either to ambient, through the air gap, or the trapped air in the end cap regions. The later is in this thesis referred to as "internal air". Thermal resistance due to convection is calculated from equation (3.4).

$$R_{\text{conv}} = \frac{1}{h_C A} \tag{3.4}$$

where A is the surface area of the interface between the interfacing mediums, and h_C is the heat transfer coefficient, HTC. The HTC can be found with numerical simulation tools, or be calculated from known empirical expressions. The later was utilized in this model, and a compilation of expressions used is found in table 3.3.

Airgap

For convection through the airgap, equation (3.5) was used.

$$h_C = \frac{Nu\lambda_{air}}{D_h} \tag{3.5}$$

where Nu is the Nusselt number and λ_{air} is the thermal conductivity of air. D_h is the hydraulic diameter, and is for the air gap described by equation (3.6).

$$D_h = \delta\sqrt{\frac{8}{3}} \tag{3.6}$$

Where δ is the radial length of the air gap. The Nusselt number is dependent on the Taylor number, a quantity that describes the relationship between centrifugal forces and viscous forces [62]. The Taylor number can be calculated from a correlation described by equations (3.7) to (3.9).

$$Ta_m < 1700 \rightarrow Nu = 2 \tag{3.7}$$

$$1700 < Ta_m < 10^4 \rightarrow Nu = 0.128Ta_m^{0.367} \tag{3.8}$$

$$10^4 < Ta_m < 10^7 \rightarrow Nu = 0.409Ta_m^{0.241} \tag{3.9}$$

where Ta_m is the modified Taylor number, the Taylor number divided by a factor F_g to fix it as a Taylor-Couette flow. The modified Taylor number is calculated in [58] by using the factor F_g, expressed by equation (3.10).

$$F_g = \frac{\pi^4 \left(\frac{2r_m - 2.304\delta}{2r_m - \delta} \right)}{1697 \left(0.0056 + 0.0571 \left(\frac{2r_m - 2.304\delta}{2r_m - \delta} \right)^2 \right) \left(1 - \frac{\delta}{2r_m} \right)} \tag{3.10}$$

Where r_m is the average value of the radii of the stator and rotor.

Convection through the air gap is considered between stator winding, stator teeth, and rotor shoe. Figure 3.5a shows the air gap node, and figure 3.5b the speed-dependent calculation of HTC and thermal resistance inside the node. Table 3.2 shows the HTC and resistance for different speeds.

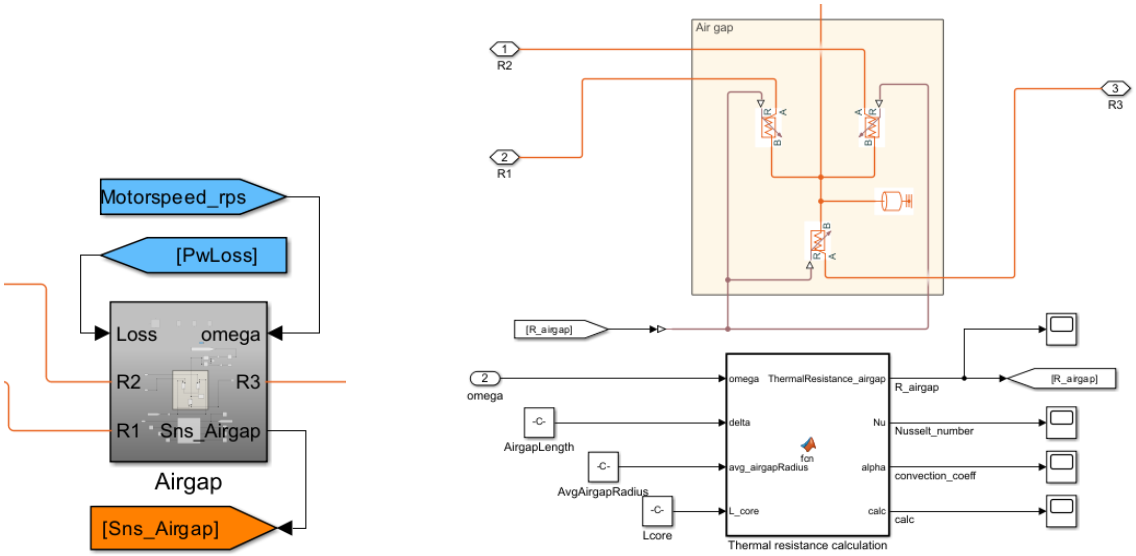

(a) Node top view. **(b)** Inside air gap node.

Figure 3.5: The thermal resistance is variable due to speed dependent convection through the air gap.

Table 3.2: Convection through the air gap is speed dependent. Table reports heat transfer coefficient and thermal resistance at different speeds.

Thermal resistance and HTC in the airgap										
Num \RPM	1000	2000	3000	4000	5000	6000	7000	8000	9000	10000
h_C	83	116	142	163	181	198	213	227	240	253
R_{airgap}	.125	.089	.074	.064	.057	.053	.049	.046	.043	.041

Internal air

Convection to the internal air is considered from the housing, end caps, stator, rotor, bearings and end windings. The thermal resistance representing each of these connections is, similarly to the air gap, calculated individually and depend on air speed. Figure 3.6a shows the internal air node, and figure 3.6b shows the block calculating the thermal resistances using the expressions compiled in table 3.3.

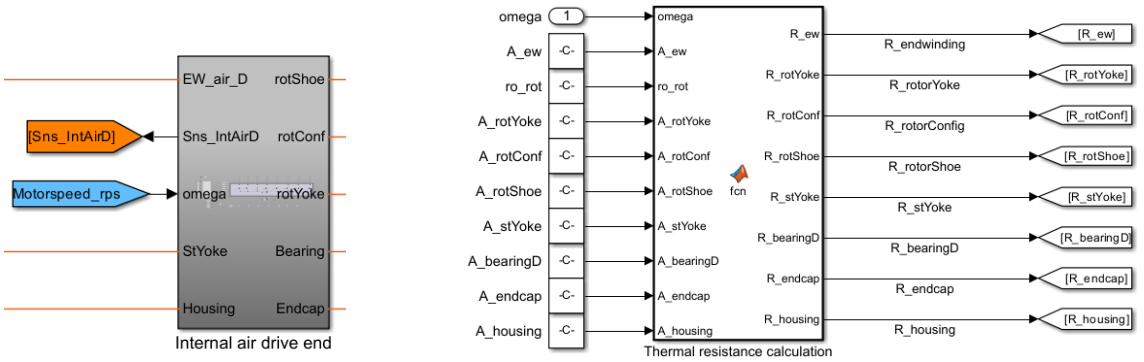

(a) Node top view. **(b)** Inside internal air node.

Figure 3.6: Variable thermal resistance in the internal air node, calculated individually for each connected component.

Housing to ambient

The convection coefficient from the motor housing to the ambient air can be quantified with analytical methods if the motor geometry and the air speed surrounding the motor is known. However, aiming to keep the model as general as possible, it is desired to find a relationship without the need for complex fluid analysis. An alternative method is presented in [63], where a relationship has been empirically found between the thermal resistance and the housing surface area for machines ranging from 1.5 kW to 1 MW. This relationship is described by equation (3.11).

$$R = \frac{0.167}{A} \tag{3.11}$$

Where R is the thermal resistance for heat transfer from motor housing to ambient air $[K/W]$, and A is the surface area $[m^2]$.

The convection to ambient is modeled by connecting the node to a constant temperature source representing the ambient, through a thermal resistance. This is shown in figure 3.7 for the housing node.

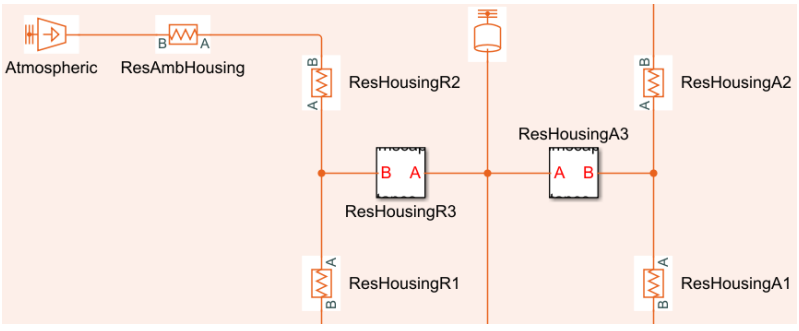

Figure 3.7: Part of the housing node, with convection to ambient in the top left corner.

Table 3.3: Heat transfer coefficient expressions for different components in contact with air.

Convection Heat Transfer Coefficient	
Component	HTC
Airgap	$h_{\text{airgap}} = \frac{\text{Nu}\lambda}{D_h}$
Internal air	$h_{\text{int}} = 15 + 6.75 \cdot u_r^{0.65}$
End windings	$h_{\text{ew}} = 41.4 + 6.22 \cdot u_r$
Rotor	$h_{\text{rotor}} = 16.5 \cdot u_r^{0.65}$
Housing	$h_{\text{housing}} = 15.5 \cdot (0.29u_r + 1)$

Where u_r is the peripheral rotor speed $[m/s]$.

Radiation

In electric machines cooled by forced convection (e.g., enclosed fan or pumped liquid), natural convection and radiation from the housing can be considered negligible [27]. This is also the case for the internal components, because the temperatures are not high enough. Therefore, radiation will not be considered a heat path in the electric machine model.

3.2.2 Thermal capacitance

The thermal capacitance $[J/K]$ for each node is the product of the node's mass and the specific heat capacity of the material. The mass is calculated by the product of the component volume and the density of the applied material. This is summarized in equation (3.12). Physical data for the materials used in the model is given in table 3.4, and for fluids in table 3.5. The fluid properties are built into Simscape, and hence the presented values are approximated from this dataset for reference.

$$C_{th} = m \times c_p = V \times \rho \times c_p \tag{3.12}$$

Where C_{th} is the thermal capacitance $[J/K]$, m is the mass $[kg]$, c_p is the specific heat capacity $[J/kgK]$, V is the volume $[m^3]$ and ρ is the density $[kg/m^3]$.

Table 3.4: Material data for solid parts considered in the model. If relevant, thermal conductivity is separated in axial and radial components.

Material data - solids.				
Material	Density [kg/m^3]	Specific heat [J/kgK]	Thermal conductivity [W/mK]	Node
Aluminium	2700	960	135	Housing, endcaps
Core steel	7600	[-]	ax: 0.24 rad: 19.8	Stator core, rotor core
Copper	8960	376	ax: 386 rad: 1.1	Active-/ and end windings
PM	7500	450	8	PM
Steel	7800	460	40.5	Shaft
Bearings	7800	460	[-]	Bearings
Insulation	[-]	[-]	0.26	Active-/ and end windings
Potting	1766	[-]	[-]	End windings

Table 3.5: Material data for fluids considered in the model. The coolant considered is a mixture of ethylene glycol and water, mixed 50/50 by volume.

Material data - fluids.					
Material	Temperature [K]	Density [kg/m^3]	Specific heat [J/kgK]	Thermal conductivity [W/mK]	Dynamic viscosity [Pa · s]
Coolant	293.15	1085	3358	0.416	0.00463
	308.15	1075	3450	0.412	0.00256
	323.25	1064	3529	0.407	0.00156
Air	298.15	1.225	1000	0.030	$1.8 \cdot 10^{-5}$

3.2.3 Losses

For each node with an inherent loss, the loss is applied to the node in the form of a heat flow (as shown in figure 3.3, indicated at (1)). The heat power to apply is determined either from tabulated data in the case of electrical and bearing losses, and analytical calculations for friction loss in the air gap (see equation (3.18) to (3.21)). Bearing losses are tabulated depending on speed, torque and temperature. The electrical losses are retrieved from lookup tables depending on the motor torque, speed and voltage, illustrated in figure 3.8 below. The tabulated loss maps were compiled by the electromagnetic design team at Polestar, and calculated from FEA software. The losses were divided in separate maps for stator and rotor iron loss, active winding and end winding copper loss, magnet loss and bearing losses. To separate the iron losses by stator yoke/teeth and rotor yoke/shoe, it was assumed that the losses are uniformly distributed as reported in [64]. Therefore, a gain factor

proportional to the volume of the node per the total volume was used, according to eq. (3.13)-(3.16).

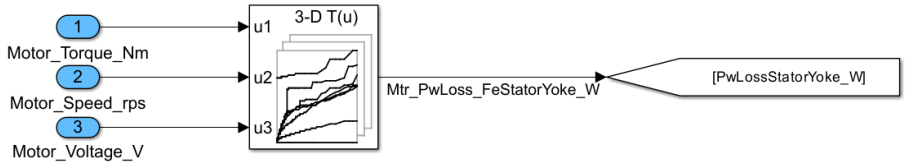

Figure 3.8: Losses retrieved from 3-D lookup tables depending on motor operating point in terms of speed, torque and voltage.

$$\text{FeStatorTeeth\_ratio} = \frac{V_{\text{stator\_teeth}}}{V_{\text{stator}}} \tag{3.13}$$

$$\text{FeStatorYoke\_ratio} = 1 - \text{FeStatorTeeth\_ratio} \tag{3.14}$$

$$\text{FeRotorShoe\_ratio} = \frac{V_{\text{rotor\_shoe}}}{V_{\text{rotor}}} \tag{3.15}$$

$$\text{FeRotorYoke\_ratio} = 1 - \text{FeRotorShoe\_ratio} \tag{3.16}$$

Where each respective volume is calculated from the motor dimensions. Separation between stator yoke/teeth is illustrated in figure 3.9a, and the separation between rotor yoke/shoe in figure 3.9b.

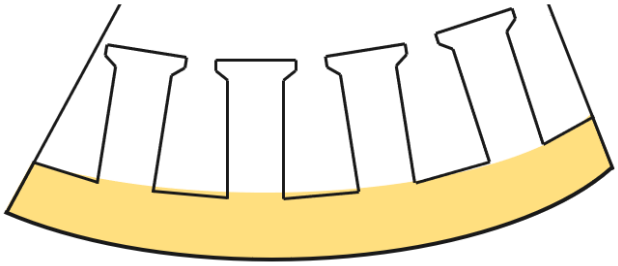

(a) Cross section of stator; yoke marked in orange, teeth in white.

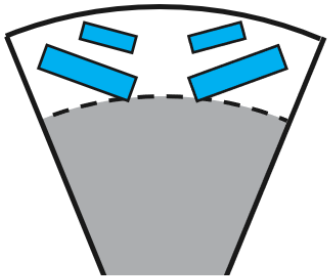

(b) Cross section of rotor; yoke marked in grey, shoe in white minus the volume of magnets, shown in blue.

Figure 3.9: Definitions used to divide stator by yoke/teeth and rotor by yoke/shoe.

As discussed in section 2.1.2.1, the copper losses change with temperature according to the change in winding resistance. A rough compensation factor was applied according to equation (3.17) [25].

$$Q_{Cu} = (1 + \alpha \cdot (T - T_{ref})) \cdot Q_{Cu_{ref}} \tag{3.17}$$

Where Q_{Cu} is the compensated power loss, α is the temperature coefficient of copper (=0.0039), T is the node temperature, T_{ref} is the temperature at which the original

loss $Q_{Cu_{ref}}$ is calculated.

Gas friction from the high-speed rotor motion generates friction losses in the air gap, and can be calculated from equation (3.18) [58]

$$P_{\text{fr}} = k_1 C_T \rho \pi \omega^3 r^4 l \tag{3.18}$$

Where k_1 is a roughness coefficient, C_T is the torque coefficient, ρ is the air mass density, ω is angular velocity, r is the average air gap radius and l is the rotor length. The roughness coefficient, k_1, is 2.5 for an axially slotted surface (the stator), and the torque coefficient is determined from equation (3.19).

$$C_T = \begin{cases} 0.515 \frac{(\frac{\delta}{r})^{0.3}}{\text{Re}_\delta^{0.5}} & \text{if } 500 < \text{Re}_\delta < 10^4 \\ 0.0325 \frac{(\frac{\delta}{r})^{0.3}}{\text{Re}_\delta^{0.2}} & \text{if } 10^4 < \text{Re}_\delta \end{cases} \tag{3.19}$$

$$Re_\delta = \frac{\rho u \delta}{\mu} \tag{3.20}$$

$$u = \omega \times r \tag{3.21}$$

Where Re_δ is the Couette-Reynolds number taking the enclosing stator into account, u is peripheral rotor speed, μ is the fluid dynamic viscosity and δ is the air gap length.

3.2.4 Cooling

The considered EESM motor is cooled with oil flowing through ducts in the stator core, while the PMSM motor is cooled by a coolant flowing through coolant jackets in the housing. Since the model of the EESM cooling system could not be verified, as further described in section 3.2.5 below, it is not presented here.

The cooling system model for the PMSM has two parts, as shown in figure 3.10. The first part is the coolant supply system, consisting of the coolant pump, tank and pipes. The second part models the jackets within the motor housing. For reference as to the location of the coolant jackets in the machine, refer to the illustration in figure 2.3.

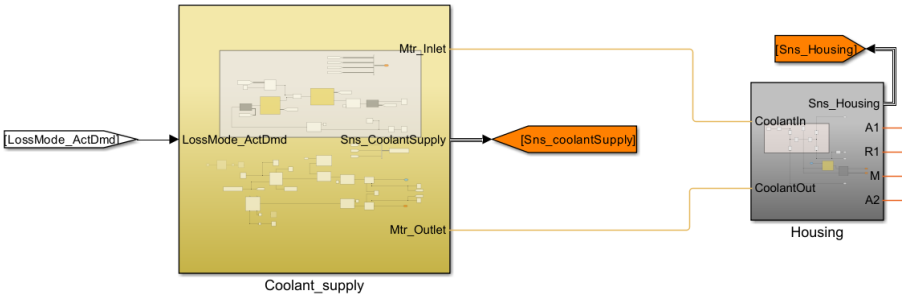

Figure 3.10: The two parts of the PMSM cooling system, supply and jackets in the housing.

The coolant supply part is further described by figure 3.11. From the top left corner, the inlet boundary conditions are set, along with a definition of the liquid. The pump is controlled by a signal demanding a specified flow rate, before pumping the fluid into the housing jackets through the supply outlet port marked in blue. After circulating in the housing, the coolant returns through the port marked in orange and is accumulated in a tank.

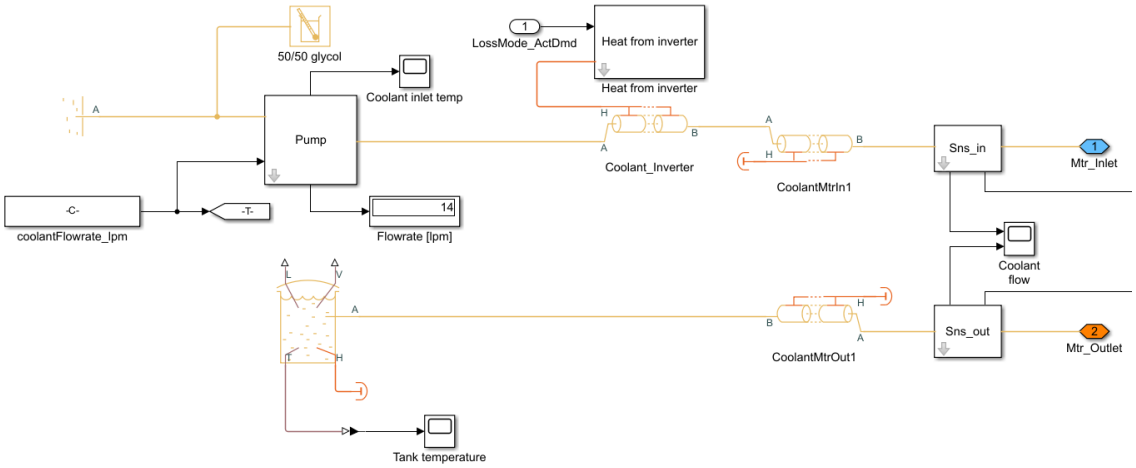

Figure 3.11: The coolant supply system sets liquid properties, boundary conditions and pumps the coolant into the motor housing.

The coolant jackets within the motor housing is connected to the thermal domain of the housing node, as described by figure 3.12a. The blue and orange coloured ports correspond to the same ports as the supply system in figure 3.11. The coolant jackets are individually modeled as shown in figure 3.12b, since they have different dimensions and hence different flow capabilities.

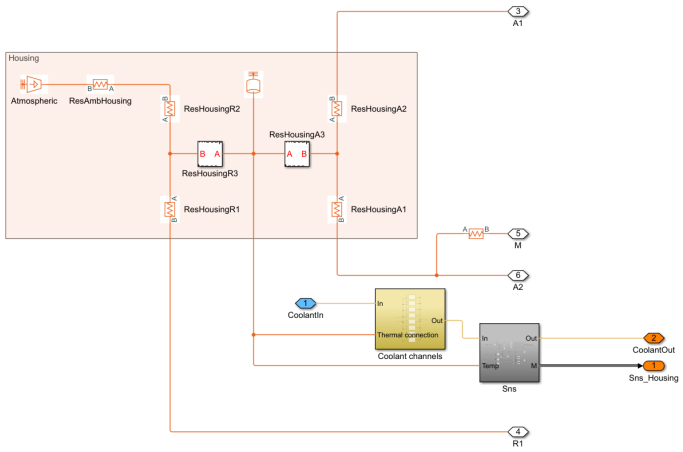

(a) The thermal domain of the housing node is integrated with to the thermal liquid domain of the coolant.

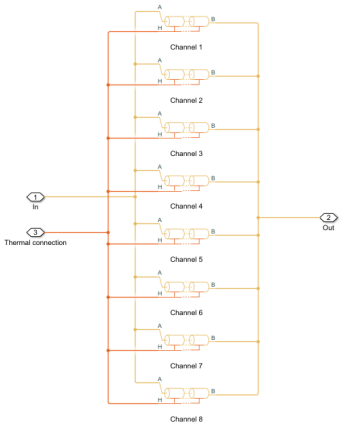

(b) The jackets around the housing are individually modeled.

Figure 3.12: The coolant system connects to the motor housing node.

3.2.5 Verification

It was determined some time into the project that there would be insufficient test data available to verify the EESM model. For that reason, focus shifted to the considered PMSM concept for which test data was available.

The PMSM model was verified by comparison with test data from two different test setups. To verify the steady-state performance of the model, it was compared to test data running at constant speed and torque for 30 minutes. The results of the steady-state validation are reported in section 4.1.1. To verify the transient performance of the model, it was compared to test data running the WLTC cycle, described in section 2.4.2. In this case, the test was performed in a complete ERAD setup, hence increasing the available heat paths from the electric machine to other components. The results of the transient validation is reported in section 4.1.2.

3.3 Vehicle thermal model

To allow for further simulations, the losses from the EM thermal model must be implemented in a thermal model of the vehicle. This regards power heat utilization to fulfil the aim of improving the energy consumption of heating the cabin of the vehicle. This was done by creating a thermal model to use together with the created model of the motor, using an already existing thermal model made by Polestar as inspiration.

3.3.1 Existing model

The existing model of the thermal part of the vehicle consists of a conventional thermal management system with four different blocks representing thermal components and an additional block for control of valves of the thermal liquid through the system. Figure 3.13 shows a simplified model of the existing vehicle thermal model.

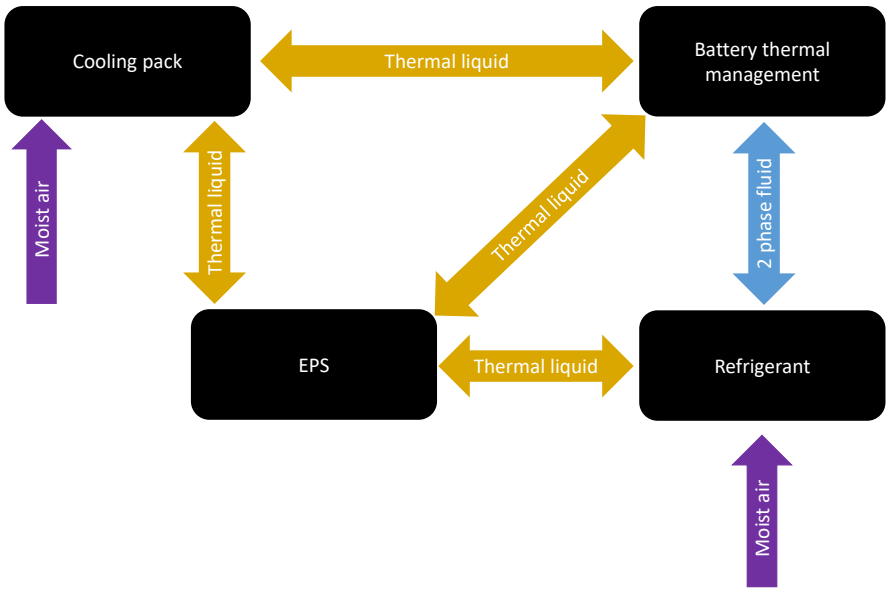

Figure 3.13: Simplified schematic of already existing thermal block.

As seen in figure 3.13, the main components in the existing thermal model are a cooling pack, the refrigerant cycle, and a block for battery thermal management. The cooling pack is a heat exchanger between a cooling fan and the thermal liquid going through the system. The battery thermal management block has a two-phase fluid as input from the refrigerant and then outputs warmer thermal liquid. The cooling pack and battery thermal management block are of less interest in the matter of this thesis, while the electric propulsion system, EPS, and refrigerant cycle are of higher importance.

The EPS has thermal liquid as input and output between all three other blocks as it is the system, together with the battery, that needs heating or cooling. It consists

of the thermal input from both the front and rear motor and is possible to control depending on the temperature demands for the motors.

The refrigerant cycle is a conventional one similar to what was described in section 2.3.1. It consists of a compressor, condenser, evaporator and chiller that are connected through two-phase fluid and uses air or thermal liquid for cooling or heating of the different components.

3.3.2 Vehicle thermal management model

To allow for implementation of the LPTN model into the existing vehicle model, a new thermal model was made. This model was based on an electric vehicle thermal model example from [65]. The already existing thermal model described in section 3.3.1 was also taken into consideration when creating the new thermal management model on vehicle level.

In the same way as for the already existing thermal model illustrated in figure 3.13, the refrigerant cycle in the new model is a conventional cycle for cabin heating of BEVs, as described in section 2.3.1, where modifications have been made to fit the aim of this thesis. This refrigerant cycle includes a radiator, chiller, evaporator and condenser. Other components in the thermal management model are a loop for battery heating, a block for the propulsion system and a loop for the heating of the cabin. The complete model of the thermal management on vehicle level is shown in figure 3.14. Every component has its own block, which are the white rectangles with the name of the component inside. The blocks are connected by the different Simscape domains, as described in section 3.1.1.

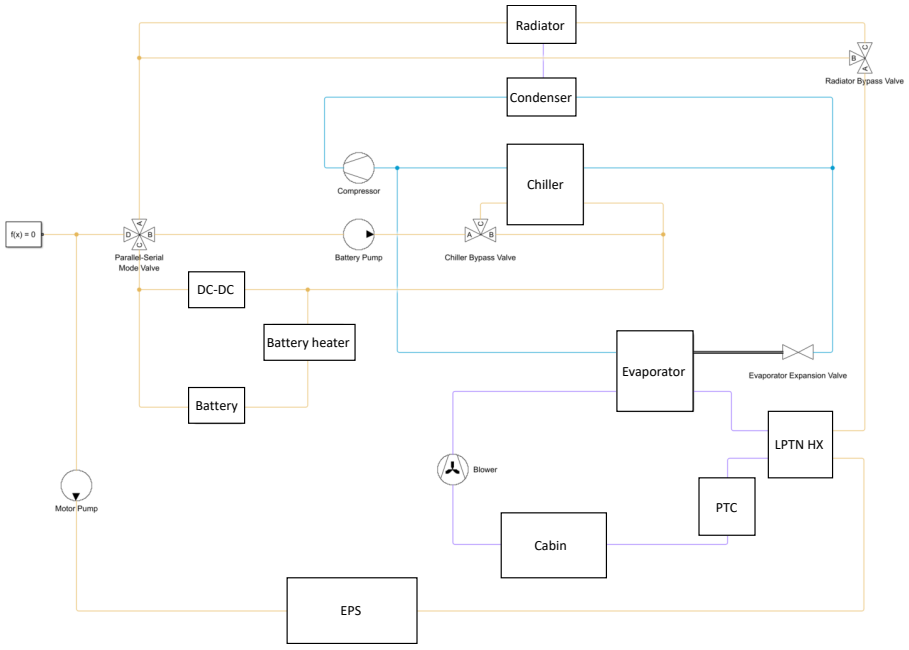

Figure 3.14: Complete vehicle thermal management model.

The battery heating loop, shown in figure 3.15, consists of one block for the DC-DC converter, one for the battery heater and one for the battery. When the battery needs to be cooled, a valve routes the coolant through the chiller to cool it down and then into the battery components to reduce their temperature. If the battery instead needs to be heated, the valve bypasses the chiller and the heater is switched on to heat up the battery to its desired temperature.

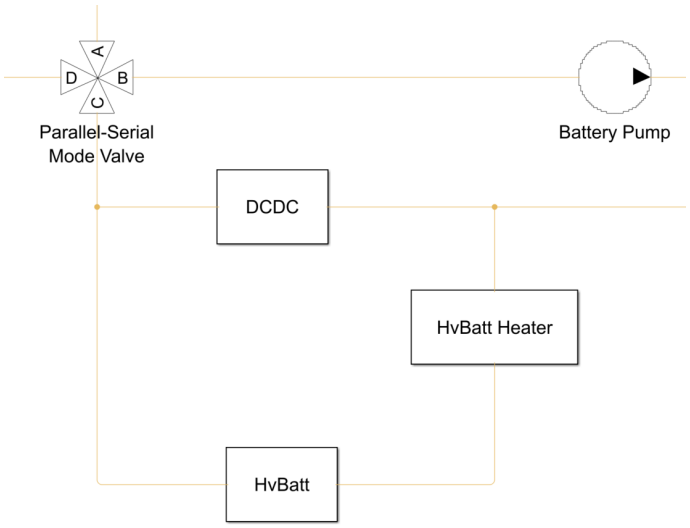

Figure 3.15: Battery heating loop.

The DCDC block consists of a lumped thermal mass representing the mass of the DC-DC converter, a heat flow rate source that inputs the heat set by the user, and a pipe that transfers the heat from the thermal domain to the thermal liquid in the system. The thermal liquid represents the liquid that is cooling the warm components in the model. The battery heater block inputs a heat flow rate with a maximum power of 500 W. It has a lumped mass representing the mass of the heater and transfers the heat through convection into the air volume of the heater. In the battery block, a heat flow representing the temperature increase in the battery is transferred through a pipe into the thermal liquid in the system.

Before the EPS block, a pump moves the thermal liquid. The inside of the block of this pump is shown in figure 3.16. It contains a fixed-displacement pump and an ideal angular velocity source that is controlled by a command signal.

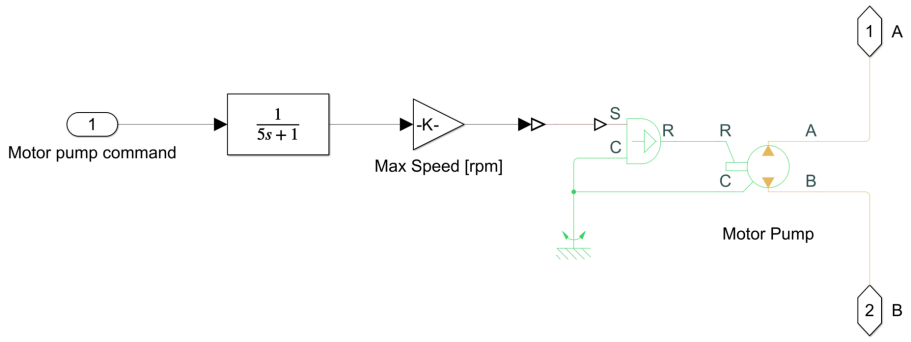

Figure 3.16: Motor pump block.

The EPS, Electric Propulsion System, block consists of the charger, motor and inverter, as shown in figure 3.17. The thermal liquid flows through these components and is heated up by the waste heat generated by them.

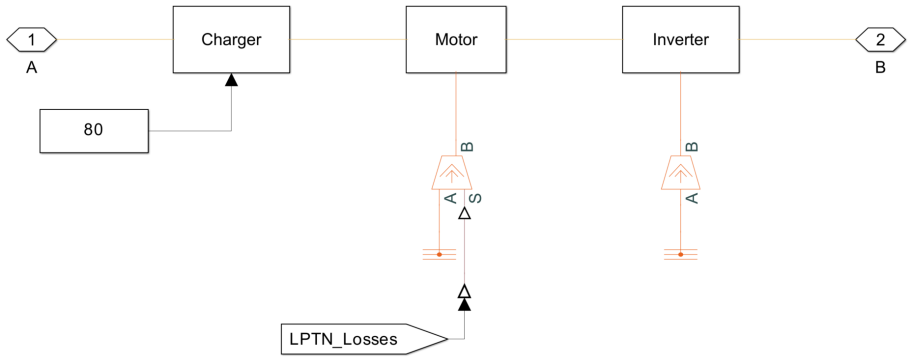

Figure 3.17: Electric Propulsion System, EPS, block.

All three blocks consist of a heat flow going into the block, a thermal mass representing the mass of the component and a pipe transferring the heat to the thermal liquid. This is shown in figure 3.18. The heat produced by the charger is constant and set by the user, while the heat into the motor and inverter comes from the measured losses from these two components when running the selected driving cycle. The motor heat losses only come from the rear motor. If the vehicle has both a front and rear motor, it would be possible to repeat the process of modeling the front motor and utilize the heat losses from that one as well.

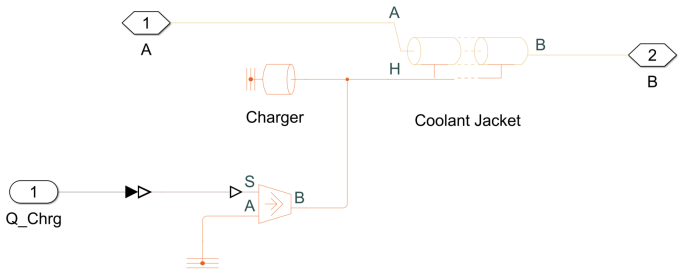

(a) Charger.

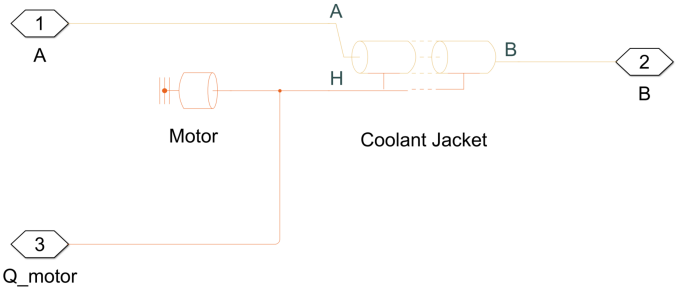

(b) Motor.

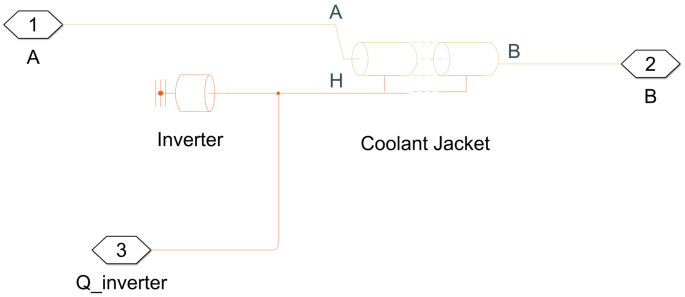

(c) Inverter.

Figure 3.18: Inside of the three blocks in the EPS block.

The losses in the motor comes from the motor block in the model described in section 3.2, where the LPTN block is placed. The losses from the motor come from the loss maps block in the LPTN block, where all losses that come from the loss maps have been summed up into a variable. This block is shown in figure 3.19.

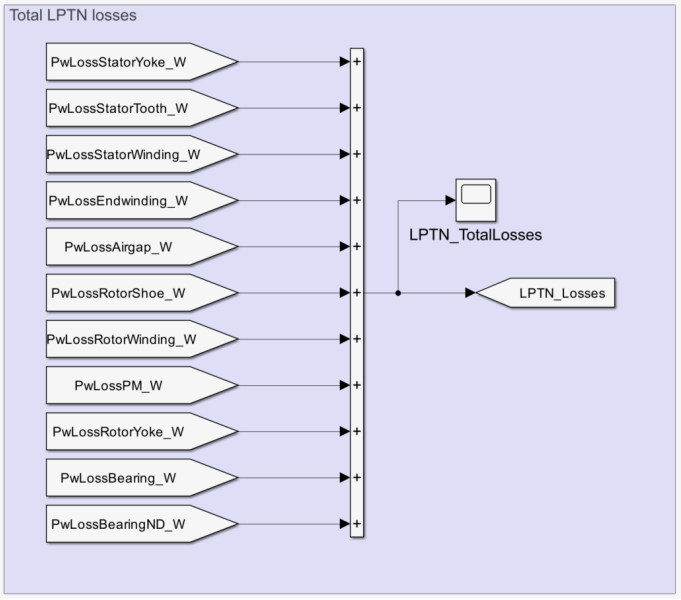

Figure 3.19: Block for summing up all losses from LPTN.

After being heated by the EPS block, the thermal liquid passes through a heat exchanger with the cabin air, where heat is transferred from the thermal liquid to the air to heat it up. A zoomed in view of the loop for the cabin heating is shown in figure 3.20.

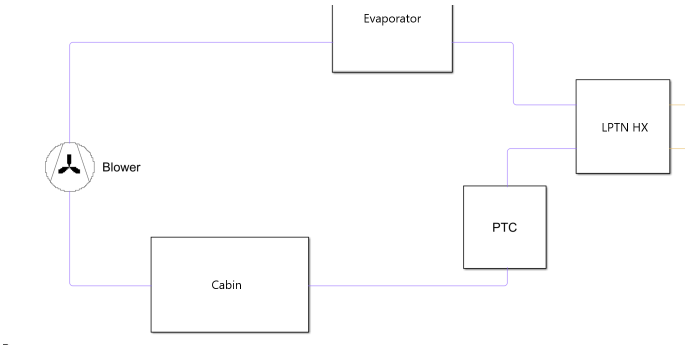

Figure 3.20: Cabin heating/cooling air loop.

Inside the heat exchanger block is a heat exchanger between air and thermal liquid, shown in figure 3.21, as well as a control system for when to use the heat exchanger. This is done by measuring the temperatures of the air and thermal liquid and controlling when the thermal liquid should flow through the heat exchanger to heat up the air. As this should only be used for heating up the air with the thermal liquid, and not the opposite, the thermal liquid only goes through the heat exchanger when it is warmer than the air. This is done by subtracting the temperature of the air from the temperature of the thermal liquid. When this value is negative, a 3-way directional valve opens the way past the heat exchanger to avoid temperature exchange and therefore avoid the air to heat up the motor. On the other hand, when the output from the temperature subtraction is positive, the valve opens the way through the heat exchanger, which makes the thermal liquid heat up the air.

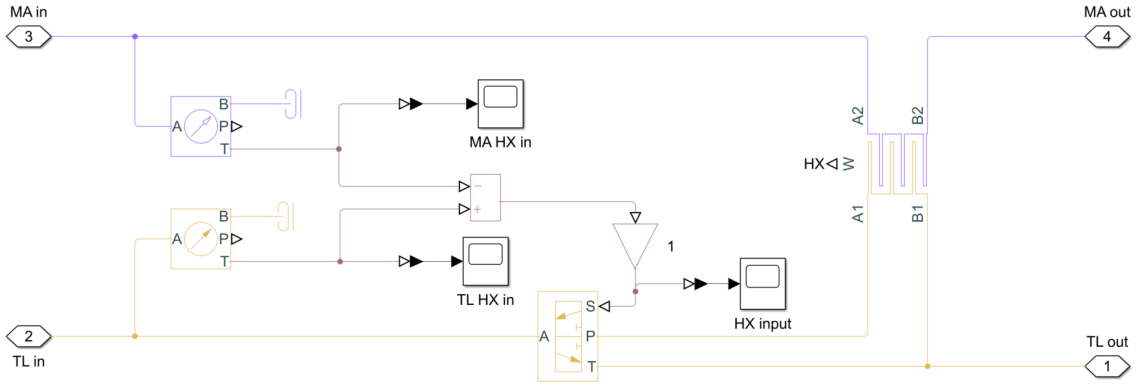

Figure 3.21: Heat exchanger block between thermal liquid out of EPS and air into cabin.

The heated air then passes through the PTC heater, where the air is heated additionally if needed to reach the cabin setpoint temperature. This block consists of a power input, a lumped mass representing the mass of the heater, and a convective heat transfer heating up the cabin air. The block is shown in figure 3.22.

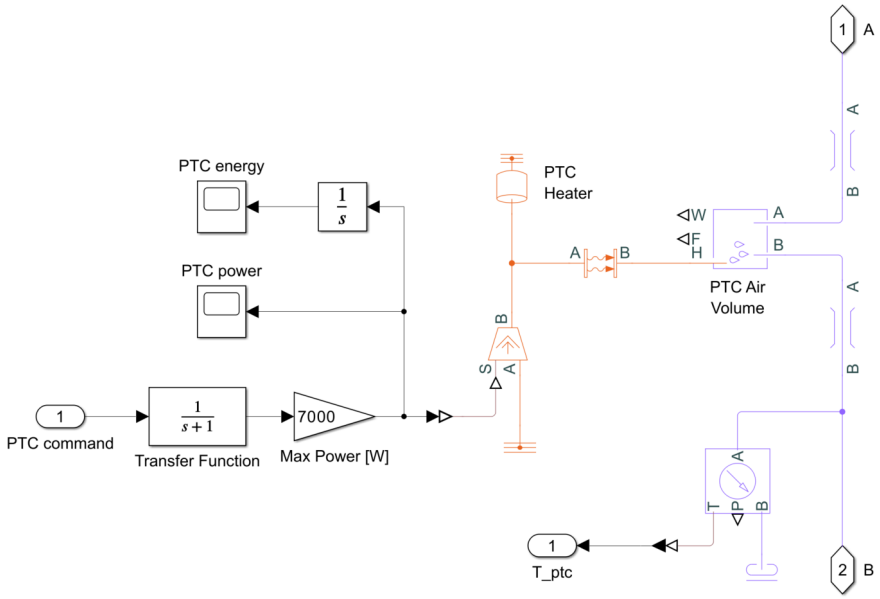

Figure 3.22: PTC heater block.

Depending on how much heat is brought to the air in the cabin loop, the PTC heater must be used more or less. The way to measure the energy that is saved by utilizing the waste heat to heat up the cabin is therefore to measure the energy consumed by the PTC heater. This is done by integrating the power consumption over time to get the total consumed energy. This value is then possible to compare to the value of the consumed power of the PTC heater when the waste heat is not utilized to aid the heating of the cabin.

The warm air then proceeds into the cabin, which consists of an air volume representing the volume of the cabin. The warm air goes into the volume and is cooled down by the environmental air and heat transfer through different parts of the car, like the windows and the doors. Heat generated from for example solar power and the passengers has also been taken into consideration, as well as a small leakage of air out of the cabin. Figure 3.23 shows the cabin model with the leakage to ambient, while the heat transfer in the cabin has been omitted.

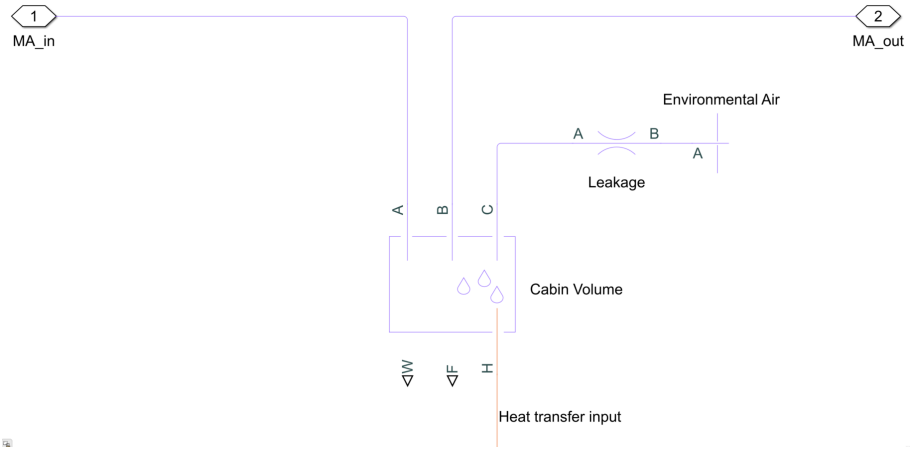

Figure 3.23: Cabin block, excluding cabin heat transfer model.

The blower controls the flow of air that goes into the cabin and the block is shown in figure 3.24. It is placed just after the cabin and consists of a volumetric flow rate source with a maximum flow rate of $0.3m^3/s$. There is also a recirculation flap that either takes the air that comes out of the cabin and accelerates its flow to go through the loop of air, or takes air from the outside environment and blows it into the loop. Whether recirculation is wanted or not can be set by the user. It is set to be off when simulating the cold weather situations as it would be inefficient to always take in new, cold air into the cabin and heat it up.

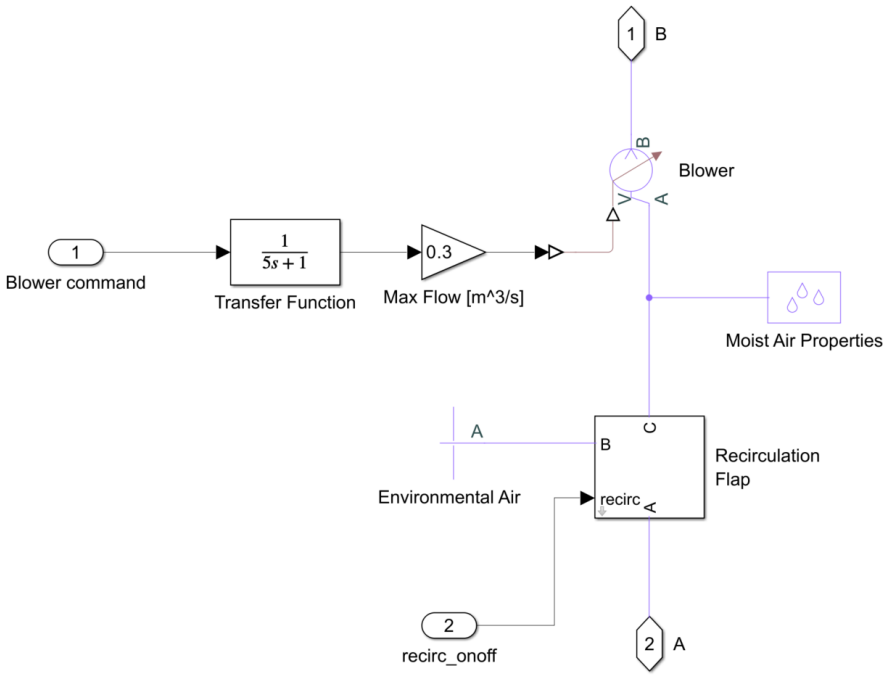

Figure 3.24: Cabin air blower.

There is also an aspect of cooling the battery, motor and cabin implemented in the model, even if it is not the focus in this thesis, which is on heating the cabin. It is still included to make the model representative of a real world system, which gives more accurate results in the end. A zoomed in view of it is provided in figure 3.25 to get an overview of the refrigerant cycle loop that is cooling the battery and cabin.

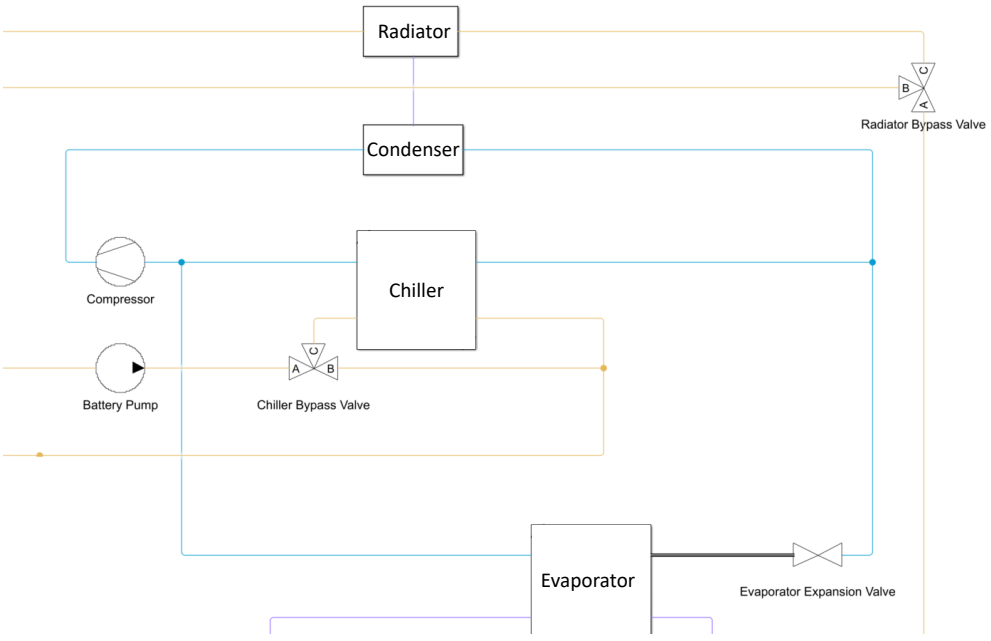

Figure 3.25: Refrigerant cycle loop.

When the thermal liquid exits the heat exchanger for heating the cabin, it passes

through a valve to either go through the radiator or not. The radiator is a heat exchanger between the environmental air and the thermal liquid, where the environmental air that comes out of the exchanger goes into the condenser. The condenser, that is a heat exchanger between the air and the refrigerant, condenses the warm refrigerant and in that way cools it down with the air coming from the radiator. There is also a fan that drives the flow of ambient air between the radiator and condenser.

Before the condenser, a compressor is placed to increase the pressure, and therefore temperature, in the refrigerant going into the condenser. The compressor contains a mass flow rate source that is controlled by a compressor map. The map takes the pressure of the evaporator and condenser into consideration to control the mass flow rate of the compressor. After the condenser, the cooled refrigerant goes through the chiller and evaporator that are connected in parallel. Before going into the evaporator, an expansion valve reduces the pressure of the refrigerant, which means that its temperature is also decreased. The cold refrigerant enters the evaporator that exchanges its heat with the air coming out of the blower and is on its way into the cabin. The air is then heated up while the refrigerant is cooled down. The refrigerant that goes through the chiller first goes through an expansion valve so that its pressure is decreased. The refrigerant is now colder than before and goes through a heat exchanger with the thermal liquid that then goes to the battery to cool it down.

If the battery is cold enough, a chiller bypass valve drives the flow of thermal liquid past the chiller and directly to the battery so that the battery is not cooled. This valve consists of a 3-way directional valve where a command signal decides if the thermal liquid should go through the chiller or not. Before the chiller, or just before the battery loop if the chiller is bypassed, is a pump that drives the flow of the thermal liquid. This is done with a fixed-displacement pump and a command signal that inputs a speed into an ideal angular velocity source that then drives the pump.

3.3.2.1 Thermal management control

To be able to manage the thermal system, a control part is included in the thermal management model. The control is divided into four different parts; control of the fan, cabin air, coolant loop and compressor.

The fan control is used to run the fan that is placed in the condenser depending on the temperatures of the environment, motor and inverter, as well as the pressure in the condenser. An overview of the fan control block is shown in figure 3.26. Relays and look-up tables use the mentioned inputs to output the desired fan speed. The fan runs when the cabin is being cooled or when the inverter and motor gets too warm and also need to be cooled.

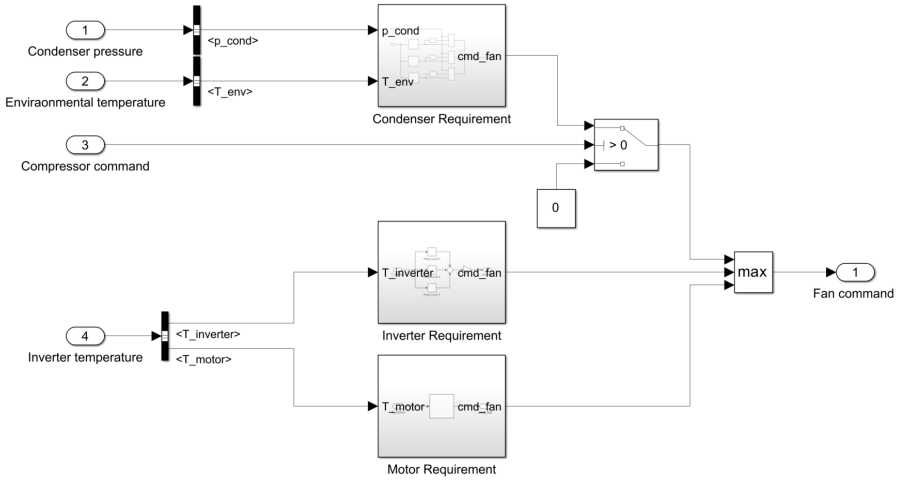

Figure 3.26: Fan control loop block.

The cabin air control states the commands to the blower and the PTC heater. In other words, it controls the air loop of the cabin by the mass flow of the air and how much it should be heated before entering the cabin. The block is shown in figure 3.27. The measured temperatures to decide the output commands of the blower and PTC heater are the temperatures of the cabin, setpoint temperature by the user, environment and PTC.

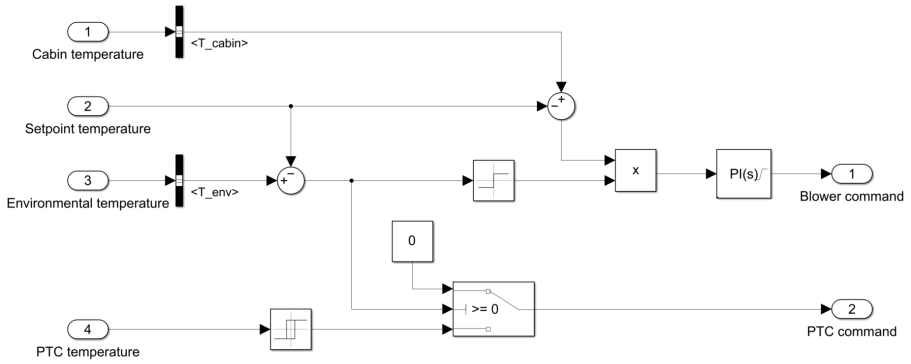

Figure 3.27: Cabin air control loop block.

The coolant loop control outputs the commands to the battery heater, motor pump, battery pump, the valve that controls if the coolant circuit should run in parallel or serial mode, as well as the radiator bypass valve. This control is made by using the measured temperatures of the environment, battery coolant, battery, motor and inverter coolant. By relays with temperature intervals of the components, these commands are then controlling the outputs to be on, off or a certain value. Figure 3.28 shows the block of the coolant loop control.

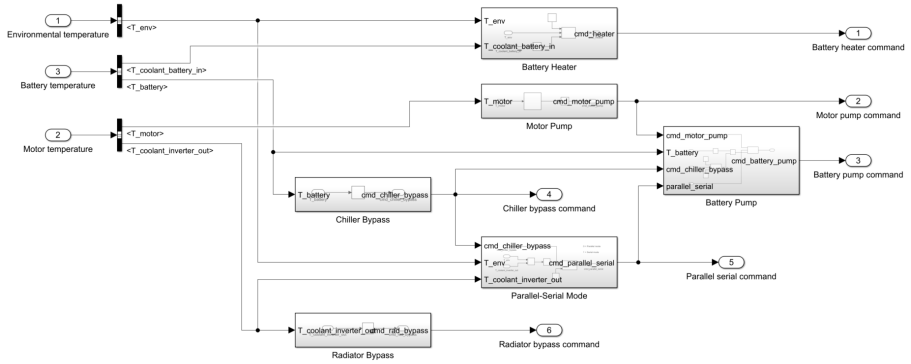

Figure 3.28: Coolant loop control block.

The compressor control outputs the command of the AC compressor by measuring the pressures in the evaporator and chiller as well as if the chiller is being used and if the AC is turned on or off. As the AC only is being used for cooling the cabin, it is not relevant when the outside air is cold and the aim is heating up the cabin. The control block of the compressor is shown in figure 3.29 below.

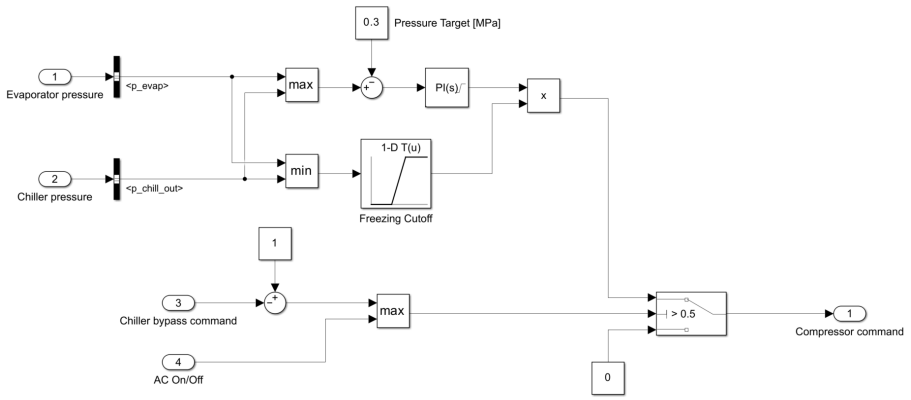

Figure 3.29: Compressor control block.

3.4 Powertrain heat utilization

The vehicle thermal model was run with different configurations and losses from the LPTN model. The model was run with the variant of the NEDC described below, in section 3.4.1 as well as the WLTC described in section 2.4.2. For comparison, the test was run in three different configurations; with neither losses nor preheating, with only EM losses but still no preheating, as well as with both EM losses and preheating.

3.4.1 Variant of NEDC

The first simulations were run with a variant of the NEDC. The cycle consists of the last 600 seconds of the normal NEDC cycle, described in section 2.4.1, taken 10 times successively. The velocity profile is illustrated in figure 3.30. These last 600 seconds of the NEDC consists of both the cycle with the lower peak for urban conditions, as well as the last high speed section for extra-urban driving. The cycle is 6000 seconds long, which corresponds to 1 hour and 40 minutes of driving.

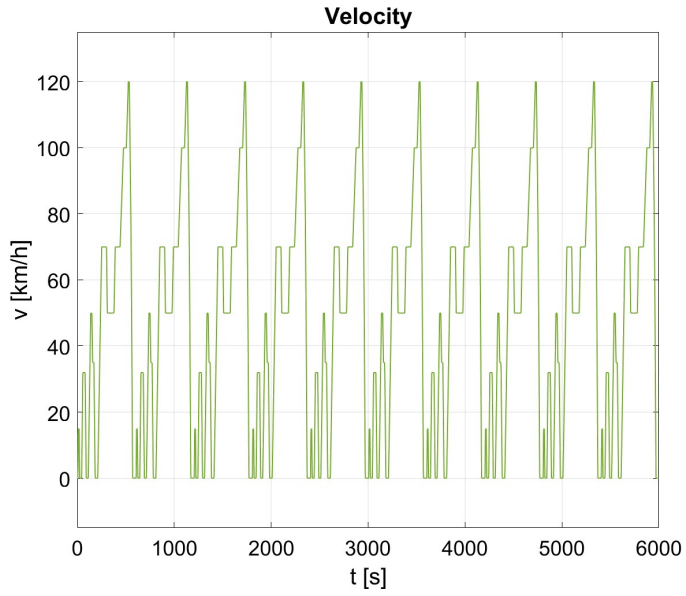

Figure 3.30: Velocity curve of variant of NEDC for initial testing of powertrain heat utilization.

The cycle therefore has sections of accelerations which generates thermal losses, which is wanted when initially running the tests and utilizing the thermal losses to heat up the cabin. This is due to the many high-speed peaks with quick accelerations.

3.4.2 Key parameters

The key parameters used during the simulations in this thesis are listed in table 3.6 below. The parameters are possible to modify, depending on the conditions that are wanted to simulate in future work.

Table 3.6: Key parameters of vehicle thermal model simulation.

Parameter	**Value**	**Unit**
Ambient temperature	-10	°C
Cabin setpoint temperature	20	°C
Initial motor temperature (without preheating)	-10	°C
Max PTC heater power	7000	W
Motor configuration	PMSM	-

4

Results

This chapter describes the results of the project by presenting the simulation results of the developed models. In section 4.1, the results of the thermal model of the electric machine is described, along with model verification in steady-state and during a driving cycle. A sensitivity analysis is presented, and the models response to some common driving cycles is reported. Finally, loss-mode operation is discussed. Section 4.2 describes the initial simulation results from the model for thermal management of the complete vehicle, regarding heating of the cabin, power and energy consumption by the PTC heater and the temperatures of the EPS components. Finally, section 4.3 describes the results of thermal management utilizing heat from the electric drive unit, both with and without a loss-mode strategy. The same aspects as in the previous chapter are considered, but simulated with different driving cycles and heat utilization configurations. The results are shown and discussed and the results from the different driving cycles as well as heat utilization configurations are compared.

4.1 EM thermal model

The developed lumped-parameter model consists of a network of 17 nodes. An illustration of the model is displayed in figure 4.1.

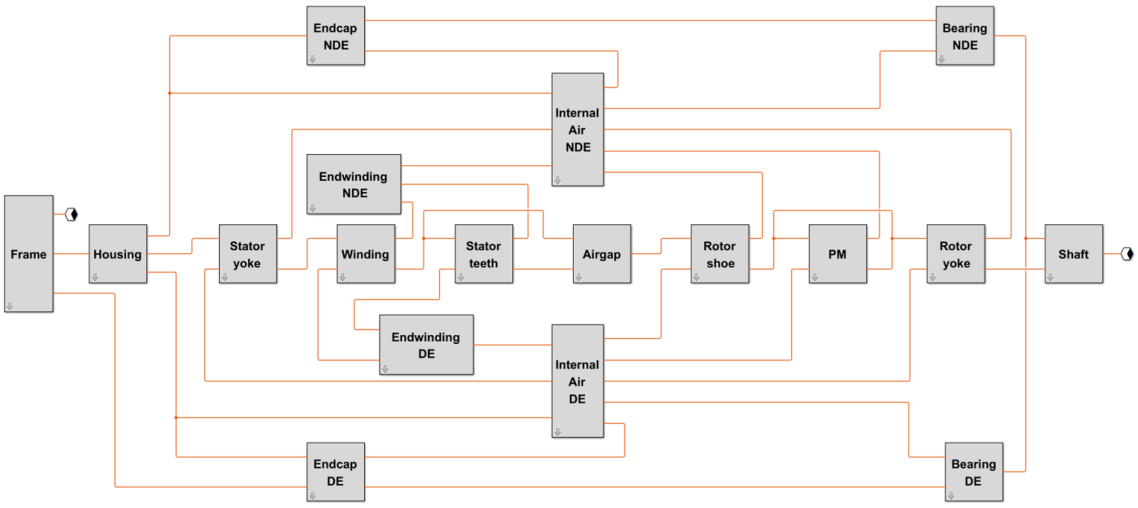

Figure 4.1: Image showing the node structure.

Each node represents a section of the motor that can be parameterized by its thermal

resistance and heat capacity. Starting from the center of the machine and moving outward radially, the components are; shaft, rotor yoke, permanent magnet, rotor shoe, airgap, stator teeth, winding, stator yoke and housing. Additionally, as seen when moving axially along the machine, are nodes for end windings, bearings, end-caps and the internal air inside the housing (but excluding the airgap). The nodes in axial direction are duplicates with respect to each side of the machine, the drive-end side, DE, and the non drive-end side, NDE. Additionally, the node denoted "frame" in figure 4.1 below signifies the transmission in a complete drive unit.

4.1.1 Verification - steady-state

The steady-state performance of the model was verified by correlation with test data running a constant operating point, such that maximum allowed temperature is achieved in 30 minutes. This case is shown in figure 4.2 below.

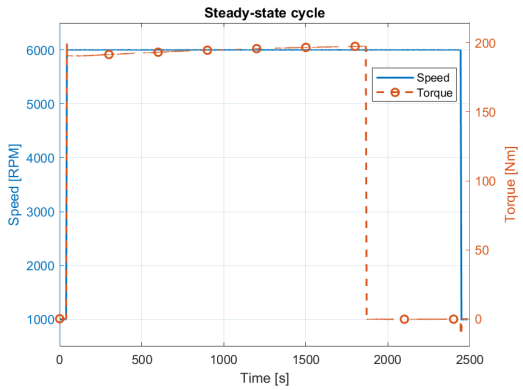

Figure 4.2: Steady-state test cycle, constant operating point during 30 min. Here shown operating at 6000 RPM & 200 Nm.

In the following figures 4.3 to 4.8, simulation results for active windings, end windings, rotor, housing, bearings and coolant are presented for each speed. Additionally, figure 4.9 and 4.10 shows the losses considered in the simulations. The subtitle to each speed-case displays the maximum relative error over the duration of the complete cycle, which is also summarized in table 4.1 in the end. Relative error is computed during each timestep, and according to equation (4.1). Finally, table 4.2 shows the relative error at the end of the cycle, i.e. when the torque steps down. Equation (4.1) is the metric commonly used in the EM thermal analysis literature, and is therefore used here for easier comparison.

$$\text{Relative error [\%]} = \frac{\text{Measured [°C] - Calculated [°C]}}{\text{Measured [°C]}} \tag{4.1}$$

Figure 4.3 and 4.4 shows active- and end windings respectively, and the results are similar. The prediction accuracy is generally higher at higher speeds, and worse at lower speeds.

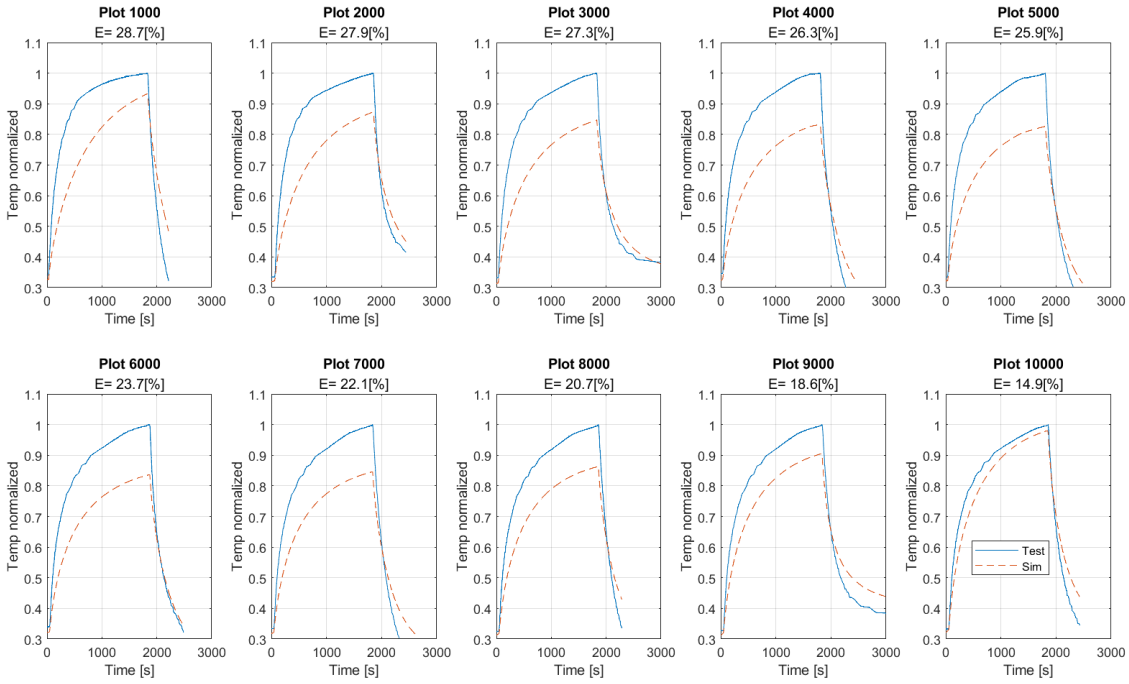

Figure 4.3: Steady-state verification - predicted temperature in the active windings.

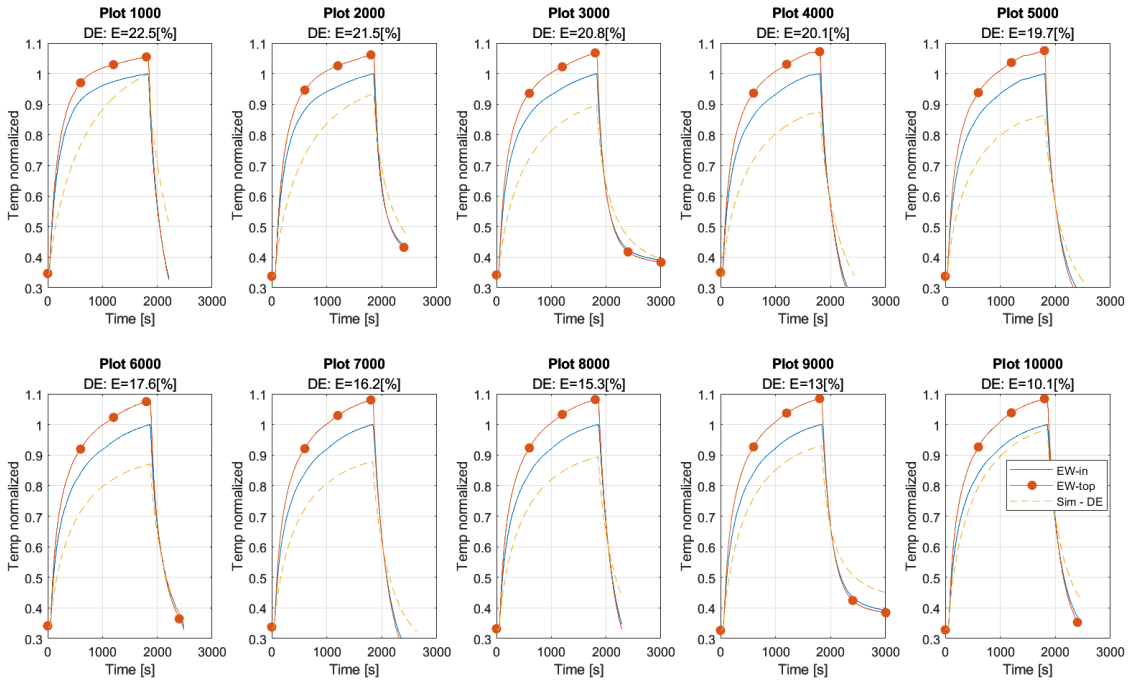

Figure 4.4: Steady-state verification - predicted temperature in the end windings.

In figure 4.4 comparing the end windings, “EW-in” refers to a temperature sensor mounted inside the end windings, whereas “EW-top” refers to a sensor mounted on the outer surface of the windings. The inner sensor position is the better match to what the model attempts to simulate, and so the error stated in the subtitles refer to the error between simulation and “EW-in”. The outer sensor measurement is included in the plot to show that it is important to keep the sensor position in mind when correlating against test data.

The trend is similar for the rotor measurement, shown in figure 4.5. The motor housing shown in figure 4.6, never reaches the measured temperature, and maintains an almost constant deviation compared to the test data. The sensor measuring this node is mounted on the inside of the motor casing pretty close to the stator iron, and this surface temperature would naturally be higher than in the lumped-mass node models. For a component such as the housing, connected to ambient air on the outer perimeter, hot air and stator iron on the inner perimeter, and a liquid coolant flowing through it, this component is difficult to verify with one single measurement. The fact that it still follows the measured trend in terms of warm-up and cool-down very well, is considered a good correlation.

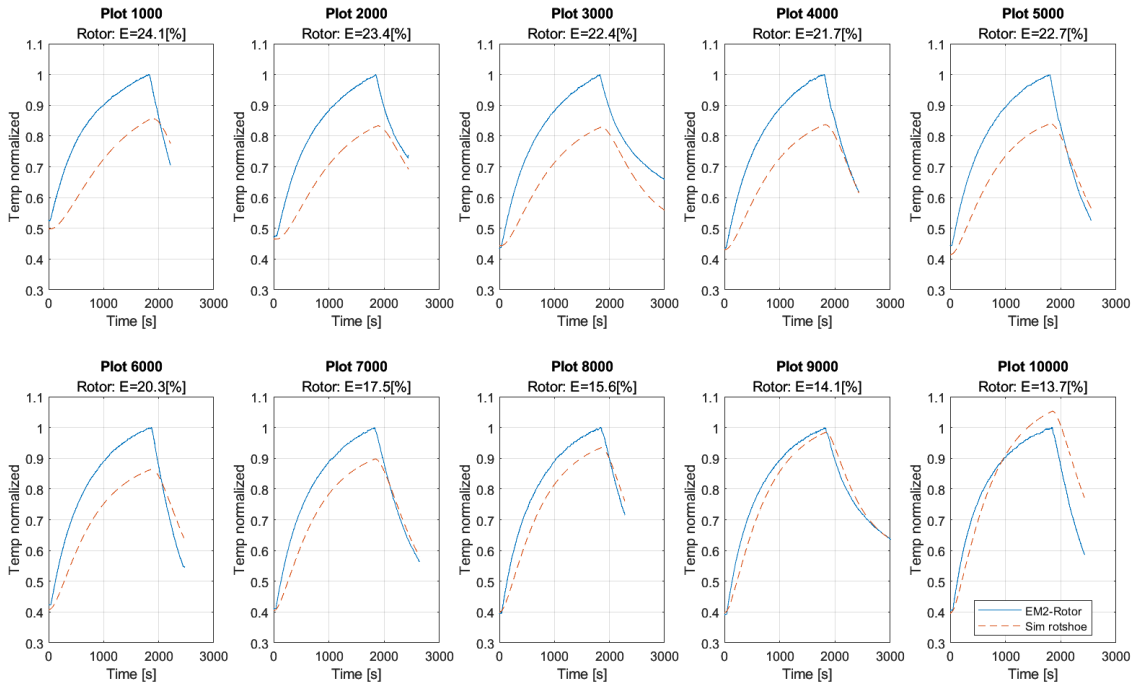

Figure 4.5: Steady-state verification - predicted temperature in the rotor.

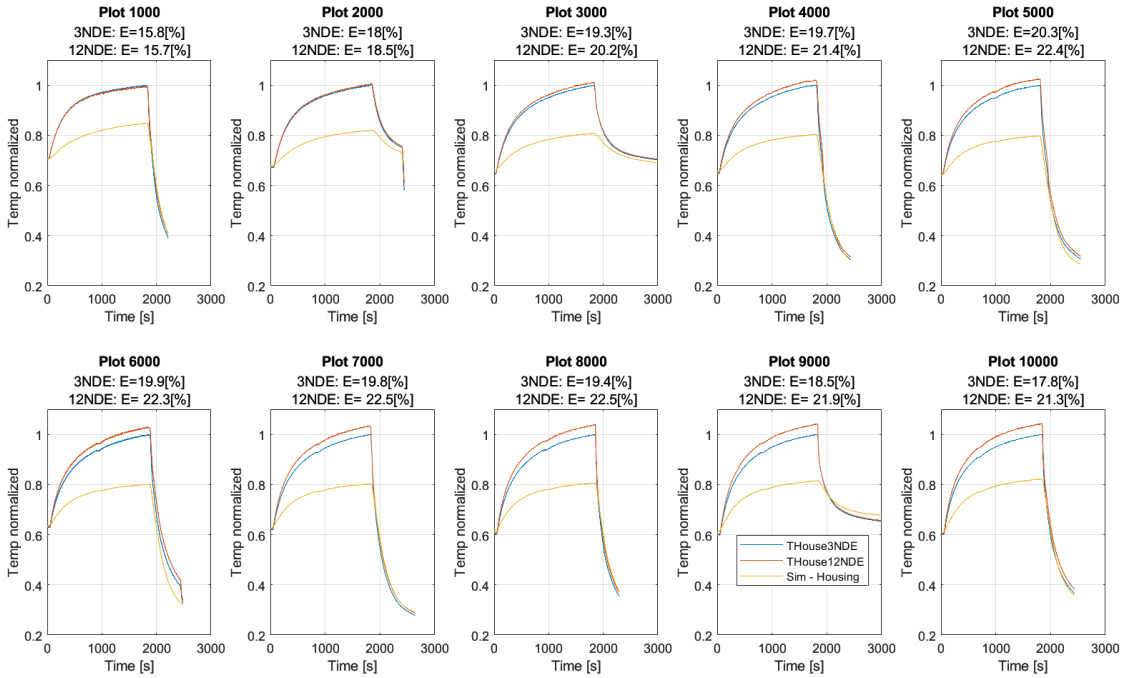

Figure 4.6: Steady-state verification - predicted temperature in the housing.

Figure 4.7 shows the simulated bearing temperature. The maximum relative error over the complete cycle measurement suggests a very poor correlation, with a maximum of almost 40% error. However, as is summarized in table 4.2, the relative error at the end of the cycle is a lot lower. This poor initial correlation could in part be explained by the deviation in initial temperature. Sensor placement should also be noted. Since the temperature sensor in the measurement is placed on the outer perimeter of the bearing, drilled into the motor housing, it naturally does not capture the same thermal mass that the node models.

The coolant temperature out of the motor is shown in figure 4.8. While the simulation correlates very well to the measurement in terms of trend, heat-up and cool-down dynamics, the simulated temperature is mostly about 1 °C lower. This could be related to the behavior seen in the housing plot, figure 4.6, which also exhibits a constant deviation from measured temperature.

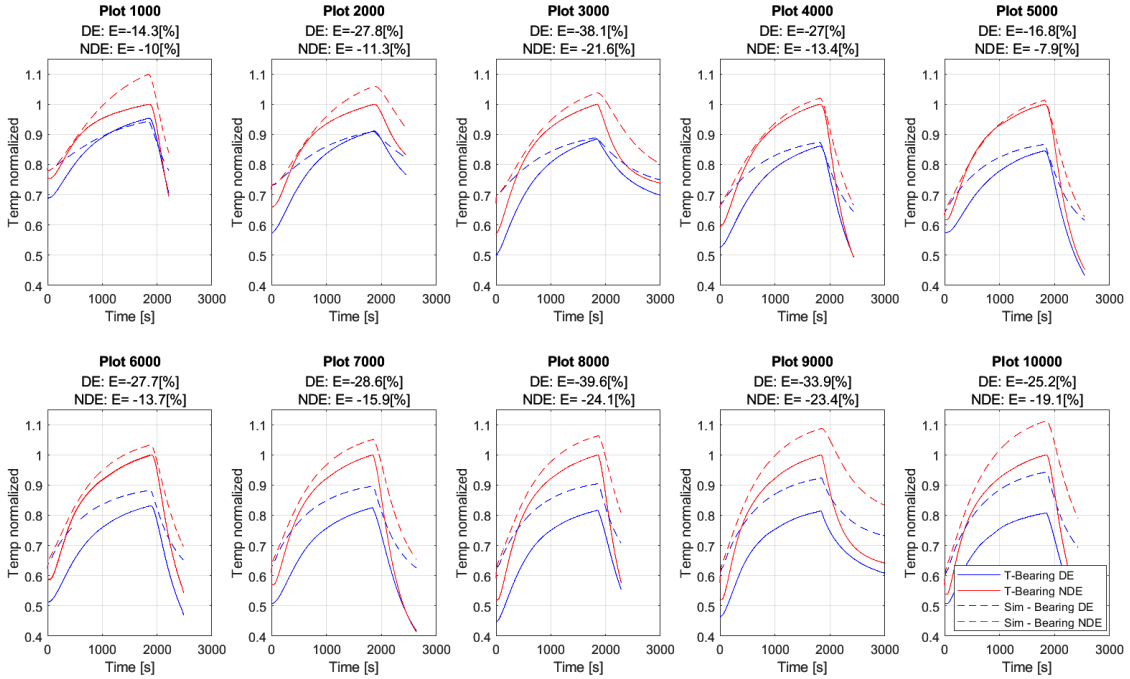

Figure 4.7: Steady-state verification - predicted temperature in the bearings.

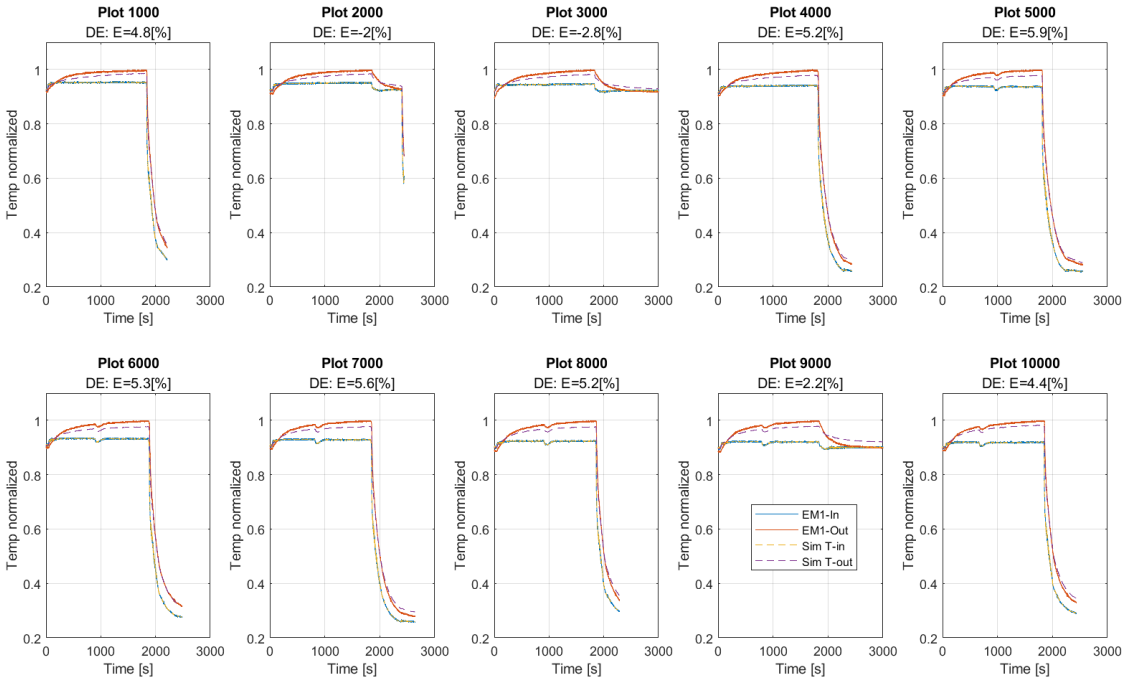

Figure 4.8: Steady-state verification - predicted temperature of coolant out of the motor.

The losses applied during the cycle are presented in figure 4.9, and figure 4.10 shows a summation of the total loss by category. It can be observed that the copper losses in the windings do not change particularly much in magnitude, since the torque in all cases is around 200 Nm (±10Nm). On the other hand, iron losses in the lamination as well as mechanical losses increase at higher speeds, and above 5000 RPM they together outweigh the copper losses.

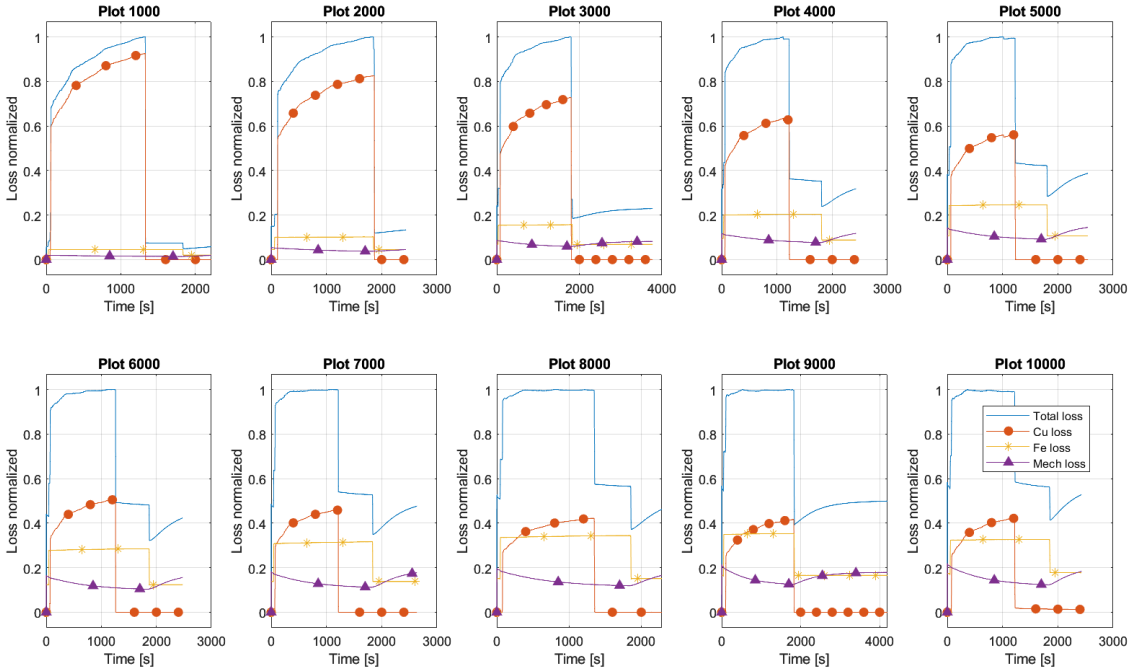

Figure 4.9: Steady-state verification - losses during the cycles.

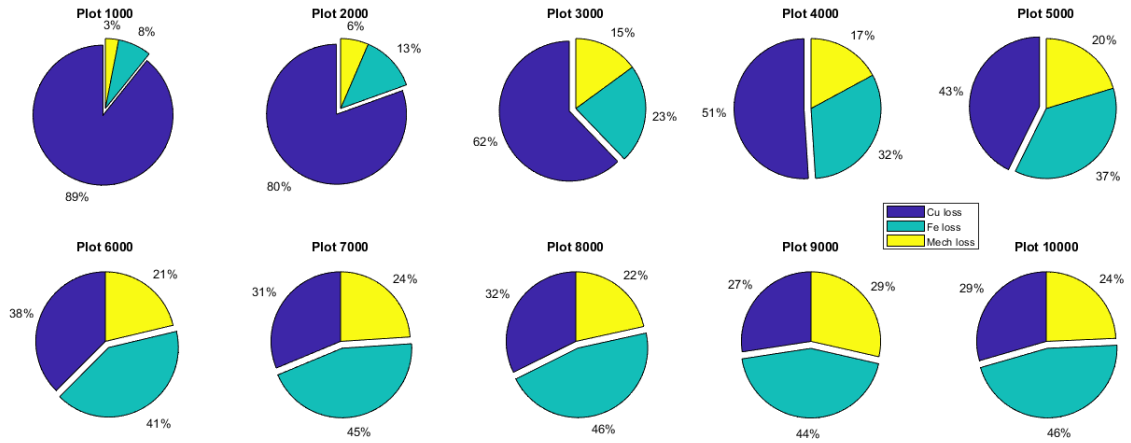

Figure 4.10: Steady-state verification - distribution of losses by category during the cycles.

Table 4.1: Steady-state validation results summarized. Maximum relative error over complete cycle duration.

Maximum relative error complete duration of cycle [%]							
	Component						
Speed RPM	Active windings	End windings	Rotor	Housing	Bearing DE	Bearing NDE	Coolant
1000	28.7	22.5	24.1	15.8	-14.3	-10.0	4.8
2000	27.9	21.5	23.4	18.0	-27.8	-11.3	-2
3000	27.3	20.8	22.4	19.3	-38.1	-21.6	-2.8
4000	26.3	20.1	21.7	19.7	-27.0	-13.4	5.2
5000	25.9	19.7	22.7	20.3	-16.8	-7.9	5.9
6000	23.7	17.6	20.3	19.9	-27.7	-13.7	5.3
7000	22.1	16.2	17.5	19.8	-28.6	-15.9	5.6
8000	20.7	15.3	15.6	19.4	-39.6	-24.1	5.2
9000	18.6	13.0	14.1	18.5	-33.9	-23.4	2.2
10000	14.9	10.1	13.7	17.8	-25.5	-19.3	4.4

Table 4.2: Steady-state validation results summarized. Maximum relative error at end of cycle.

Maximum relative error at end of cycle [%]							
	Component						
Speed RPM	Active windings	End windings	Rotor	Housing	Bearing DE	Bearing NDE	Coolant
1000	6.7	0.2	14.6	15.0	1.1	-9.9	1.2
2000	12.6	6.6	16.9	17.8	0.3	-5.9	1.3
3000	15.3	10.3	17.3	19.2	0.4	-3.7	1.5
4000	16.7	12.5	16.4	19.7	-1.5	-1.9	1.6
5000	17.3	13.6	16.0	20.3	-2.5	-1.2	2
6000	16.3	12.9	13.6	19.9	6.5	-3.3	2.3
7000	15.2	12.0	10.1	19.8	-8.8	-5.1	1.9
8000	13.5	10.6	6.5	19.4	-10.8	-6.4	1.9
9000	9.2	6.9	0.9	18.5	-13.5	-8.7	2.4
10000	1.7	1.6	-6.1	17.8	-16.8	-11.3	1.6

Tables 4.1 and 4.2 show that for some measured nodes, there is a big discrepancy in error over the complete cycle compared to the error at the end of the cycle. An explanation for this is that the simulation cannot exactly mimic the test conditions. This can for example be seen from the initial temperatures, as the test object does not seem to be uniformly warm at the beginning of the test. This can have a big effect on the relative error.

4.1.2 Verification - transient cycle

The transient performance of the model was verified by correlation with test data running the WLTC cycle, described in section 2.4.2. The test cycle is slightly more aggressive due to higher speed and acceleration, as shown in 4.11. To achieve the highest fidelity possible, the exact speed, torque and voltage vectors as used by the motor in the test was used as input to the simulation. The test was performed in a complete ERAD, and so the motor is mounted in connection to the transmission and inverter. These components will of course also heat up during operation, and influence each other because of the direct/close contact to each other.

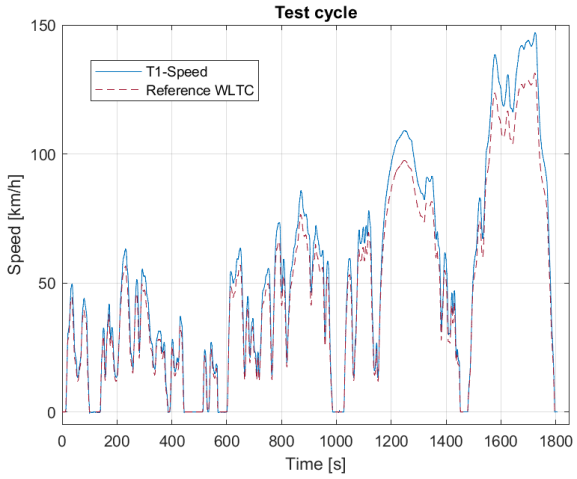

Figure 4.11: Transient test cycle, slightly more aggresive WLTC.

Table 4.3 below summarizes the simulation results compared to the test data in terms of maximum absolute temperature deviation (measured - simulated) and maximum relative error, as definded in eq. (4.1). The table comprises simulation results for end winding, stator yoke, housing, rotor yoke and bearings, where eventual numbers after the component refers to different points of measurement.

Table 4.3: Maximum deviation in absolute temperature and maximum relative error, as defined in eq. (4.1). All values rounded to one decimal. Numbered components refer to different points of measurement.

Measured vs Simulated temperature WLTC		
Component	Max deviation [°C]	Max relative error [%]
End windingDE	6.9	16.4
Stator3	-2.3	8.7
Stator12	-2.0	7.4
Housing3	-3.6	13.9
Housing12	-2.9	11.6
Rotor1	7.7	20.9
Rotor2	8.0	22.0
BearingDE	12.2	4.0
BearingNDE	-14.6	48.7

Figure 4.12 below plots the deviation in temperature, ΔT, over the complete cycle. The figure shows the same cases as reported in table 4.3 above, but all plots in the figure have been smoothed for easier readability and visualization of trends. It can be seen that the stator and housing temperature prediction ranges within ± 4°C from measured data. The end windings are within ± 7°C, the rotor is within ± 8°C and the bearings are within ± 15°C.

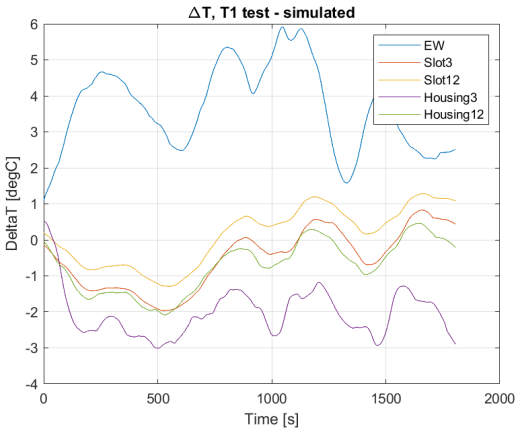

(a) Temperature deviation - end windings, stator lamination and housing.

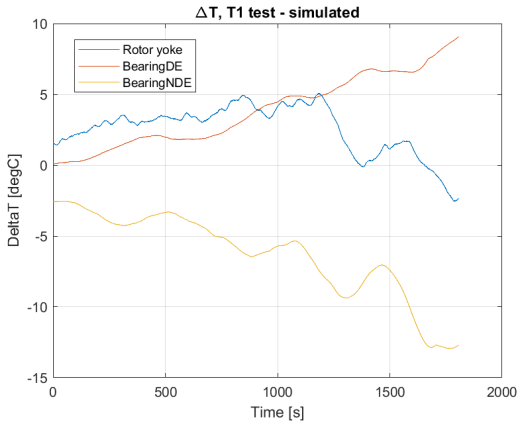

(b) Temperature deviation - rotor and bearings.

Figure 4.12: Smoothed plots of temperature deviation during the cycle.

In the following plots of simulated temperature versus measured, the solid plots labeled "T1" refers to test data and the dashed lines labeled "Sim" refers to simulation output. Figure 4.13a shows the temperature in the stator lamination, where "Slot3" and "Slot12" refer to different positions along the motor circumference. Figure 4.13b shows the rotor temperature.

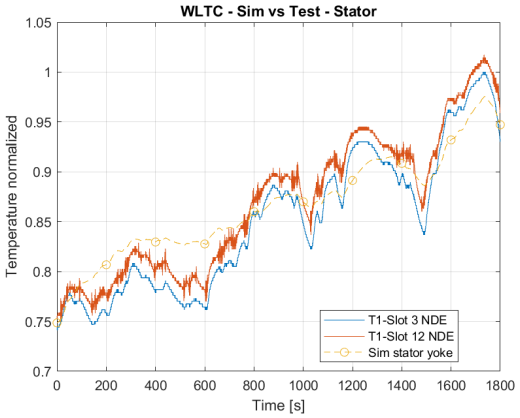

(a) WLTC verification - stator temperature.

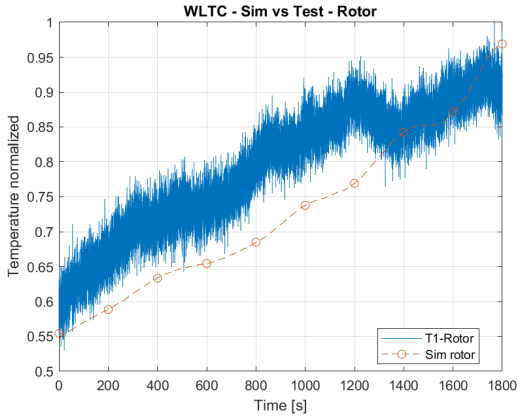

(b) WLTC verification - rotor temperature.

Figure 4.13: Simulation of stator and rotor temperature during WLTC compared to test data for verification.

Figure 4.14a shows the housing temperature, where “Housing3” and “Housing12” again refers to different sensor positions along the circumference of the motor. Both are included in the plot to show that the temperature in a component differ depending on where the measurement is taken. This can not be captured in the model, but is important to be aware of when comparing to test data. Figure 4.14b shows the temperature in the end windings, there “inDE” refers to the sensor inside the windings and on the drive-end side.

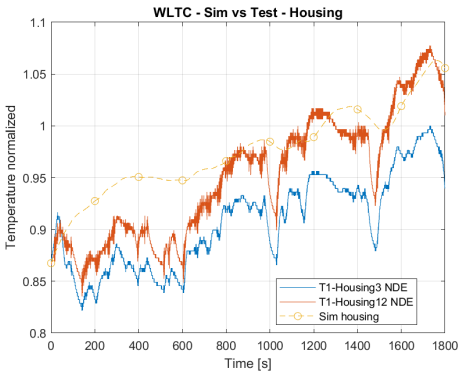

(a) WLTC verification - housing temperature.

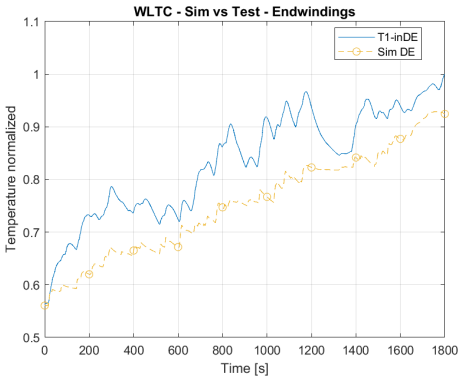

(b) WLTC verification - end winding temperature.

Figure 4.14: Simulation of housing and end winding temperature during WLTC compared to test data for verification.

Figure 4.15a shows the bearing temperature for each side. An unexpected behaviour is revealed in terms of difference between DE and NDE, where the drive-end side would be expected to be the warmer side. Figure 4.15b shows coolant temperature out of the motor, and a rather poor correlation to the test data. This is mainly because the initial temperature is inconsistent between simulation and test data. This fault is explored further in the next section, 4.1.2.1.

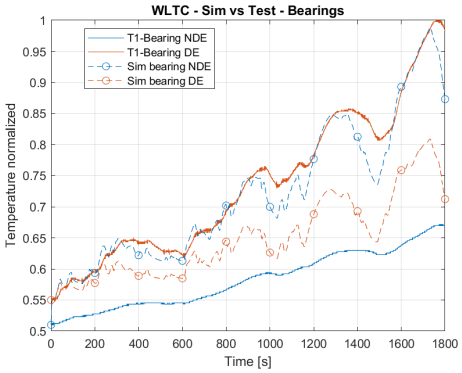

(a) WLTC verification - bearing temperature.

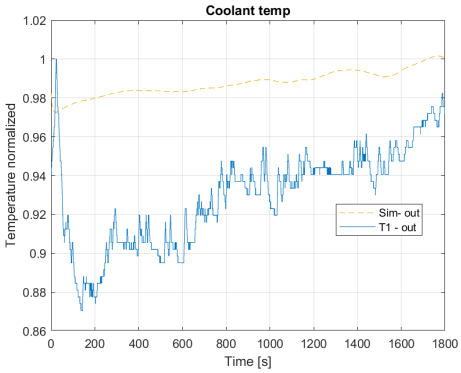

(b) WLTC verification - coolant temperature out of motor.

Figure 4.15: Simulation of bearing and coolant temperature during WLTC compared to test data for verification.

4.1.2.1 Possible sources of error & correlation corrections

While the simulation results over the complete WLTC cycle correlates well to the test data in terms of trend and absolute temperature, there are sections of the cycle were the simulation does not follow the same gradient as the test data. In this test case, a complete ERAD unit is tested, and as previously discussed, the motor temperature gradient is affected by the nearby components. In this particular case, the motor coolant comes from the inverter, and while the inlet temperature to the ERAD is kept constant at 25°C, it will heat up before reaching the motor. Figure 4.16 below shows the coolant temperature in and out of the inverter, and out of the motor.

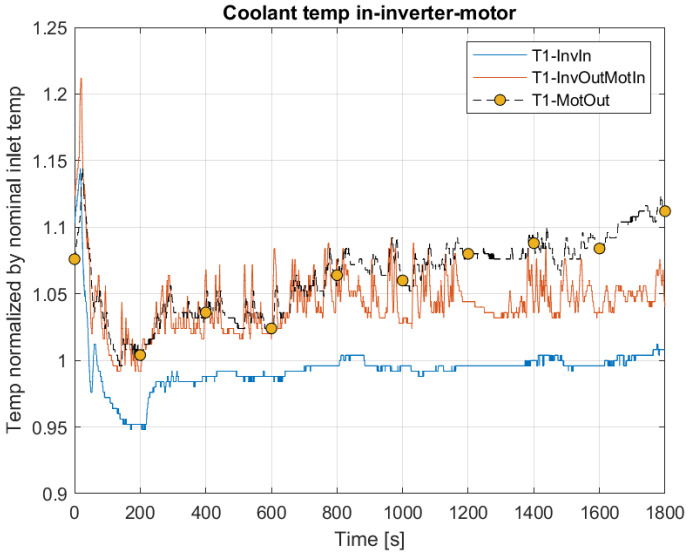

Figure 4.16: Coolant temperature from test data - temperature into inverter, out of inverter/into motor and out of the motor. Normalized to nominal inlet temperature.

To further mimic the test conditions as closely as possible, the coolant temperature into the motor from the test data (red plot in figure 4.16 above) is used as input. The results from re-running the simulations with this new boundary condition is shown in figures 4.17 to 4.20 and summarized in table 4.4.

Figure 4.17 below plots the temperature deviation, ΔT, over the complete cycle. All plots in the figure have been smoothed for easier readability and visualization of trends. It can be seen that the stator and housing temperature prediction ranges within $\pm$ 3.3°C from measured data. The end windings are within $\pm$ 4.2°C, the rotor is within $\pm$ 9.5°C and the bearings are within $\pm$ 6.5°C.

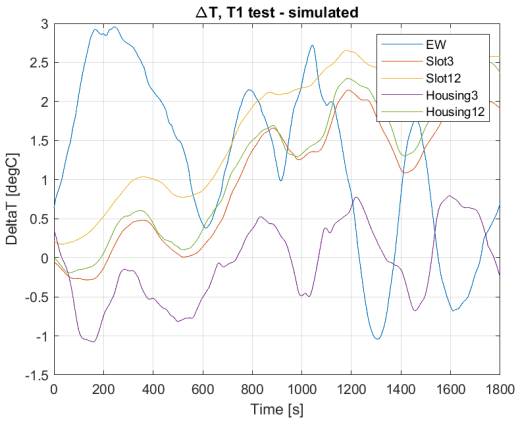

(a) Temperature deviation - end winding, stator lamination and housing.

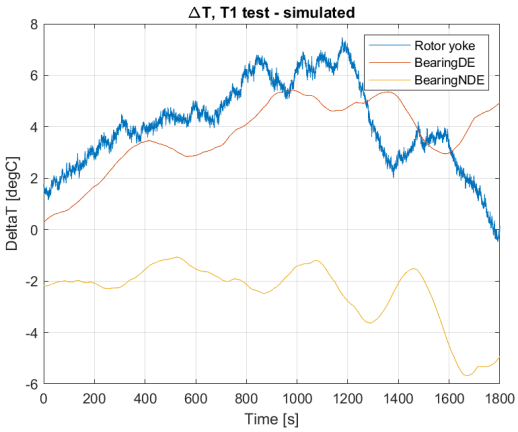

(b) Temperature deviation - rotor and bearings.

Figure 4.17: Smoothed plots of temperature deviation during the cycle.

Figure 4.18a shows the stator temperature with the new coolant boundary condition. Comparing to the previous simulation in figure 4.13a, the simulated temperature is somewhat lower, but still correlates well and improves the error with respect to the measurement in position "Slot3". Figure 4.18b shows the rotor temperature, and compared to the previous simulation in figure 4.13b it shows a slightly worse correlation, deviating about 2 degrees more.

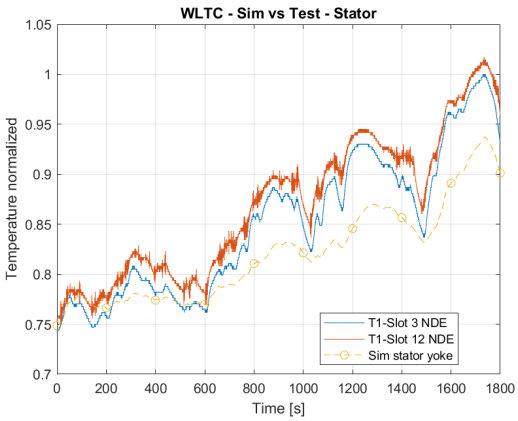

(a) WLTC verification, correlated - stator temperature.

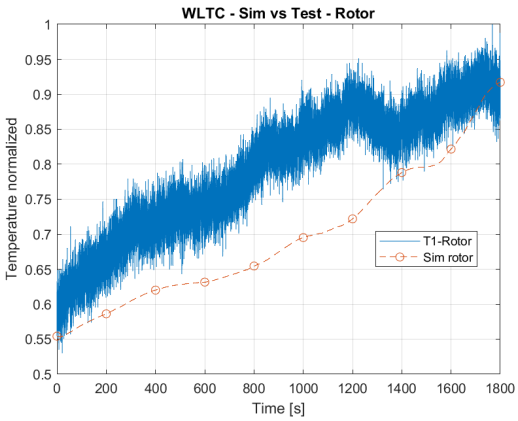

(b) WLTC verification, correlated - rotor temperature.

Figure 4.18: Simulation of stator and rotor temperature during WLTC, with boundary conditions from test data.

Figure 4.19a shows the housing temperature with the new coolant boundary condition, and can be compared to the previous simulation in figure 4.14a. The temperature is again somewhat lower than the previous case, but the error is decreased and maximum deviation lowered. Figure 4.19b shows the new simulation of the end winding temperature, as compared to the previous in figure 4.14b. In this case, the temperature is higher, the error is improved by about 5 percentage points and the maximum deviation is lowered by more than 4 °C.

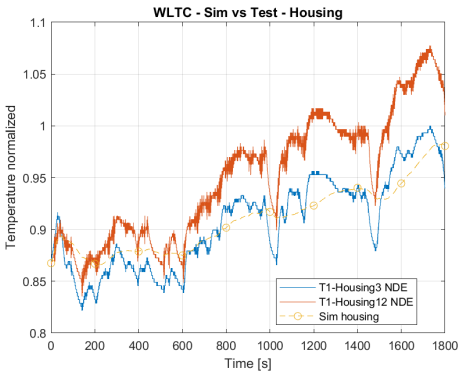

(a) WLTC verification, correlated - housing temperature.

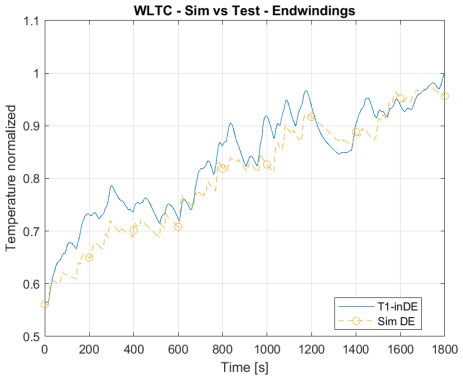

(b) WLTC verification, correlated - end winding temperature.

Figure 4.19: Simulation of housing and end winding temperature during WLTC, with boundary conditions from test data.

Figure 4.20a shows the bearing temperature from the new simulation as compared to figure 4.15a. The drive-end and non drive-end side temperatures now correlate better and as expected. The error for the NDE bearing is decreased by 27 percentage points. Finally, figure 4.20b shows the coolant temperature with the new boundary condition, in contrast to figure 4.15b. As expected, the correlation is much closer to the measured test data. However after about 800 seconds into the cycle a deviation is clearly visible.

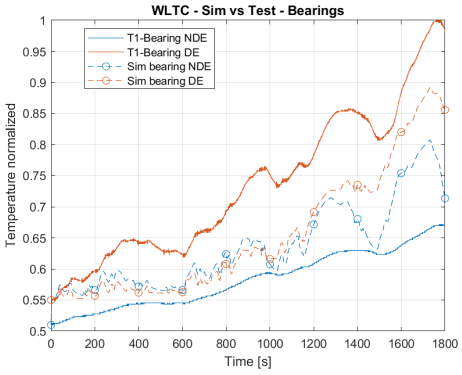

(a) WLTC verification, correlated - bearing temperature.

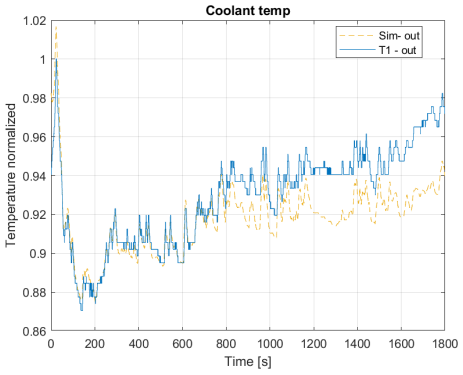

(b) WLTC verification, correlated -coolant temperature out.

Figure 4.20: Simulation of bearing and coolant temperature during WLTC, with boundary conditions from test data.

Table 4.4: Simulation results after model improvements, corresponding to table 4.3. Fourth column shows the improvement in maximum relative error between the initial model and the correlated, in percentage points.

Measured vs Simulated temperature WLTC			
Component	Max deviation [°C]	Max relative error [%]	Error improvement [p.p]
EndwindingDE	4.2	11.3	5.1
Stator3	2.7	8.6	0.1
Stator12	3.3	10.3	-2.9
Housing3	-1.5	6.2	7.7
Housing12	3.1	10.0	1.6
Rotor1	9.5	25.5	-4.6
Rotor2	9.4	25.6	-3.6
BearingDE	6.5	4.0	0.0
BearingNDE	-6.5	21.7	27.0

4.1.3 Sensitivity analysis

To identify the most important parameters influencing the thermal behavior of the model, a sensitivity analysis was performed focusing on a selected number of components. The chosen components are the active windings, end windings and rotor, which were identified as the most critical for accurate prediction. The study was performed by simulating the cycle shown in figure 4.21a, with the related losses shown in figure 4.21b. The variation in predicted temperature is reported in [%] calculated according to eq. (4.2), such that an increased temperature compared to the original model is positive. The temperature is measured at the time t = 1850s, when the model has reached steady state.

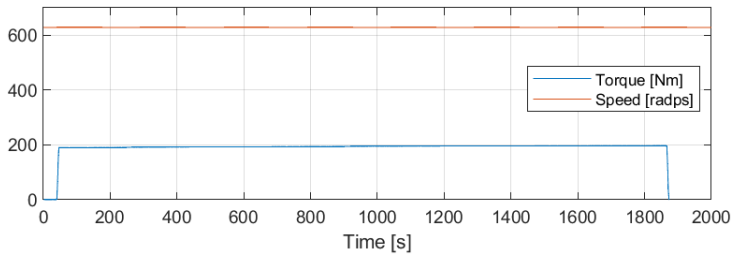

(a) Cycle running constant speed and torque.

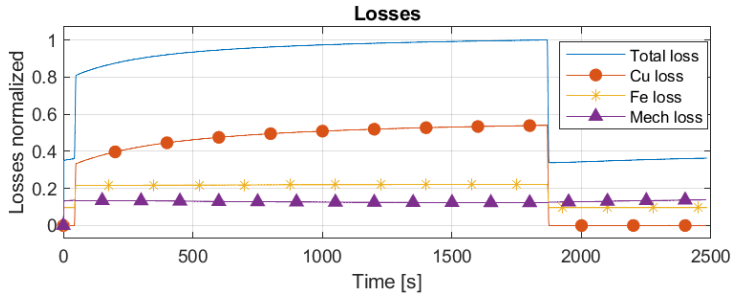

(b) Losses by category for the cycle shown above.

Figure 4.21: Sensitivity analysis was performed with the cycle shown in (a) resulting in the losses shown in (b).

$$\text{Variation } [\%] \ = \frac{T_{\text{modified}} - T_{\text{original}}}{T_{\text{modified}}} \tag{4.2}$$

With regards to the active winding temperature prediction, there are a number of parameters that influence the node. Thermal conductivity and thermal resistance to the stator yoke are chosen as parameters in this study. The conductivity is interesting since it is a calculated equivalent depending on factors such as insulation and fill factor (see section 3.2), and the resistance to the stator greatly influences how much heat can be transported from the windings to the coolant flowing through the housing.

Results from the active winding sensitivity analysis are shown in table 4.5 below. The radial component of thermal conductivity has the biggest influence, showing a -7.99% decrease and a 9.62% increase in temperature when the parameter is varied

between +25% and -25%, respectively. Second most influencing factor is the thermal resistance to the stator, showing a 6.90% increase and a -10.25% decrease in temperature when the parameter is varied between +25% and -25%. The results are consistent with conclusions in literature [66] [58].

Table 4.5: Active windings parameter variation and subsequent result on temperature rise compared to baseline.

Sensitivity analysis - windings		
Parameter	Modification [%]	Variation [%]
Thermal conductivity rad	+25 [%]	-7.99
Thermal conductivity rad	-25 [%]	9.62
Thermal conductivity ax	+25 [%]	0.11
Thermal conductivity ax	-25 [%]	-0.18
Resistance to yoke	+25 [%]	6.90
Resistance to yoke	-25 [%]	-10.25

For the end windings, the chosen parameters are thermal conductivity, with the same motivation as previously for the active windings, and additionally the convective resistance to air. The results of this are shown in table 4.6 for the drive-end side, and in table 4.7 for the non drive-end side. The results are similar for both sides, and it is evident that the thermal resistance to air is a critical parameter, as a reduction greatly increases the predicted temperature while an increased resistance has a moderate effect.

Table 4.6: Drive-end end windings parameter variation and subsequent result on temperature rise compared to baseline.

Sensitivity analysis - end winding DE		
Parameter	Modification [%]	Variation [%]
Thermal conductivity rad	+25 [%]	-9.27
Thermal conductivity rad	-25 [%]	-5.23
Thermal conductivity ax	+25 [%]	-7.58
Thermal conductivity ax	-25 [%]	-7.11
Resistance to air	+25 [%]	-2.38
Resistance to air	-25 [%]	-14.06

Table 4.7: Non drive-side end windings parameter variation and subsequent result on temperature rise compared to baseline.

Sensitivity analysis - end winding NDE		
Parameter	Modification [%]	Variation [%]
Thermal conductivity rad	+25 [%]	-9.95
Thermal conductivity rad	-25 [%]	-4.84
Thermal conductivity ax	+25 [%]	-7.94
Thermal conductivity ax	-25 [%]	-6.99
Resistance to air	+25 [%]	-3.24
Resistance to air	-25 [%]	-13.07

Finally for the rotor, the chosen parameters are thermal conductivity from the laminated core and the thermal resistance to the air gap. The results are shown in table 4.8. It is concluded that the radial thermal conductivity and the thermal air gap resistance are the most sensitive parameters, seeing as a +25% higher value decreases the predicted temperature by -4.35% and -3.69% respectively, while a decreased value does not have as big effect.

Table 4.8: Rotor parameter variation and subsequent result on temperature rise compared to baseline.

Sensitivity analysis - rotor		
Parameter	Modification [%]	Variation [%]
Thermal conductivity rad	+25 [%]	-4.35
Thermal conductivity rad	-25 [%]	2.21
Thermal conductivity ax	+25 [%]	-1.60
Thermal conductivity ax	-25 [%]	-1.61
Airgap resistance	+25 [%]	-3.69
Airgap resistance	-25 [%]	0.71

Sensitivity analysis is a valuable tool to identify the most influential thermal parameters and assess the robustness of the model. From this study, it can be concluded that there are certainly some parameters that have a big influence on the predicted temperature and must be carefully chosen. In particular, these are the equivalent thermal conductivity of the windings, thermal conductivity of the laminated core and the convective resistance to air. To reduce the uncertainty of these parameters, numerical or experimental approaches could be used as described by [61] [60]. Finally, the uncertainty of the convective thermal resistance to air could be reduced by using CFD analysis to better understand the airflow inside the motor.

4.1.4 System response

The following section shows the results of the EM thermal model during some cycles that are common in vehicle operation and electric machine thermal evaluation. These are “constant speed” in section 4.1.4.1 and “repeated acceleration” in section 4.1.4.2.

4.1.4.1 Constant speed

Driving at constant speed for some time is a very common use case for a vehicle, for example in highway driving. This case simulates a constant vehicle speed of 125 [km/h] during 30 minutes, as shown in figure 4.22a below. The losses in the electric machine during this cycle is displayed in figure 4.22b.

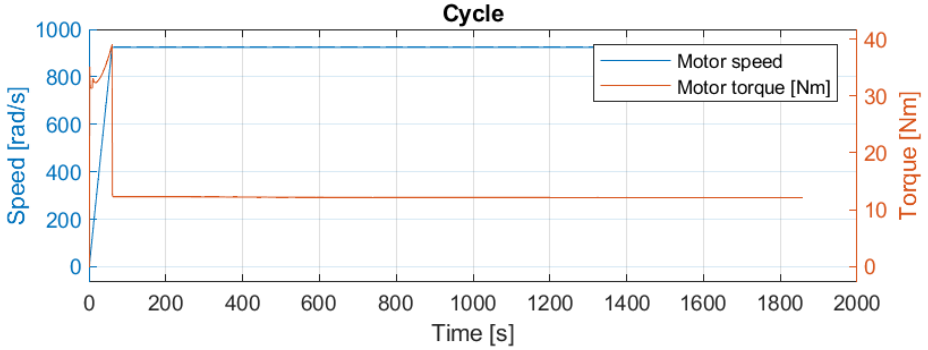

(a) Motor operating points during vehicle constant speed.

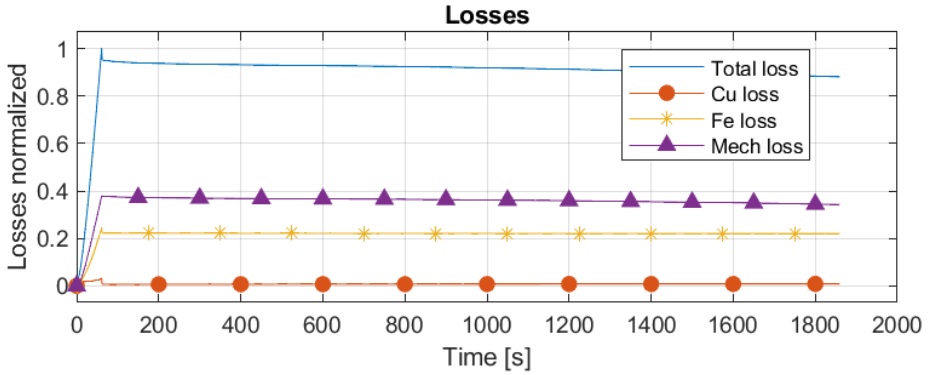

(b) Losses in the EM during the cycle.

Figure 4.22: Constant speed driving cycle, 125 [km/h] during 30 min.

The predicted temperatures in stator, rotor, active- and end windings are shown in figure 4.23. These particular nodes are selected because they are considered the most critical in terms of thermal development. As expected from a high-speed cycle, the iron losses and mechanical losses outweigh the copper losses, and hence the stator temperature is high. The copper losses are comparatively low, but will heat up nevertheless from the close contact and low thermal conductivity to the windings. The relatively high mechanical losses also contributes to heat up the rotor.

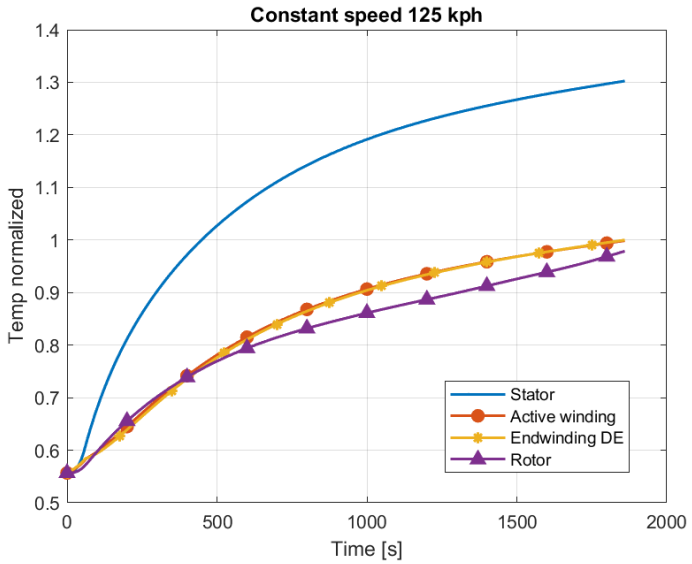

Figure 4.23: Selected temperature measurements from the constant speed cycle.

4.1.4.2 Repeated accelerations

A cycle of 10 repeated accelerations from 10-120 km/h during 100 seconds was simulated according to figure 4.24a, with subsequent losses shown in figure 4.24b. The predicted temperature of stator, rotor and windings is shown in figure 4.25.

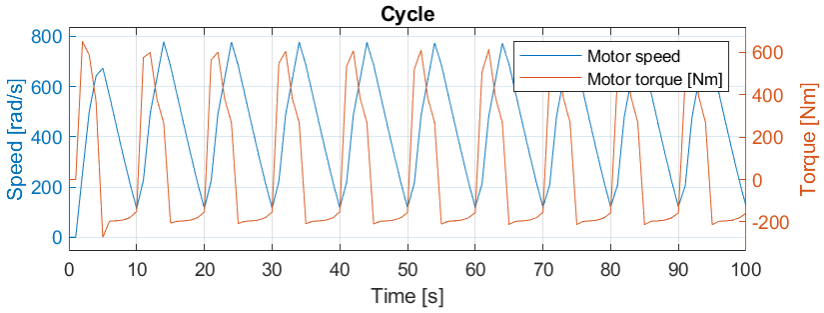

(a) Cycle for 10 repeated accelerations from 10-120 km/h in 100 seconds. Plot shows motor speed and torque during accelerations.

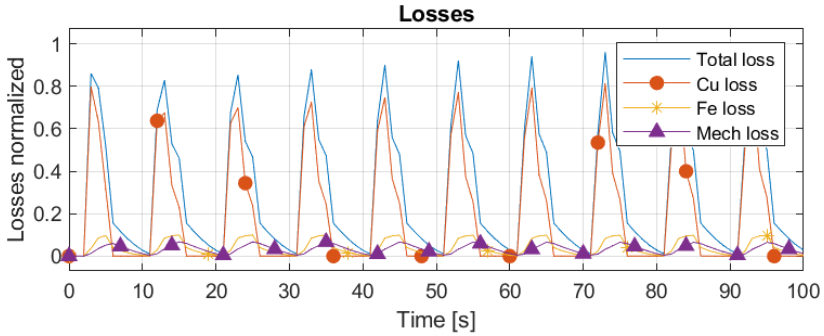

(b) Losses during cycle.

Figure 4.24: Repeated acceleration cycle described by speed, torque and the resulting losses.

The results are expected. Since the iron losses are speed dependent, and the cycle never operates at a sustained high speed, the iron losses are low and hence also the stator and rotor temperatures. The copper losses however are torque dependent, and since the accelerations require a high amount of torque the losses in the windings are subsequently very high. The stator temperature heats up because of the close interaction and hence low thermal resistance to the windings. The low sustained speed along with low mechanical losses means the rotor barely heats up.

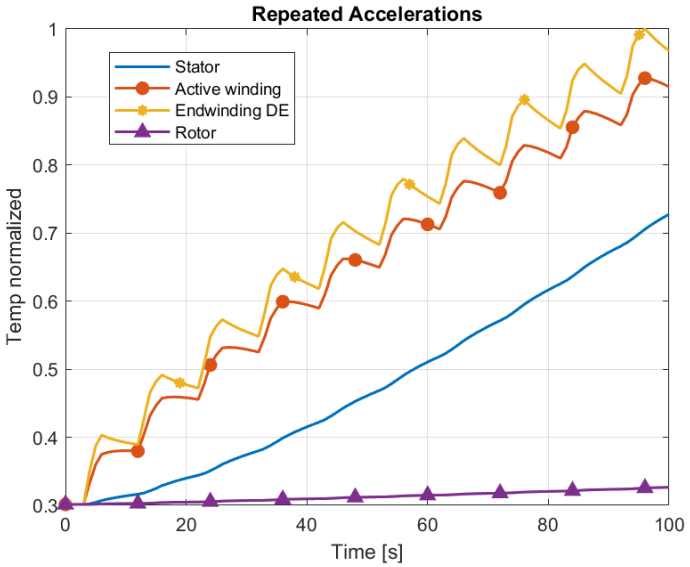

Figure 4.25: Selected temperature measurements resulting from the demanding repeated acceleration cycle.

4.1.5 Loss-mode

The loss-mode strategy is controlled by altering the output from the loss-lookup tables before being applied in the model, as shown in figure 4.26a below. A binary control signal activates loss-mode, whereas the loss can be set to a chosen constant value or a gain to the loss maps. This approach was chosen since no mapped data for loss-mode operation were available, and input values reasonable for loss-mode were instead taken from the available literature. The signal to activate loss-mode is a simple time-based controller shown in figure 4.26b.

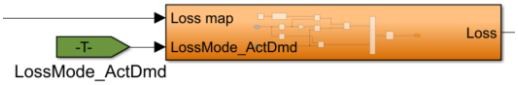

(a) Control block to alter the calculated losses for loss-mode operation.

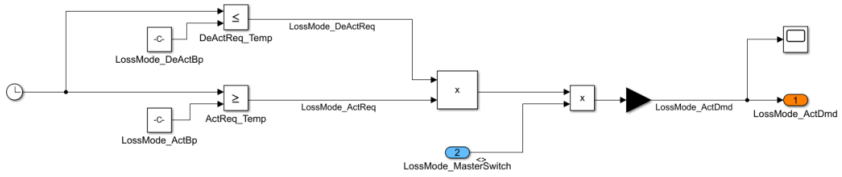

(b) Loss-mode activation signal control.

Figure 4.26: Basic loss-mode controller implementation.

4.1.5.1 ERAD loss-mode

To add the possibility of simulating with a loss-mode in the inverter, heat is added to the coolant before entering the electric machine model. The model for this is shown in figure 4.27a, and figure 4.27b shows the implication on the coolant temperature reaching the motor.

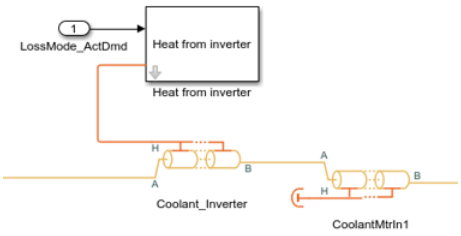

(a) Coolant is heated by the inverter.

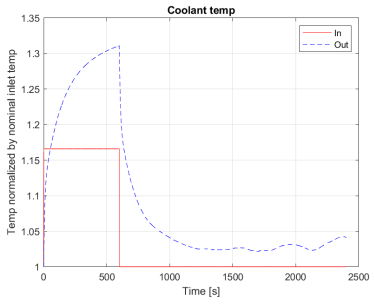

(b) Coolant in- and out of the electric motor when running WLTC with 10min loss-mode preconditioning.

Figure 4.27: Loss-mode in the inverter is modeled by heating up the coolant before it reaches the electric machine.

To test the loss-mode functionality using a complete ERAD, heating of the transmission was studied. The motivation for this is shown in figure 4.28a, the energy lost in the transmission is lower with higher operating temperature. "Cold" is here 0°C, corresponding to a loss of 4.1% of the total energy consumed during a WLTC cycle. "STP" is 25°C, and "warm" is 65°C, corresponding to 3.8% and 3.5% respectively. In order to model the transient heat developed in the transmission, a basic thermal model was created. The model consists of a single lumped mass and heat flow from internal losses, conduction to the electric machine and convection to ambient. Figure 4.28b below shows this model compared to measured data of oil temperature in an ERAD transmission.

There are surprisingly few papers documenting thermal models of an electric machine in combination with a transmission model. However, it is proposed in [26] that a lumped-parameter motor model can be coupled to a transmission model by conduction through the housing, end caps and shaft. This approach is adopted for the developed transmission model, however it should be noted that the authors could not verify this model due to lack of adequate data.

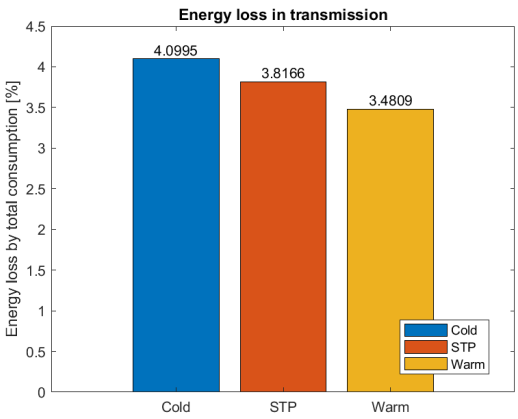

(a) Transmission losses at various temperatures.

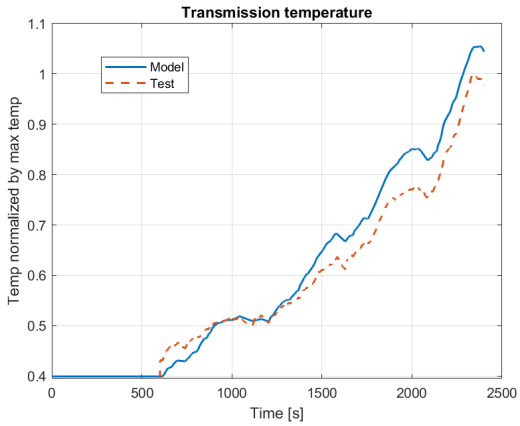

(b) Basic transmission model compared to measured oil temperature.

Figure 4.28: Raising the temperature of the transmission greatly reduces its losses. ERAD loss-mode could possibly be used to help heat up the transmission and reduce its losses.

A test case was set up to run the WLTC cycle but with a 10 minutes standstill phase for preconditioning, using loss-mode. The cycle is displayed in figure 4.29a, and the concurrent losses in figure 4.29b. During the preconditioning phase, 2000W of heat power was considered from the inverter, and 2500W to be generated in the stator (divided 2000W in the yoke and 500W in the teeth). The numbers were taken from what was found reasonable for a loss-mode while standstill according to [15], however the distribution in the stator is a coarse approximation in lack of sources. The red-dashed plot in figure 4.29a shows a binary command setting the loss-mode control on or off, hence on during the first 600 seconds.

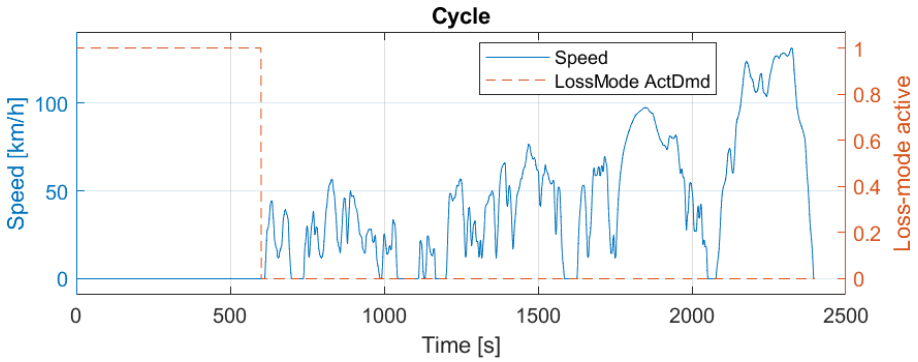

(a) WLTC with 10min standstill before take-off for preconditioning.

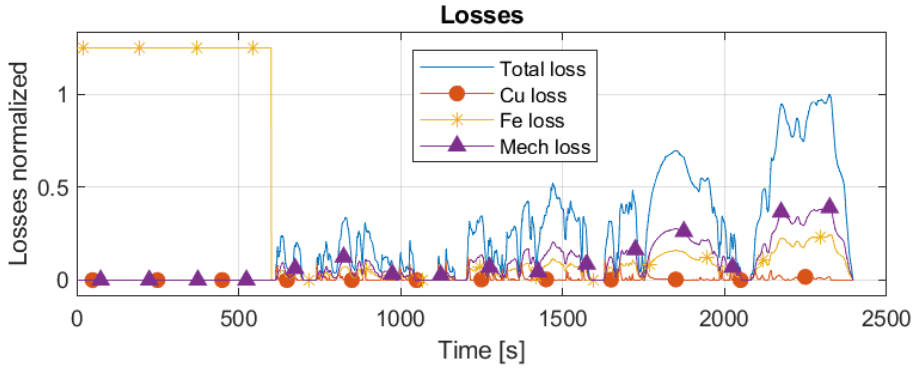

(b) Losses during preconditioning and rest of WLTC cycle.

Figure 4.29: Cycle with preconditioning period, described by speed, loss-mode controller and losses during cycle.

Figure 4.30 below shows the predicted temperatures in the electric machine during this cycle. Stator and active winding in figure 4.30a, end windings and magnet in figure 4.30b and all other measured components in figure 4.30c. The results show that with these selected amount of losses during a 10min standstill preconditioning phase, no temperature reaches beyond what would be considered a safe temperature range.

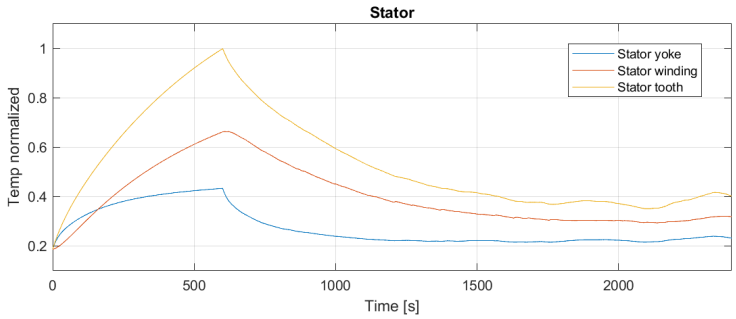

(a) Stator and active winding temperature.

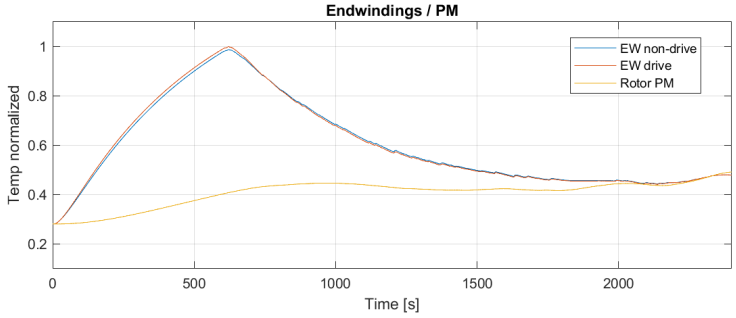

(b) End winding and PM temperature.

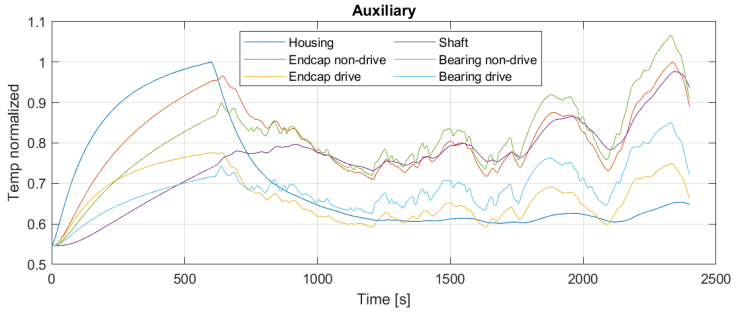

(c) Housing, endcap, shaft & bearing temperature.

Figure 4.30: Temperatures in the machine during WLTC cycle with 10min loss-mode preconditioning. All temperatures are within what would be considered safe.

The resulting influence on the transmission energy loss is shown in figure 4.31a, together with temperature of the transmission and connected parts of the motor in figure 4.31b. The model shows some, but very little heat transfer to the transmission during the 600 seconds of standstill preconditioning. The little heat that is transferred has a minor effect on the energy loss, such that no clear conclusion to the effectiveness can be made. As previously stated, the thermal resistance between the motor and transmission could not be verified, and so the idea should not be dismissed from this study. Furthermore, a concept that utilizes shared cooling fluid between the electric machine and the transmission would further increase the effective heat transfer.

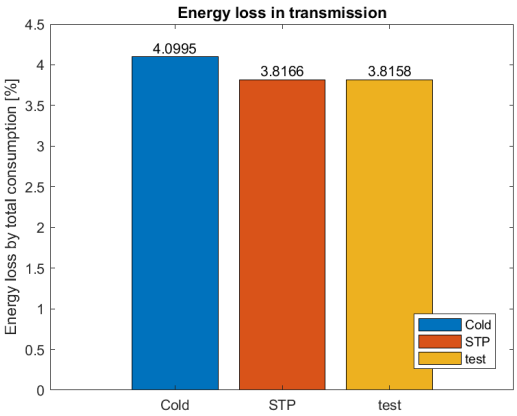

(a) Transmission losses for the pre-conditioned case (third, yellow bar).

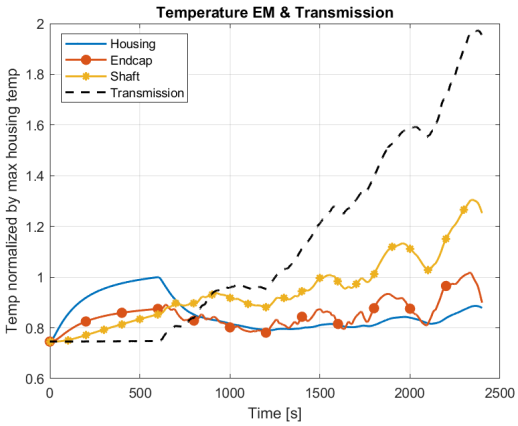

(b) Temperature of transmission and selected motor parts.

Figure 4.31: Results of ERAD loss-mode study to increase transmission efficiency. A surprisingly small amount of heat transfers from the motor to the gearbox, however some improvement can be seen.

4.1.6 Conclusion EM thermal model verification

The verification activities showed that the model performs within its expected accuracy of 30% relative error. From the steady-state correlation, it was clear that the model accuracy is higher at higher speeds. A factor for this could be discrepancy between the loss map data used in the model versus the actual losses during testing. It was discovered during the later stages of the thesis that the simulated loss maps indeed deviated from what was found in testing, and especially at lower speeds. The loss maps are also independent of motor temperature, and have been compiled at a set temperature. Optimally, loss maps with temperature as a fourth dimension would be used, however they were not available.

Still, the results were found to be within range and especially close upon reaching steady-state. The transient verification showed that the model correlates well also over the duration of a complete driving cycle, WLTC in this case.

It should be noted that magnet temperature prediction could not be validated, since it was not measured specifically in the available test data.

4.2 Vehicle thermal model

The vehicle thermal management model described in section 3.3.2 resulted in that the PTC heater is heating up the cabin together with the heat losses from the electric motor. The temperature setpoint is in this thesis chosen to 20°C, while the ambient temperature is -10°C. The ambient temperature is chosen to be low as the aim of this thesis is to investigate the utilization of powertrain losses in cold climate. The setpoint temperature was chosen as it is a common temperature of comfort in a cabin. For all the simulations, the motor configuration used is a PMSM. For the initial simulation, giving the results in this section, section 4.2, the variant of the NEDC cycle, described in section 3.4.1 was run for 4200 seconds. This means that, out of the 10 last 600 seconds of the NEDC cycle, seven of these were run, as the simulation time is long and all the 10 cycles were not needed to be run for the baseline simulations.

The PTC heater operates at maximum power until the measured cabin temperature is a couple of degrees over the setpoint. Then the heater command signal fluctuates between 0 and 1 as the heater turns on when the temperature drops a few degrees below the setpoint, and turns off when the temperature reaches a few degrees above the setpoint. The temperature of the air inside the cabin therefore fluctuates between a couple of degrees below the setpoint and a couple of degrees above it. This results in a cabin temperature with a behaviour shown in figure 4.32a. The figure also shows the temperature of the air that has been heated inside the PTC heater and goes into the cabin. When the air into the cabin is heated by the PTC heater, the power consumption is according to figure 4.32b.

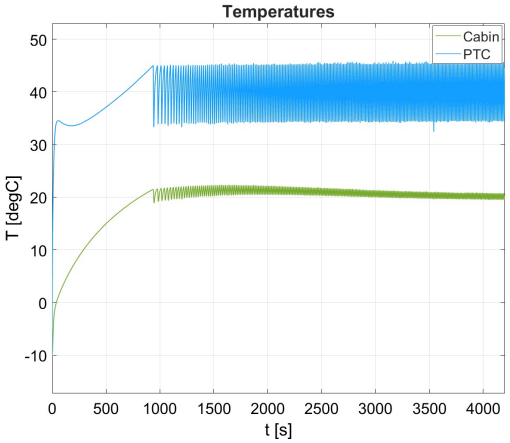

(a) Cabin and PTC heater temperatures.

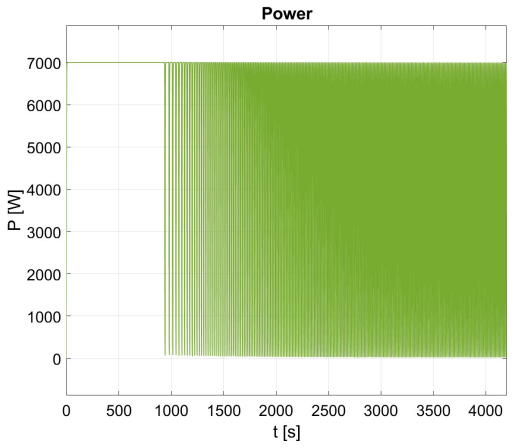

(b) PTC heater power consumption.

Figure 4.32: Cabin and PTC heater temperatures, and PTC heater power consumption during simulation.

The temperature reaches its setpoint of 20°C and then starts to fluctuate a little bit over it, then slightly overshoots until it stabilizes around 20°C again. The overshoot leads to a cabin temperature slightly higher than the setpoint, which leads to less

comfort for the people in the car as well as a little bit of energy that is wasted by the PTC heater. This is unwanted and something that could be improved in the cabin air control showed in figure 3.27.

As mentioned, the power consumption of the PTC heater fluctuates between 0 W and 7000 W when the cabin has reached its setpoint temperature. This gives the following energy consumption from the PTC heater, shown in figure 4.33.

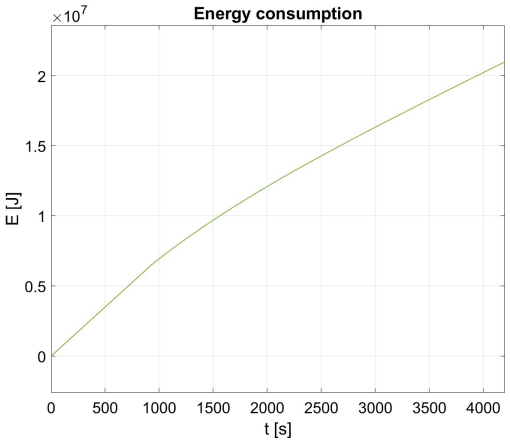

(a) PTC energy consumption.

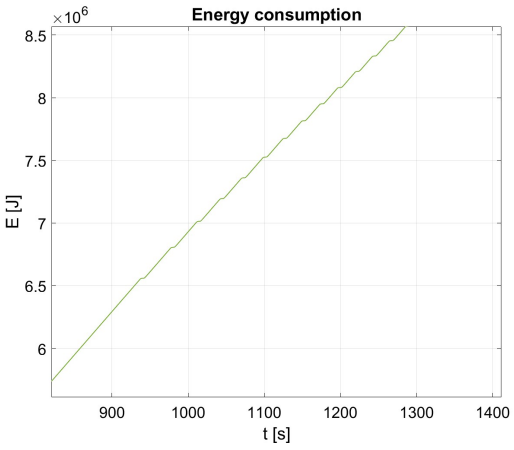

(b) Zoomed in view of PTC energy consumption.

Figure 4.33: PTC heater's energy consumption during simulation and zoomed in view when reaching cabin setpoint temperature.

When looking at the zoomed in view in figure 4.33b, it can be seen that the graph starts stepping just before 1000s, when the setpoint temperature of the cabin is reached, due to the fluctuating power of the PTC heater. This makes the energy consumption subside as less power is being taken from the heater as it is turned off when the temperature goes over the setpoint to let the cabin cool down.

When the motor is running without motor heat losses being utilized or preheating, the whole EPS system heats up according to figure 4.34.

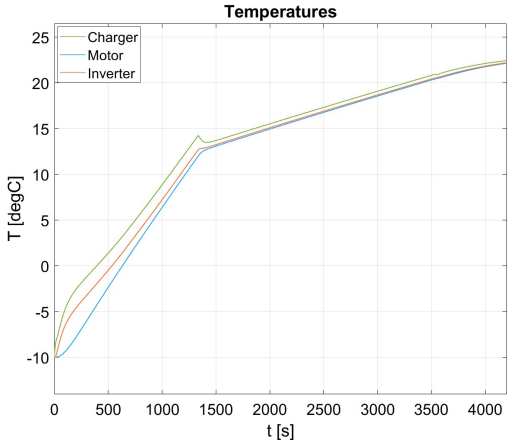

Figure 4.34: EPS components temperature during simulation.

The temperatures go a bit over 20°C, but keeps increasing and as the slope is still inclining in the end of the simulation, it will most likely keep inclining until it is started to be cooled down.

4.3 Powertrain heat utilization

The vehicle thermal model described in section 3.3.2, was used to simulate cases with different types of driving cycles and configurations of powertrain heat utilization and preheating of the motor. The driving cycles used were the WLTC described in section 2.4.2 as well as a variant of the NEDC described in section 2.4.1.

4.3.1 Simulations with WLTC

The WLTC was simulated both without any loss utilization or preheating of the motor, without preheating but with losses utilized for cabin heating, as well as with both preheating and heat loss utilization. The reason for preheating the motor before starting to run it is to investigate if it is possible to further decrease the energy consumption of the PTC heater. Preheating the motor have many benefits outside of reducing the PTC heater's energy consumption, which are described in section 2.3.3. Therefore, investigating if preheating is beneficial in this matter could help the decision making whether to preheat the motor or not, for the overall advantages. The results of the simulations are presented in the following sections.

4.3.1.1 Without preheating and without utilizing heat losses

When the simulation was run without preheating the motor and the heat losses from it were not utilized, it resulted in the following cabin heating, power and energy consumption from the PTC heater as well as temperature of the EPS components, shown in figure 4.35.

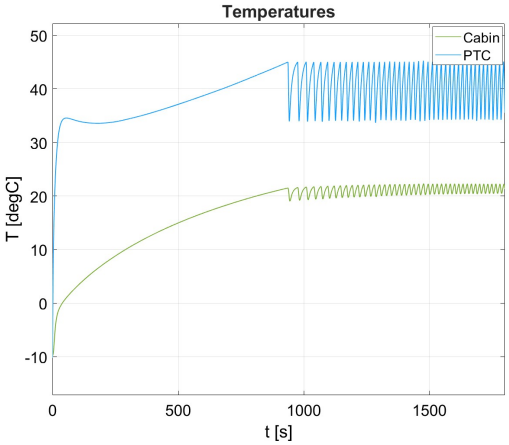

(a) Cabin temperature for WLTC without motor preheating or losses.

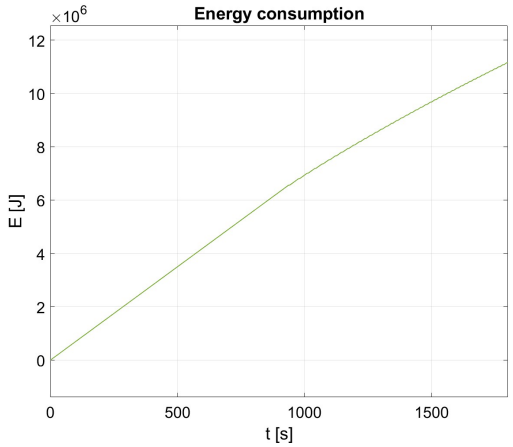

(b) PTC energy consumption for WLTC without motor preheating or losses.

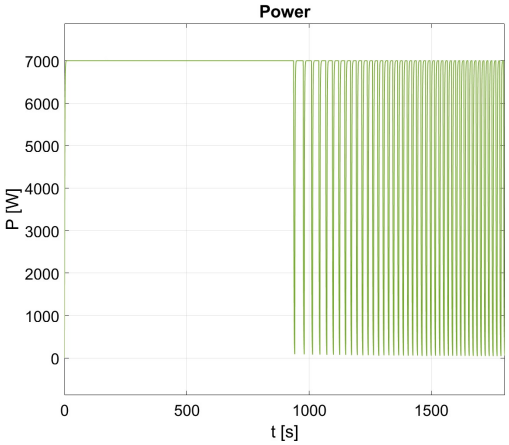

(c) PTC power consumption for WLTC without motor preheating or losses.

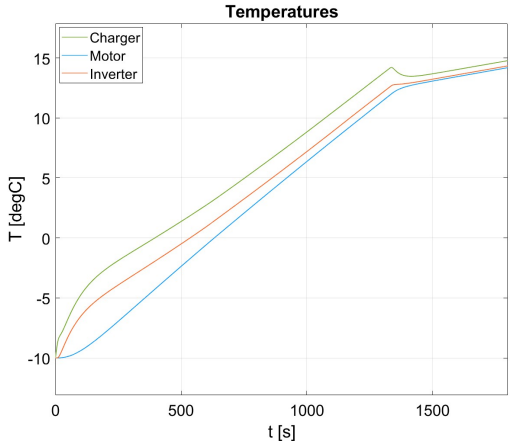

(d) EPS components temperatures for WLTC without motor preheating or losses.

Figure 4.35: Simulation results of WLTC run without preheating and without utilizing motor heat losses.

The figures show that the cabin heats up just above the setpoint temperature 20°C just after 900 seconds and then fluctuates around it, as described in the beginning of section 4.2. It is also possible to see that the temperatures in the EPS components, the charger, motor and inverter, reach temperatures of around 15°C, which is not much for electric propulsion components. The reason for this is simply that the simulation only was run for 1800 seconds, which did not give the EPS components enough time to heat up more. It is possible to see a positive slope of the graph in the end of the simulation, which means that if the simulation would run further, the temperature would keep increasing.

4.3.1.2 Without preheating and with utilizing heat losses

When the simulation was run still without preheating the motor, but now with utilizing the heat losses generated by it, it resulted in the following cabin heating, power and energy consumption from the PTC heater as well as temperatures of the EPS components presented in figure 4.36.

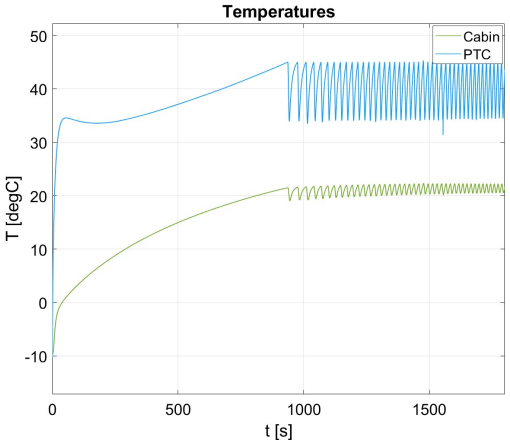

(a) Cabin temperature for WLTC without motor preheating, but with losses

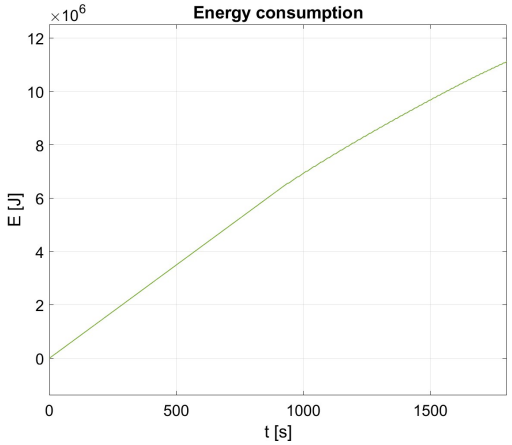

(b) PTC energy consumption for WLTC without motor preheating, but with losses.

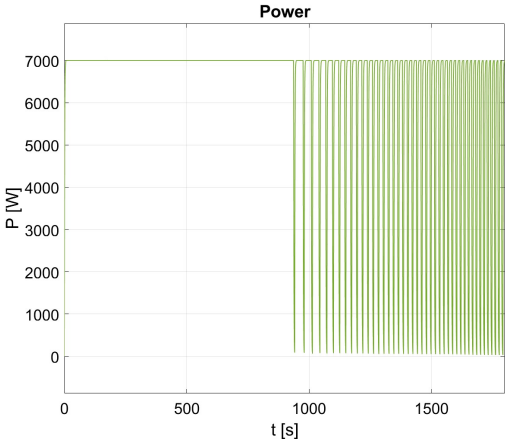

(c) PTC power consumption for WLTC without motor preheating, but with losses.

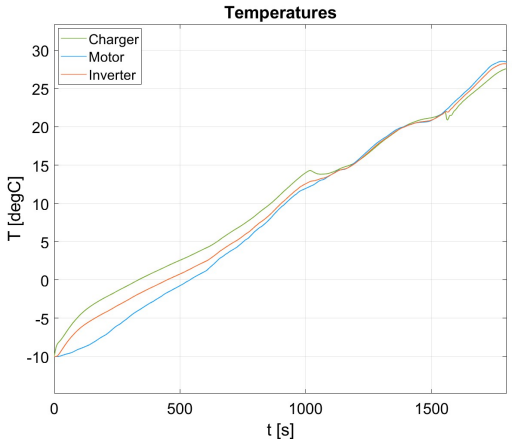

(d) EPS components temperatures for WLTC without motor preheating, but with losses.

Figure 4.36: Simulation results of WLTC run without preheating but with utilizing motor heat losses.

The graphs show a similar behavior to the simulation in the previous section when run without utilizing the heat losses. The only significant difference that can be seen in the graphs is that the EPS components reach higher temperatures as the motor is heated up by the thermal losses. This gives a temperature increase of over 10°C at the end of the cycle compared to the previous case, as the motor reaches slightly over 25°C. Some peaks and increases in the EPS component's temperatures can be

seen after 1600 seconds, which follow the driving cycle that pushes the motor more in these periods and therefore generate more losses.

The cabin is not heated up faster than without the heat losses from the motor as it takes time for the motor itself to heat up and start generate losses that are large enough to heat up the cabin. As figure 4.36d shows, the temperatures of the EPS components stop increasing in the very end of the cycle, which means that a longer cycle is required to utilize these higher temperatures.

Figure 4.37 shows when the heat exchanger between the thermal liquid coming out of the EPS system and the air going into the cabin, is being activated. This is because the graph shows the temperature difference between the thermal liquid and the air, which activates the heat exchanger when its positive, as this means that the thermal liquid is warmer than the air and will heat it up instead of cooling it down.

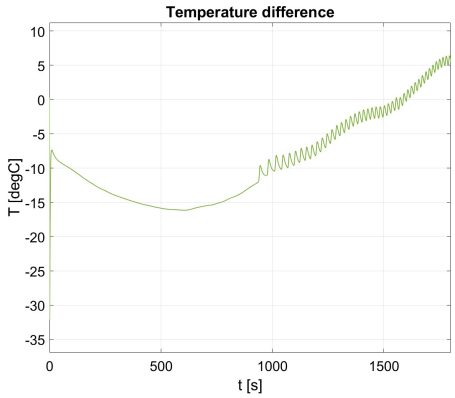

Figure 4.37: Temperature difference between thermal liquid out of EPS and air into cabin, controlling the heat exchanger.

From figure 4.37 it is possible to see that after approximately 1600s, the graph exceeds 0 and the system starts utilizing the heat losses from the motor to heat up the cabin. This means that the thermal liquid coming out of the EPS system is colder than the air going into the cabin during almost the whole cycle. Therefore, the heat losses from the motor can not be utilized properly until the motor is warm enough.

4.3.1.3 With preheating and with utilizing heat losses

When the simulation was run with both preheating and utilizing the heat losses of the motor, it resulted in the following heating of the cabin, temperatures of the EPS components and energy consumption from the PTC heater, presented in figure 4.38.

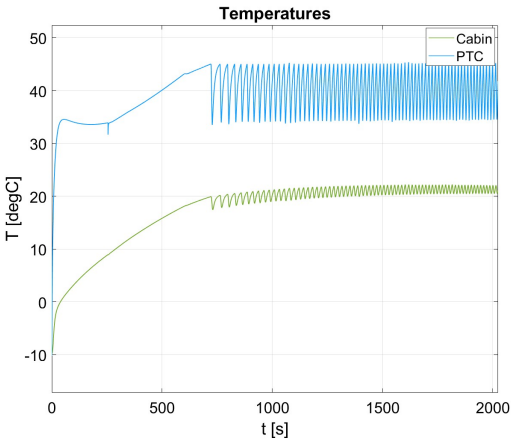

(a) Cabin temperature for WLTC with both motor preheating and losses.

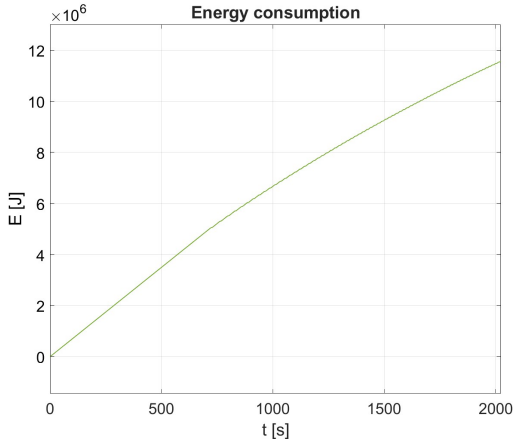

(b) PTC energy consumption for WLTC with both motor preheating and losses.

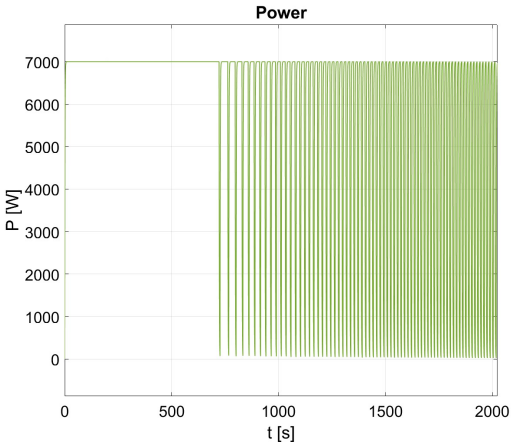

(c) PTC power consumption for WLTC with both motor preheating and losses.

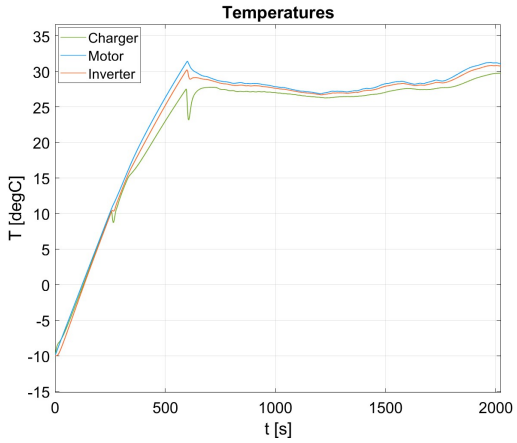

(d) EPS components temperatures for WLTC with both motor preheating and losses.

Figure 4.38: Simulation results of WLTC run with preheating and with utilizing motor heat losses.

The graphs show that the cabin and EPS components are heated up faster thanks to the preheating of the motor. This means that the cabin reaches its setpoint temperature faster so that the power consumption of the PTC heater starts fluctuating earlier, which means that the energy consumption decreases. When looking closely at figure 4.38c and comparing it with the power consumption without the preheating of the motor shown in figure 4.36c, it is possible to see a small difference. The peaks when the power is running maximally are a little bit shorter in the case when the motor has been preheated as the losses from the motor are larger after the preheating, which means that less power has to be used by the PTC heater to heat up the cabin. The overall time when the power is running on maximum is therefore shorter when the preheating is used, which means that less energy is consumed by the PTC heater.

Figure 4.39 shows the temperature difference between the thermal liquid and air.

This shows that before 300 seconds, the thermal liquid is warmer than the air, which means that the heat exchanger is activated and the motor losses are heating up the cabin.

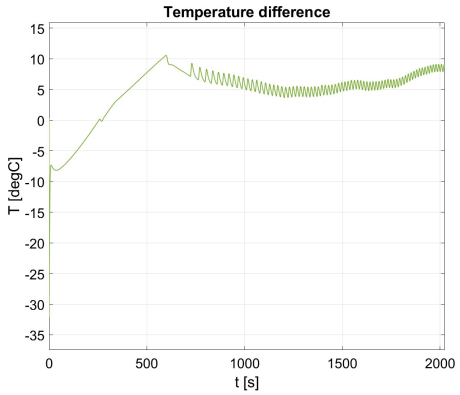

Figure 4.39: Temperature difference between thermal liquid out of EPS and air into cabin, controlling the heat exchanger, for WLTC.

The graph in figure 4.39 shows that with the preheating, the thermal liquid becomes warmer than the air after less than 300 seconds. Therefore, the losses from the motor are utilized to heat up the cabin almost immediately, which is the reason for the energy consumption of the PTC heater to be reduced while running the motor with preheating compared to running without the preheating.

4.3.1.4 Comparison of WLTC simulations with and without losses and preheating

To allow for a comparison of the consumed energy by the PTC heater, the consumption was measured at every 500 seconds and printed in table 4.9. The difference in consumption between the simulation and its forerunner was also calculated for a better view of the result.

Table 4.9: Results of simulations with WLTC with the three different configurations of utilizing heat losses and preheating the motor.

Time	Preheating	Losses	PTC consumption	Difference forerunner
500s 1000s 1500s 1800s	None	None	3.49MJ 6.93MJ 9.67MJ 11.15MJ	-
500s 1000s 1500s 1800s	None	Directly from motor	3.490MJ 6.93MJ 9.67MJ 11.11MJ	-0.00MJ -0.00MJ -0.00MJ -0.05MJ
500s 1000s 1500s 1800s	1.5MJ	Directly from motor	3.49MJ 6.67J 9.26MJ 10.64MJ	-0.00MJ -0.26MJ -0.41MJ -0.47MJ

The results show that the largest energy consumption from the PTC heater is when there is no preheating of the system and that the heat losses from the motor are not utilized for heating up the cabin, as expected.

It is possible to see that the PTC heater's energy consumption barely decreases when the heat losses from the motor are utilized. The first time when it is possible to see any change is after 1800 seconds, and it is still only a decrease of 0.05MJ. The reason for this is that the temperatures of the EPS components are rising slowly, which means that it is not until the end of the simulation that they have reached temperatures of over 25°C. The thermal liquid from the EPS components is therefore not able to heat up the air loop that goes through the cabin until the end of the simulation. This was also seen in figure 4.37, where the difference of the temperatures of the thermal liquid out of the EPS system and the air going into the cabin. When the graph has a negative value, the heat exchanger is not used, and when the temperature difference is positive, the thermal liquid goes through the exchanger. This means that the heat exchanger only is used during the last 200 seconds, which means that this is the only time that the thermal losses from the motor are utilized to heat up the cabin, hence the low difference in PTC heater energy consumption.

The result of the first two rows in the table is therefore reasonable, as the first time a decrease in the PTC heater's power consumption is seen is during the last 300 seconds of the simulation, the only time when the heat utilization of the losses is actually being used. Therefore, to be able to see an actual decrease in the PTC heater's energy consumption while only utilizing the losses from the motor, without preheating it, a longer cycle needs to be run. This would mean that when the motor has gained temperature, there would still be a big part of the simulation left. Then the heat losses could be utilized for a longer time, which probably would give a much larger decrease in the consumed energy by the PTC heater.

On the other hand, when the motor is being preheated, it gains temperature in the beginning of the cycle even though it is a short cycle. This means that using the preheating of the motor, as predicted, reduces the energy consumption in the beginning of the heating of the cabin as more heat losses can be utilized.

The problem with the preheating is that when the motor is preheated with 1.5MJ, the maximum reduction in energy consumed by the PTC heater is 0.47MJ, which is less than the energy used for the preheating. This means that over 1MJ is still lost when using the preheating compared to just utilizing the heat losses from the motor. This is because a lot of energy needs to be spent on raising the temperature of the electric motor that has a large mass. As the PTC heater transfers the power almost straight to the coolant, less energy is required as the coolant has a very low mass. The preheating of the motor is therefore not beneficial in this case and for this matter, but it would be possible to test difference values and times on the preheating to see if a more beneficial result could be obtained.

4.3.2 Simulations with variant of NEDC

Table 4.9 showed that a longer cycle needed to be run to allow the utilization of the heat losses. Therefore, the variant of the NEDC described in section 3.4.1 was simulated both without any heat losses being utilized and with these losses utilized for cabin heating. It was also run with motor heat losses utilization combined with preheating of the motor, to see if preheating could save energy consumed by the PTC heater even more. The simulations gave the results described in the following section when run in the different configurations.

4.3.2.1 Without preheating or utilizing heat losses

When the simulation was run without the preheating of the motor and the heat losses from it were not utilized, it resulted in the following cabin heating, power and energy consumption from the PTC heater, as well as temperature of the EPS components, presented in figure 4.40.

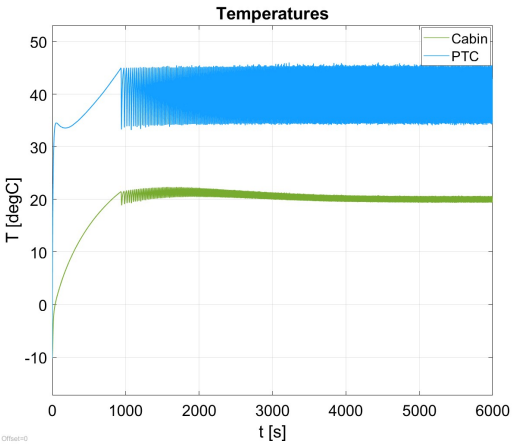

(a) Cabin temperature for variant of NEDC without motor preheating or losses.

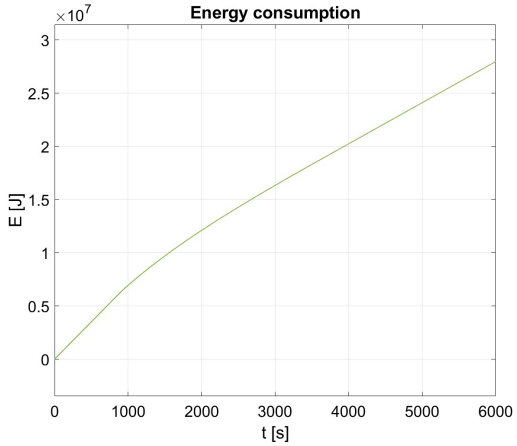

(b) PTC energy consumption for variant of NEDC without motor preheating or losses.

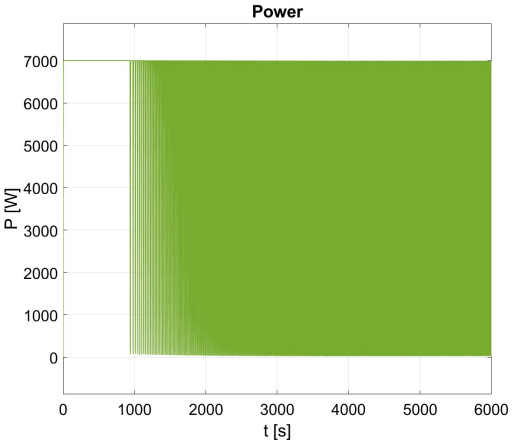

(c) PTC power consumption for variant of NEDC without motor preheating or losses.

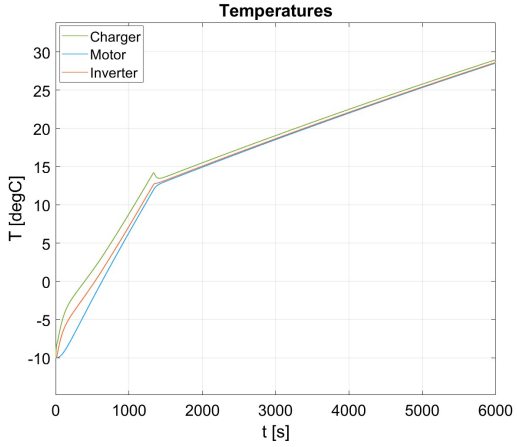

(d) EPS components temperatures for variant of NEDC without motor preheating or losses.

Figure 4.40: Simulation results of variant of NEDC run without preheating and without utilizing motor heat losses.

The figures show similar behaviour as when running the same configuration, no preheating and no utilization of motor losses, with the WLTC described in section 4.3.1.1, even though different driving cycles were run. This shows that the principle is the same with the heating of the cabin, as well as the power and energy consumption, even if there is a small change in the numbers when looking closely. The temperatures of the EPS components, however, are a bit different when the longer cycle, the variant of the NEDC, is run. During the first 1800 seconds of the simulation, the EPS component temperatures are basically identical to when the WLTC was run. But as the NEDC variant is longer, the components have more time to heat up. Figure 4.35d shows that after the first 1800 seconds of the simulation, the components keep gaining temperature. After the 6000 seconds, the EPS components have reached temperatures of almost 30°C. It is possible to see that the slopes of the graphs show that the temperatures are constantly increasing, so a

longer simulation would reach even higher temperatures.

4.3.2.2 With utilizing heat losses, but not preheating the motor

When the simulation was run still without preheating the motor, but with utilizing the heat losses generated by it, it resulted in the following cabin heating, power and energy consumption from the PTC heater, and temperatures of the EPS components, presented in figure 4.41.

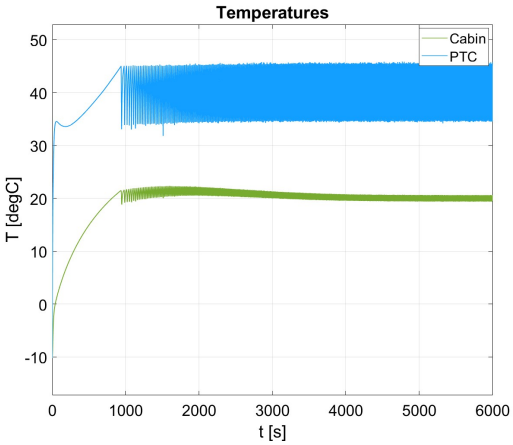

(a) Cabin temperature for variant of NEDC without motor preheating, but with losses.

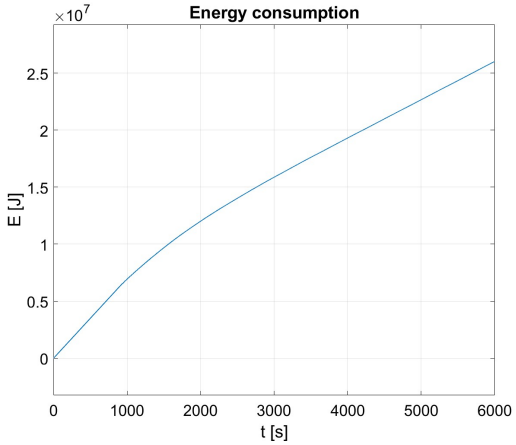

(b) PTC energy consumption for variant of NEDC without motor preheating, but with losses.

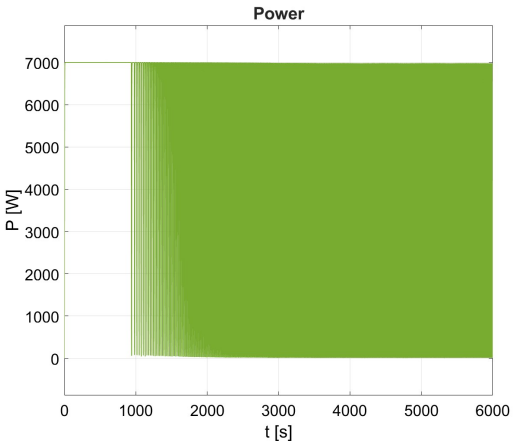

(c) PTC power consumption for variant of NEDC without motor preheating, but with losses.

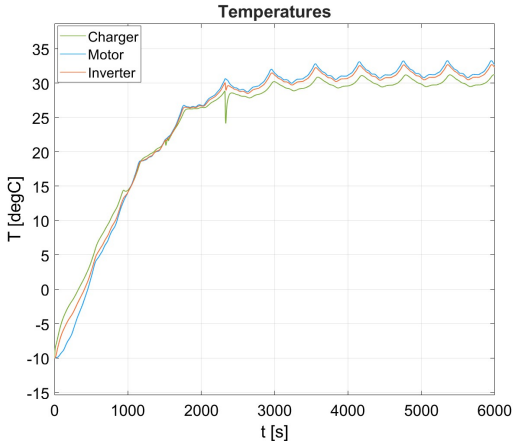

(d) EPS components temperatures for variant of NEDC without motor preheating, but with losses.

Figure 4.41: Simulation results of variant of NEDC run with preheating but without utilizing motor heat losses.

The graphs show that the PTC heater's energy consumption is lower than for the simulation without utilizing the losses, but the graphs still follow the same pattern. There are peaks in the last 4000 seconds in figure 4.41d, that show that the temperatures of the EPS components are affected by the driving cycle. These peaks

correspond to the velocity peaks in the NEDC variant and come up due to high accelerations that push the motor and generate more heat losses that heat up the EPS components.

Figure 4.42 illustrates the temperature difference between the thermal liquid and the air, which also shows when the heat exchanger between them is being used.

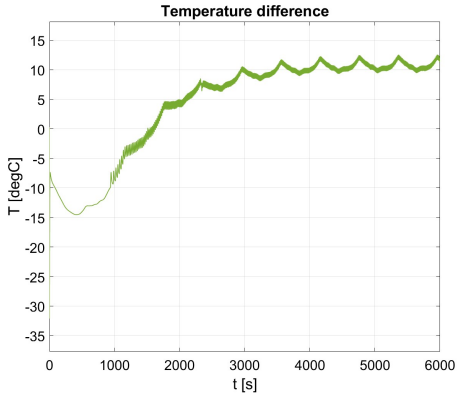

Figure 4.42: Temperature difference between thermal liquid out of EPS and air into cabin, controlling the heat exchanger, for variant of NEDC.

Figure 4.42 shows that it is after around 1500 seconds that the heat exchanger is activated so that the thermal liquid out of the EPS system is heating up the air into the cabin. Therefore, during approximately 4500 seconds, the heat losses are being utilized to help the PTC heater with the heating of the cabin. This means that, compared to running the shorter WLTC cycle with utilizing the heat losses from the motor, described in section 4.3.1.2, the heat losses are being utilized for a much longer time. As a small decrease in energy consumption by the PTC heater was seen when the heat losses were starting to be utilized when the WLTC was run, the same pattern should be seen when running the longer NEDC variant, but with a larger decrease in energy consumption.

4.3.2.3 With preheating and with utilizing heat losses

When the simulation was run with both preheating and utilizing the heat losses of the motor, it resulted in the following cabin heating, energy and power consumption from the PTC heater, as well as temperatures of the EPS components, shown in figure 4.43.

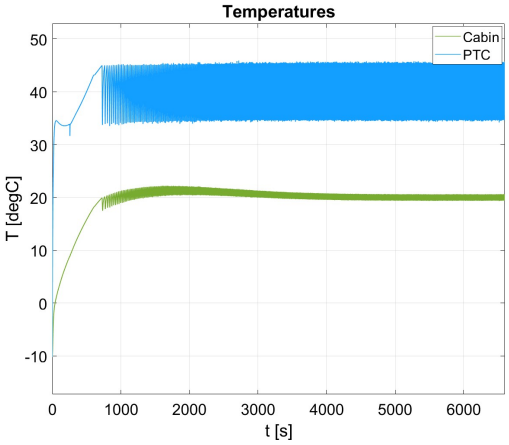

(a) Cabin temperature for variant of NEDC with both motor preheating and losses.

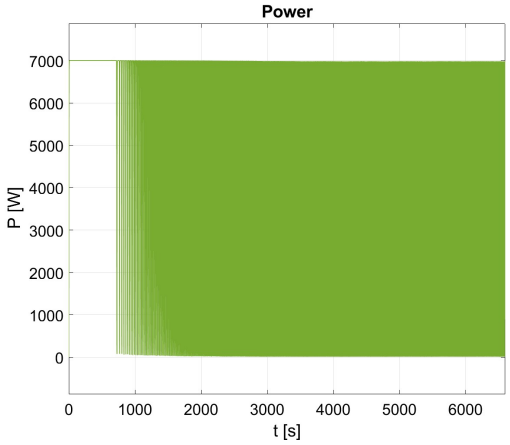

(b) PTC power consumption for variant of NEDC with both motor preheating and losses.

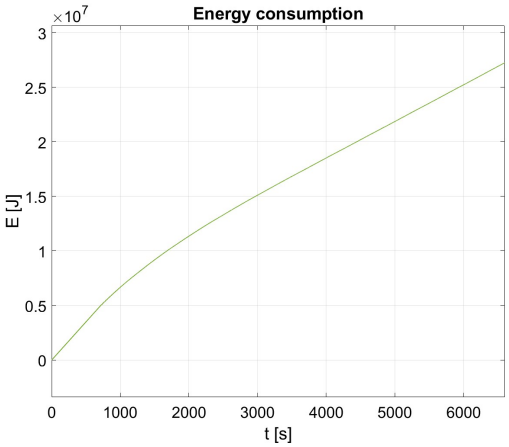

(c) PTC energy consumption for variant of NEDC with both motor preheating and losses.

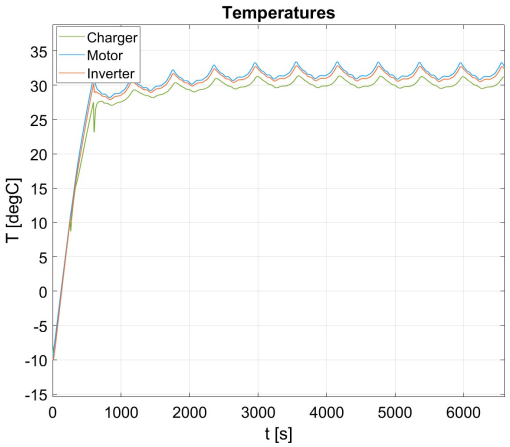

(d) EPS components temperatures for variant of NEDC with both motor preheating and losses.

Figure 4.43: Simulation results of variant of NEDC run with preheating and with utilizing motor heat losses.

The graphs show that the cabin reaches its setpoint temperature faster, due to the preheating of the motor, which is the same behavior as when the WLTC was run. The energy consumption graph for the PTC heater then starts to subside earlier, which means that less energy is consumed by it in total as its maximum power is used for a shorter amount of time. It is also possible to see the same pattern with the peaks that follow the peaks of the driving cycle in the same way as when the NEDC variant was run without preheating, in section 4.3.2.2.

As in the previous sections, the graph showing the temperature difference between the thermal liquid and air, and therefore when the heat exchanger between them is activated, is shown in the figure 4.44 below.

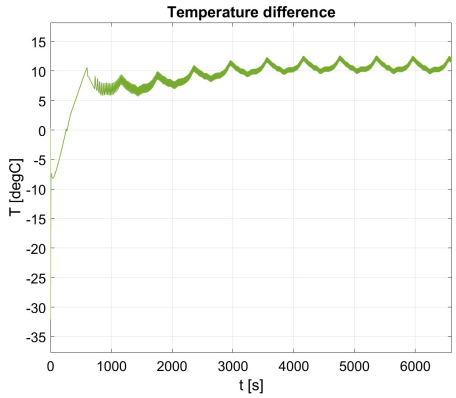

Figure 4.44: Temperature difference between thermal liquid out of EPS and air into cabin, controlling the heat exchanger, for variant of NEDC.

Figure 4.44 shows that, thanks to the preheating of the motor, the thermal liquid from the EPS starts heating the air going into the cabin after just a couple of 100 seconds. The losses are therefore being utilized during almost the whole simulation as the thermal liquid has a high temperature from the beginning of the simulation and is able to help heating the cabin.

4.3.2.4 Comparison of variant of NEDC simulations with and without losses and preheating

Table 4.10 below summarizes the consumption of energy by the PTC heater with the three different configurations of preheating and motor heat utilization that were run.

Table 4.10: Results of simulations with NEDC variant cycle with the three different configurations of utilizing heat losses and preheating the motor.

Time	Preheating	Losses	PTC consumption	Difference forerunner
1000s	None	None	6.930MJ	-
2000s			12.08MJ	
3000s			16.30MJ	
4000s			20.22MJ	
5000s			23.99MJ	
6000s			27.73MJ	
1000s	None	Directly from motor	6.930MJ	-0.00MJ
2000s			12.00MJ	-0.08MJ
3000s			15.87MJ	-0.43MJ
4000s			19.31MJ	-0.91MJ
5000s			22.66MJ	-1.33MJ
6000s			26.02MJ	-1.71MJ
1000s	1.5MJ	Directly from motor	6.660MJ	-0.27MJ
2000s			11.36MJ	-0.64MJ
3000s			15.12MJ	-0.75MJ
4000s			18.53MJ	-0.78MJ
5000s			21.87MJ	-0.79MJ
6000s			25.22MJ	-0.80MJ

The results show that the largest energy consumption from the PTC heater is when there is no preheating of the system and that the heat losses from the motor are not utilized for heating up the cabin, as expected.

During the first 1000 seconds, when the motor is still cold, there is no decrease in energy consumption from the PTC heater when the simulation runs without preheating. When the motor gets warmer, after 1000 seconds, the consumption from the PTC heater keeps decreasing while the simulation is running. This shows that utilizing the heat losses to heat up the cabin fulfills its aim by decreasing the power consumption of the PTC heater. By decreasing the consumption of the heater, less total energy is used by the battery, which means that this energy can be used for driving the car instead. In turn, this increases the total range of the vehicle.

Compared to the simulation with the WLTC that only lasted for 1800 seconds, the motor has time to heat up and then start to generate losses that can be utilized. It is therefore possible to see a relatively large decrease in energy consumed by the PTC heater; 1.71 MJ in total after 6000 seconds of simulation. It is possible to see in the table that the difference in energy consumption between running without utilizing losses and running with keeps increasing. Therefore, the longer the simulation would run, the larger the difference would most likely be. This is thanks to that as long as the motor is running, it keeps generating losses that keep heating up the cabin. This also means that the harder the motor is pushed, the more losses it will

generate and help heating the cabin. Then the motor is, of course, consuming more energy in general, which is something that's good to keep in mind as it decreases the total range of the vehicle.

In the end of the simulation, the improvement in PTC energy consumption when utilizing the losses, but not preheating the motor, can be calculated from equation (4.3).

$$\text{Improvement} = \frac{\text{Saved energy}}{\text{Total consumption}} = \frac{1.71}{26.02} = 0.0657 = 6.75\% \tag{4.3}$$

This means that the 1.71MJ that was saved by utilizing the heat losses of the motor constitutes to 6.75% of the total energy consumed by the PTC heater in loss utilizing configuration. The unit of the energy consumed by the PTC heater has been MJ throughout this thesis, but can be converted to kWh to make it easier to relate to. 26.02 MJ is the total consumption of the PTC heater during the variant of the NEDC cycle when the heat losses are being utilized, but the motor has not been preheated. This can be converted to 7.23 kWh. The energy gained by utilizing the losses, 1.71MJ, can be converted to 0.475 kWh.

When the simulation is run with also preheating the motor, it can be seen that more energy is saved by the PTC heater, also more than in the simulation with the WLTC, but still not more than what is used to preheat the motor. The conclusion is therefore the same as for the WLTC simulation; that for this particular aspect, it is not worth preheating the motor as it uses more energy than what it being saved.

4.3.3 Conclusion of both WLTC and variant of NEDC simulations

The overall conclusion of the simulations run, both with the shorter WLTC and the longer NEDC variant, is that utilizing the heat losses generated by the motor saves energy consumed by the PTC heater, while preheating the motor and then utilizing the heat losses saves energy, but less energy than the preheating itself consumes.

For the utilization of heat losses from the motor, the cycle needs to be run for a long enough time to get a decrease in the energy consumption of the PTC heater. This is because the motor needs time to get warm enough to produce losses that can be utilized. As the preheating only happens in the beginning of the simulation, the length of the simulation does not affect if its useful or not, if the cycle is long enough for the value to stabilize. The driving cycle does affect the results even if it is very little, but there is a small difference in the energy consumption measured at the same time. Factors like the amount of time the motor is being preheated and the power used during the preheating could perhaps affect if the preheating of the motor is beneficial or not. This was not explored in this thesis, but would be an interesting future work.

One factor that has not been taken into consideration during the simulations is the efficiency of the heat transfer between the motor in the LPTN block and in the EPS block as the losses are directly added to the motor. The losses are summed up from

the LPTN model and then directly implemented as a heat flow into the motor block in the vehicle thermal management model. A better way to do this could have been to, for example, add the thermal liquid directly from the cooling circuit in the LPTN model and into the thermal liquid in the system of the vehicle thermal management model that goes directly into the heat exchanger for heating the air going into the cabin. This would have made the results more applied to reality and therefore more accurate.

Another factor is that the preheating of the motor might not be beneficial for only the matter of saving energy from the PTC heater, while it, on the other hand, could be beneficial for other aspects regarding the motor. Therefore, the knowledge that preheating of the motor reduces the energy consumption of the PTC, even if it's not more than the energy consumed by the actual preheating, can be useful. It might turn out that in the whole picture, when taking all the benefits of preheating into consideration, preheating the motor will be worth doing.

5
Conclusion

This chapter presents the conclusions from the work conducted as part of the thesis. Finally some recommendations for future work is described in section 5.1.

It can be concluded that the developed thermal model of the electric machine is able to predict the temperature developed in different parts within the expected accuracy of 30% relative error. The model is a lumped-parameter model, and it does not significantly impact the simulation time of the simulation environment. It was made as general as possible, and hence the only parameters needed are motor dimensions, material data and loss maps. If loss maps that can be assumed similar are available, similar motor types can be simulated with minimal modification. Different cooling concepts can also be evaluated.

The model validity was correlated using available test data, during steady-state operation and during a common driving cycle. At constant operating points, it was found that the model tends to underpredict the temperatures during low speeds but is rather accurate at higher speeds. This could be from a discrepancy in the loss map data compared to the actual losses seen during testing. This discrepancy was found to deviate particularly in the lower speed regions. It would also be desirable to use loss maps with temperature as a fourth dimensional, and hence temperature dependent losses that are more accurate than the current compensation factor.

It was also noted that the relative error at the end of the cycle in many cases was a lot smaller than the error over the complete cycle. An explanation to this is the difficulty of exactly mimicking the test conditions, such as initial temperature for each motor component. The smaller error at the end of the cycle shows robustness in the sense that even though the initial temperatures are off by some degrees, the overall thermal development follows and approaches the trend.

The correlation to the WLTC test data showed that the model performs well over the duration of a representative driving cycle, which is also the typical application to run in the simulation platform. Out of the two sets of test data that the model was correlated against, the WLTC cycle is considered a better metric than the steady-state cycle. Operating the motor continuously at constant speed and torque for 30 minutes is an unreasonable load condition in the real world.

The conclusions of the vehicle thermal model are that utilizing the heat losses generated by an electric motor in a battery electric vehicle can reduce the energy used by the PTC heater, which aim is to heat up the cabin. When simulating a BEV over the driving cycles WLTC and a variant of the NEDC, 6.75% of the energy used by the PTC heater can be saved, which corresponds to 0.475 kWh. This is when simulations are run in ambient temperature of -10°C and heating the cabin to 20°C. Saving energy in a component in the vehicle, means that the total energy consumption is reduced and that the range of the vehicle is increased.

The heat losses from the motor are not able to be utilized for heating the cabin until the motor is warm enough. Therefore, utilizing the heat losses are not beneficial over a short driving cycle or a driving cycle that is not pushing the motor enough to generate large losses. When the WLTC is run, it takes approximately 1600 seconds, just under half an hour, before the heat losses can be utilized. When a variant of the NEDC is run, it takes around 3000 seconds, almost an hour, before the motor is warm enough. The driving cycle, therefore, plays a big role in how much the heat losses can be utilized, as it determines how hard the motor is being pushed and therefore how large losses it produces.

To heat up faster, the motor can be preheated. Preheating the motor allows an even larger energy saving by the PTC heater, an energy saving that is smaller than the energy used for the preheating, in the cases run in this thesis work. This does not mean that preheating the motor consumes more energy in the complete vehicle, taking all components into consideration, but does in the case of only the energy from the PTC heater, simulated in certain configurations over certain driving cycles.

5.1 Future work

Due to the limitations described in section 1.3 as well as the time frame of the thesis, not all desired aspects were possible to cover. Therefore, this section consists of descriptions and ideas of future work that could be done to improve the work or develop it further.

5.1.1 EM thermal model

One of the most important measurements in the PMSM model is still to be verified - the temperature of the magnets. Due to the absence of test data with this measurement, it was not performed as part of this thesis. Verification could be performed either by gathering more test data or utilizing FE-analysis. A further alternative is to approximate the magnet temperature from the available test data from the rotor temperature, using known empirical relationships similar to a state observer.

The heat transfer coefficients to air could be validated and/or improved by utilizing CFD. This thesis has not verified the calculated HTCs any further than comparing to values found in literature.

More work can be done to build a complete and more accurate thermal model of the complete drive unit, including transmission and inverter. As was evident from comparing simulation to ERAD test data, the electric motor thermal development is not independent of the other drive unit components. On the contrary, they set the boundary conditions of the electric machine model.

Finally, it would be desirable to develop four-dimensional loss maps with temperature as the fourth component.

5.1.2 Vehicle thermal model and heat utilization

Some aspects have been mentioned in the vehicle thermal modeling where future improvements can be done. These are the control system of the cabin temperature, where it now overshoots a little bit over the set temperature, before it goes down and stabilizes around it. Heating up the cabin in cold climate over the setpoint temperature will not only make the temperature warmer than what the occupants wish for, but also consumes extra energy with the PTC heater. Modifying the control system of the cabin heating could therefore save energy while improving the comfort for the occupants. Another improvement that could be done in the vehicle thermal model is the way that the losses from the LPTN are implemented. By summing the losses from the LPTN model and implementing them as a heat flow directly into the thermal management model, efficiency and similar aspects are neglected. One way to simulate real circumstances better would be to take the coolant from the LPTN and implement it directly into the thermal management model. This is more physically accurate than implementing the magnitude of the losses.

Regarding the preheating of the motor, it was in this thesis used to investigate if it could reduce the PTC heater's energy consumption even further, together with the utilization of the heat losses. The simulations showed that the preheating did not reduce the energy consumption of the PTC heater more than the amount energy used for the preheating, when it was run with certain values. This, however, does not ensure that preheating is not beneficial with any values, as only one case was run during the thesis. Therefore, future work could be to run the preheating during different times and with different power, to see if some values could make it beneficial for the PTC heater's energy consumption. Also, investigating if the preheating is beneficial for other aspects like lower power consumption overall from the motor or wear reduction on the motor, would be interesting to do. This could result in that preheating of the motor is beneficial on a higher level as it is already decreasing the power consumption of the PTC heater, just not more than the energy being used for the actual preheating.

For this thesis work, the LPTN system was only considered for the rear motor. Utilizing the losses from both motors (in the case of a dual motor vehicle) would mean that more heat losses could be utilized and the power consumption of the PTC heater could be reduced further. Also, the heat losses could be used for other aspects than heating up the cabin, for example to heat up the battery to help keeping it in its temperature window. This could improve the efficiency of the battery and therefore the energy consumption of the vehicle, while also improving the performance of the vehicle.

Lastly, future work includes investigating the effect of utilizing the heat losses from the motor on the range of the vehicle. By proving that the PTC heater consumes less energy, it is proved that the range of the vehicle is increased as less energy from the battery is used for this, but not by how much. By modeling the energy consumption by all components in the vehicle and including them in the calculation of the range of the vehicle, it would allow seeing how much the utilization of the motor heat losses improve the total driving range of the vehicle.

Bibliography

[1] Polestar Sweden, "Polestar_precept_039, id 504289," 2023, [Electronic image]. Available: https://media.polestar.com/se/sv/media/photos/504289 [Accessed: 2023-06-06].

[2] P.loos, Wikimedia Commons, "Stator machine triphasée," 2023, [Electronic image]. Available: https://commons.wikimedia.org/wiki/File:Stator_machine_triphas%C3%A9e.jpg [Accessed: 2023-06-27].

[3] Wikipedia Commons, "Nedc," Accessed May. 30, 2023. [Online]. Available: https://commons.wikimedia.org/wiki/File:NEDC.language.multi.svg

[4] ——, "Wltc class 3," Accessed May. 30, 2023 [Online]. [Online]. Available: https://commons.wikimedia.org/wiki/File:WLTC_class_3.svg

[5] L. Burs, E. Roemer, S. Worm, and A. Masini, "Are they all equal? uncovering adopter groups of battery electric vehicles," *Sustainability (Switzerland)*, vol. 12, 4 2020.

[6] M. A. Melliger, O. P. van Vliet, and H. Liimatainen, "Anxiety vs reality – sufficiency of battery electric vehicle range in switzerland and finland," *Transportation Research Part D: Transport and Environment*, vol. 65, pp. 101–115, 12 2018.

[7] N. Meyer, I. Whittal, M. Christenson, and A. Loiselle-Lapointe, "The impact of driving cycle and climate on electrical consumption & range of fully electric passenger vehicles," in *26th Electric Vehicle Symposium 2012, EVS 2012*, vol. 1, 2012.

[8] M. Steinstraeter, T. Heinrich, and M. Lienkamp, "Effect of low temperature on electric vehicle range," *World Electric Vehicle Journal*, vol. 12, 2021.

[9] Z. Zhang, J. Wang, X. Feng, L. Chang, Y. Chen, and X. Wang, "The solutions to electric vehicle air conditioning systems: A review," *Renewable and Sustainable Energy Reviews*, vol. 91, 2018.

[10] J. J. Meyer, J. Lustbader, N. Agathocleous, A. Vespa, J. Rugh, and G. Titov, "Range extension opportunities while heating a battery electric vehicle," in *SAE Technical Papers*, vol. 2018-April, 2018.

[11] J. Guo and F. Jiang, "A novel electric vehicle thermal management system based on cooling and heating of batteries by refrigerant," *Energy Conversion and Management*, vol. 237, 2021.

[12] Polestar, "Polestar 2 - plus pack," Accessed Jan. 24, 2023 [Online]. [Online]. Available: https://www.polestar.com/global/polestar-2/upgrades/#plus-pack

[13] S. Wu, R. Xiong, H. Li, V. Nian, and S. Ma, "The state of the art on preheating lithium-ion batteries in cold weather," *Journal of Energy Storage*, vol. 27, 2020.

[14] K. Minnerup, T. Herrmann, M. Steinstraeter, and M. Lienkamp, "Case study of holistic energy management using genetic algorithms in a sliding window approach," *World Electric Vehicle Journal*, vol. 10, 2019.

[15] A. Kersten, A. Andersson, B. Ban, Y. Xu, M. Rodén, A. Norouzzadeh, and S. Rydén, "Electric vehicle heating management techniques utilizing drivetrain-loss-heating of refrigerant," in *IECON – 48th Annual Conference of the IEEE Industrial Electronics Society*, 2022, pp. 1–8. [Online]. Available: https://ieeexplore.ieee.org/document/9968738

[16] Polestar, "Polestar sustainability," Accessed Jan. 25, 2023 [Online]. [Online]. Available: https://www.polestar.com/global/sustainability/

[17] J. Buberger, A. Kersten, M. Kuder, R. Eckerle, T. Weyh, and T. Thiringer, "Total co2-equivalent life-cycle emissions from commercially available passenger cars," *Renewable and Sustainable Energy Reviews*, vol. 159, 2022.

[18] Y. Yang, B. Bilgin, M. Kasprzak, S. Nalakath, H. Sadek, M. Preindl, J. Cotton, N. Schofield, and A. Emadi, "Thermal management of electric machines," 2017.

[19] A. Boglietti, A. M. El-Refaie, O. Drubel, A. M. Omekanda, N. Bianchi, E. B. Agamloh, M. Popescu, A. D. Gerlando, and J. B. Bartolo, "Electrical machine topologies: Hottest topics in the electrical machine research community," *IEEE Industrial Electronics Magazine*, vol. 8, 2014.

[20] A. Hughes and B. Drury, *Electric Motors and Drives: Fundamentals, Typas and Applications*, 5th ed. Newnes, Elsevier, 2019.

[21] I. Boldea, L. N. Tutelea, L. Parsa, and D. Dorrell, "Automotive electric propulsion systems with reduced or no permanent magnets: An overview," *IEEE Transactions on Industrial Electronics*, vol. 61, 2014.

[22] B. Raghuraman, S. Nategh, N. Sidiropoulos, L. Petersson, and A. Boglietti, "Sustainability aspects of electrical machines for e-mobility applications part i: A design with reduced rare-earth elements," vol. 2021-October, 2021.

[23] A. Acquaviva, M. DIana, B. Raghuraman, L. Petersson, and S. Nategh, "Sustainability aspects of electrical machines for e-mobility applications part ii: Aluminium hairpin vs. copper hairpin," vol. 2021-October, 2021.

[24] G. Cutuli, D. Barater, S. Nategh, D. Ericsson, and M. Törmänen, "Aluminum hairpin solution for electrical machines in e-mobility applications : Part ii:thermal and cooling aspects," 2022.

[25] Z. Huang, "Thermal design of electrical machines: Investigation and evaluation of cooling performances," Licentiate Thesis, Lund University, Lund, Sweden, July 2013.

[26] C. J. Paar, "Thermal design of electric traction machines integrated in hybrid electric vehicles," PhD thesis, Graz University of Technology, Graz, AT, July 2016, available at https://diglib.tugraz.at/download.php?id=60827547c05cb&location=browse.

[27] E. A. Grunditz, "Design and assessment of battery electric vehicle powertrain, with respect to performance, energy consumption and electric motor thermal capability," PhD thesis, Chalmers University of Technology, Göteborg, SE, May 2016, available at https://research.chalmers.se/publication/236616.

[28] A. Boglietti, A. Cavagnino, D. Staton, M. Shanel, M. Mueller, and C. Mejuto, "Evolution and modern approaches for thermal analysis of electrical machines," vol. 56, 2009.

[29] M. Schrittwieser, A. Marn, E. Farnleitner, and G. Kastner, "Numerical analysis of heat transfer and flow of stator duct models," *IEEE Transactions on Industry Applications*, vol. 50, 2014.

[30] S. Nategh, Z. Huang, A. Krings, and M. Leksell, "Thermal modeling of directly cooled electric machines using lumped parameter and limited cfd analysis," *IEEE Transactions on Energy Conversion*, vol. 28, 2013.

[31] S. Nategh, H. Zhang, O. Wallmark, A. Boglietti, T. Nassen, and M. Bazant, "Transient thermal modeling and analysis of railway traction motors," *IEEE Transactions on Industrial Electronics*, vol. 66, 2019.

[32] P. Ponomarev, M. Polikarpova, and J. Pyrhönen, "Thermal modeling of directly-oil-cooled permanent magnet synchronous machine," in *Thermal modeling of directly-oil-cooled permanent magnet synchronous machine*, 2012.

[33] Y. A. Çengel and A. J. Ghajar, *Heat and Mass Transfer: Fundamentals & Applications*, 5th ed. McGraw-Hill Education, 2015.

[34] Wikipedia, "Thermal conductivity, thermal anisotropy," 2023, https://en.wikipedia.org/wiki/Thermal_conductivity#Thermal_anisotropy [Accessed: 2023-05-25].

[35] D. Staton, A. Boglietti, and A. Cavagnino, "Solving the more difficult aspects of electric motor thermal analysis in small and medium size industrial induction motors," 2005.

[36] E. A. Grunditz, T. Thiringer, J. Lindström, S. T. Lundmark, and M. Alatalo, "Thermal capability of electric vehicle pmsm with different slot areas via thermal network analysis," *eTransportation*, vol. 8, 2021.

[37] S. M. Ammar and C. W. Park, "Validation of the gnielinski correlation for evaluation of heat transfer coefficient of enhanced tubes by non-linear regression model: An experimental study of absorption refrigeration system," *International Communications in Heat and Mass Transfer*, vol. 118, 2020.

[38] M. Bires, C. Paul, and P. Drage, "Smart approach for the thermal management of electric vehicles," *ATZ worldwide*, vol. 123, 2021.

[39] M. Sreekanth, M. Feroskhan, N. Gobinath, G. L. Rao, and N. Sinaga, "Comprehensive exergy analysis of thermal management of cabin, battery and motor in electric vehicles," *International Journal of Applied Science and Engineering*, vol. 19, 9 2022.

[40] M. Setiyo, B. Waluyo, and N. Hamidi, "Analysis of evaporator effectiveness on 1/2 cycle refrigeration systems: A case study on lpg fueled vehicles," *Jurnal Teknologi*, vol. 82, 2020.

[41] A. Abdulwahab and S. Mysen, "Experimental study of condenser material in the air conditioning system," *Materials Today: Proceedings*, vol. 61, 2022.

[42] X. Yin, J. Fang, A. Wang, Y. Song, F. Cao, and X. Wang, "A novel co2 thermal management system with battery two-phase (evaporative) cooling for electric vehicles," *Results in Engineering*, vol. 16, 2022.

[43] M. H. Park and S. C. Kim, "Heating performance characteristics of high-voltage ptc heater for an electric vehicle," *Energies*, vol. 10, 2017.

[44] R. Musat and E. Helerea, "Characteristics of the ptc heater used in automotive hvac systems," *IFIP Advances in Information and Communication Technology*, vol. 314, 2010.

[45] M. Ibragimov, D. Akbarov, and I. Tadjibekova, "Investigation of asynchronous electric motor winding in heating mode and drying mode to prevent moisture," vol. 365. EDP Sciences, 1 2023.

[46] Z. Sun, Z. Wen, X. Zhao, Y. Yang, and S. Li, "Real-world driving cycles adaptability of electric vehicles," *World Electric Vehicle Journal*, vol. 11, 2020.

[47] P. Iora and L. Tribioli, "Effect of ambient temperature on electric vehicles' energy consumption and range: Model definition and sensitivity analysis based on nissan leaf data," *World Electric Vehicle Journal*, vol. 10, 2019.

[48] M. Lapuerta, J. Rodríguez-Fernández, Ángel Ramos, D. Donoso, and L. Canoira, "Wltc and real-driving emissions for an autochthonous biofuel from wine-industry waste," *Scientific Reports*, vol. 11, 12 2021.

[49] The MathWorks, Inc., "Matlab," 2023. [Online]. (accessed on 2023-03-21). [Online]. Available: https://se.mathworks.com/products/matlab.html

[50] ——, "Simulink," 2023. [Online]. (accessed on 2023-03-21). [Online]. Available: https://se.mathworks.com/products/simulink.html

[51] ——, "Simscape," 2023. [Online]. (accessed on 2023-03-21). [Online]. Available: https://se.mathworks.com/products/simscape.html

[52] ——, "Foundation and custom domains," 2023. [Online]. (accessed on 2023-05-31). [Online]. Available: https://se.mathworks.com/help/simscape/creating-custom-domains.html

[53] ——, "Modeling moist air systems," 2023. [Online]. (accessed on 2023-05-31). [Online]. Available: https://se.mathworks.com/help/simscape/ug/modeling-moist-air-systems.html

[54] ——, "Thermal models," 2023. [Online]. (accessed on 2023-05-31). [Online]. Available: https://se.mathworks.com/help/simscape/thermal-models.html?s_tid=CRUX_topnav

[55] ——, "Modeling thermal liquid systems," 2023. [Online]. (accessed on 2023-05-31). [Online]. Available: https://se.mathworks.com/help/simscape/ug/thermal-liquid-modeling-workflow.html

[56] ——, "Two-phase fluid models," 2023. [Online]. (accessed on 2023-05-31). [Online]. Available: https://se.mathworks.com/help/simscape/two-phase-fluid-models.html

[57] ——, "Mechanical models," 2023. [Online]. (accessed on 2023-05-31). [Online]. Available: https://se.mathworks.com/help/simscape/mechanical-models.html

[58] J. Nerg, M. Rilla, and J. Pyrhönen, "Thermal analysis of radial-flux electrical machines with a high power density," *IEEE Transactions on Industrial Electronics*, vol. 55, 2008.

[59] D. Kuehbacher, A. Kelleter, and D. Gerling, "An improved approach for transient thermal modeling using lumped parameter networks," in *An improved approach for transient thermal modeling using lumped parameter networks*, 2013.

[60] J. E. Cousineau, K. Bennion, D. DeVoto, and S. Narumanchi, "Experimental characterization and modeling of thermal resistance of electric machine lamination stacks," *International Journal of Heat and Mass Transfer*, vol. 129, 2019.

[61] N. Simpson, R. Wrobel, and P. H. Mellor, "Estimation of equivalent thermal parameters of impregnated electrical windings," *IEEE Transactions on Industry Applications*, vol. 49, 2013.

[62] P. B. Swann, H. Russell, and I. H. Jahn, "Taylor-couette-poiseuille flow heat transfer in a high taylor number test rig," *Journal of the Global Power and Propulsion Society*, vol. 5, 2021.

[63] A. Boglietti, A. Cavagnino, and D. Staton, "Determination of critical parameters in electrical machine thermal models," *IEEE Transactions on Industry Applications*, vol. 44, 2008.

[64] B. Andersson, "Lumped parameter thermal modelling of electric machines: Analysis of an interior permanent magnet synchronous machine for vehicle applications," Master's thesis, Chalmers University of Technology, 2013, available at https://odr.chalmers.se/items/8110a58b-1050-48dd-87bf-e8fd8e6d1d0d.

[65] The MathWorks, Inc., "Electric vehicle thermal management," 2023. [Online]. (accessed on 2023-04-15). [Online]. Available: https://se.mathworks.com/help/hydro/ug/sscfluids_ev_thermal_management.html

[66] A. Boglietti, A. Cavagnino, and D. A. Staton, "Tefc induction motors thermal models: A parameter sensitivity analysis," *IEEE Transactions on Industry Applications*, vol. 41, 2005.

DEPARTMENT OF MECHANICS AND MARITIME SCIENCES
CHALMERS UNIVERSITY OF TECHNOLOGY
Gothenburg, Sweden
www.chalmers.se

CHALMERS
UNIVERSITY OF TECHNOLOGY